S.E.M. Brummel

Master Thesis

Feasibility of Acoustic Emission Methods for Fatigue Monitoring in Tubular Double Side Welded T-joints

TU Delft

royal roos

Master Thesis

Feasibility of Acoustic Emission Methods for Fatigue Monitoring in Tubular Double Side Welded T-joints

By

S.E.M. Brummel

in partial fulfillment of the requirements for the degree of

Master of Science
in Offshore Engineering

at the Delft University of Technology,
to be defended publicly on Tuesday, August 27, 2018, at 14:30 AM.

Supervisor:	Prof.dr.ir. Mirek Kaminski	TU Delft
Thesis committee:	Ir. Fengfeng Mao	Royal Roos
	Dr. Lotfollah Pahlavan	TU Delft
	Ir. Fulko Roos	Royal Roos
	Ir. Bart Scheeren,	TU Delft
	Dr.Ir. Paul van Woerkom,	TU Delft


Salomon Brummel
27-8-2018

Preface

This thesis is the accumulation of 20 years of studying which resulted in obtaining the Masters of Science degree in Offshore and Dredging Engineering at the faculty of Mechanical, Maritime and Materials Engineering of the Delft University of Technology. The graduation process was not a smooth ride and definitely not a short one but after a hard sprint to finish everything there is a result and I am very content with that.

This thesis was not possible without all the support I got. First I would like to thank Fulko Roos and Veronica Breed for the opportunity to cooperate with Royal Roos. They have provided me with a working space and helped me with the process and most of all making me feel at home within the organization. I would also like to thank the team at Royal Roos with Fengfeng Mao and Alejandro Fernandez Munoz, who also helped me with the thesis. The other interns Felix van Dieijen, Marijn Abrahamse and Einte Kamstra for the company and the discussions we had during lunch.

The thesis was a combined project with the TU Delft. Mirek Kaminski gave me the inspiration and subject for this project and guided me from a distance, I would like to thank him deeply for his efforts. In this time period there was a change of daily supervision. First Paula van Lieshout helped me to really understand the fatigue phenomenon. Later Lotfollah Pahlavan took over as mentor and helped me to truly understand the acoustic emission. I would like to thank them both for their formidable guidance and helping me to finish this thesis. In this thesis tests were performed on the Hexapod and I would like to thank Gabrielle Bufalari for helping with these tests and all the info he provided. The last person I would especially would like to send my gratitude to is Bart Scheeren, who funny enough I mentored in his first year of his studies, for all the guidance he gave me when he was graduating and when he became a PHD on the acoustic emission subject. He helped me I great extent of this thesis.

Finally I would like to thank my family and friends who helped me through this hard period and Liza van Kempen for designing my placard seen above. But special thanks to my girlfriend Elise Schiltkamp who supported and helped me persevere during this period but who also was graduation in this same period and is graduating a day after me.

Hope you will enjoy your reading of this thesis.

S.E.M. Brummel
Delft, August 2018

Abstract

In the field of fatigue testing in laboratory conditions, the common practice is uniaxial testing (i.e. in tension). The real-life loads on structures are usually not limited to one direction but contain multiaxial components. For this kind of testing, the ship and offshore structures department of Delft University of Technology developed a machine that is capable of exciting stresses in a specimen that resembles real life. A preliminary study has been conducted for the feasibility of using the acoustic emission method for monitoring fatigue on this multiaxial testing machine and in specific on a tubular double-side welded T-joint in offshore applications. This method is a tool to help to understand the fatigue progress in the material during testing.

Fatigue is a process by which damage is caused under cyclic loading below the yield stress. This phenomenon initiates on a microscale were dislocations accumulate and grow into a crack. The crack can grow until the structural integrity fails in complete rupture. The fatigue lifetime may be predicted; this is done with the help of uniaxial fatigue models. For multiaxial fatigue these models are not accurate and therefore a multi axial fatigue model should be developed. The crux here is to do these experiments to gain knowledge of the multiaxial fatigue to develop an accurate model for multiaxial fatigue.

The acoustic emission method is a non-destructive evaluation method that can help to determine the condition of a structural component. The acoustic emission signals have features that contain information on what is going on in the material. Feature extraction can also give insight to the fatigue lifetime. In addition, the acoustic emission signals can be used for localization of the damage. The localization calculation is done by comparing different times of arrivals and with this information the source can be localized. If this localization and tracking of the fatigue crack can be achieved on the multiaxial testing machine the new prediction models that are developed at the university can be more rigorously evaluated.

Combining the knowledge of fatigue and acoustic emission method, the following main research question is formulated: *“Is it possible to detect a fatigue crack with the acoustic emission method, and how can the crack length and position be estimated in the tubular welded T-joint specimen multiaxial loading?”*

Before the main question could be tackled, the background noise of the testing machine is measured for possible interference for future test. The second sub-question is: What features of the acoustic emission signal can be acquired and processed robustly for the tubular specimen? The last sub-question is: What are the essential features of the acoustic emission signals released by fatigue cracks under multiaxial loading? This last question could not be answered because there were no multiaxial experiments during the duration of this project. However, the methodology presented here as shown on a uniaxial case is believed to be directly applicable for multiaxial loading cases as well

Three experiments were performed of which one uniaxial test was used for detailed acoustic emission analysis. The data was analyzed with localization of the fatigue crack in the specimen. The localization of the crack and tracking its position is shown to be possible when the data is of sufficient quality. The difference in the estimate of the crack size by acoustic emission and the measured crack length turned out to be smaller than 10% when the crack reached its maximum length.

Content

List of figures

List of abbreviations

AE	Acoustic Emission
PSB	Persistent slip bands
TU Delft	Technical University of Delft
RMS	Root mean square
PLB	Pencil lead break

List of symbols

Latin:

a	crack length
B	thickness of material
C	Elastic constant
c_g	the speed of the dominant wave mode
c_{S0}	group speeds of the fundamental guided wave modes S0
c_{A0}	group speeds of the fundamental guided wave modes A0
d	average grain diameter
k_y	strengthening coefficient
m	slope of SN curve
M_k	stress intensity magnification factor
N_g	number of cycles
v	British standard variable
w	British standard variable
x_c	x-axis coordinates of AE source
y_c	y-axis coordinates of AE source
Y_{fm}	far field factor for membrane stress
z	initial crack length

Greek:

σ	stress range
σ_0	material constant for the initial stress for the dislocation movement
σ_y	yield stress
Ω	physical domain under inspection
ω	frequency

1. Introduction

The aim of this research is to evaluate the potential of using the acoustic emission (AE) method for fatigue monitoring of a tubular welded specimen. The application of a system of sensors to detect stress waves is the AE method, when the material undergoes irreversible changes, such as developing fatigue cracks. Therefore, in this research, the motivation for detecting fatigue damage stems from the need for a better understanding of fatigue stress under multiaxial loading. Traditional fatigue testing is conducted in tension and sometimes with torsion or, in unique cases, a combination of the two scenarios. The 4D-fatigue testing approach (three spatial dimensions plus the time dimension) to multiaxial fatigue of specimens is tested to an even smaller extent. The time dimension with a variation of parameters in multiaxial fatigue testing has not been standardized; therefore, research is still needed for understanding what happens when a structure is under cyclic multiaxial loading.

This report begins with a literature review that highlights the fatigue principles and the acoustic emission method. A subsequent section on fatigue principles closely examines the development of fatigue during the lifetime in steel. In the section on the AE method, the wave propagation and characteristics of the AE signals are elaborated. After the literature review, the following chapter concerns the research related to the primary research question, which is the following:

Is it possible to detect a fatigue crack with the AE method, and how can the crack length and position be estimated in the tubular welded T-joint specimen for multiaxial loading?

In this research, several tests were conducted on the Hexapod (see Figure 2), which is a Stewart platform commonly used for fatigue testing in six degrees of freedom. The specimen that was used in this research is shown in in Figure 1 (before being set up with AE sensors). In general, before fatigue measurements are performed, the background noise of the hexapod should be assessed, and the first subquestion pertains to this process:

1. *What is the ultrasonic background noise of the Hexapod, and in what way does it interfere with AEs from the fatigue cracks in the test specimen?*

Once the first subquestion is addressed, the following two subquestions can be investigated:

2. *Which features of the signal can be acquired and processed robustly for standard welded T-joints in laboratory conditions?*

3. *What are the essential features of AE signals released by fatigue cracks under multiaxial loading?*

Figure 1 Picture of the double side welded T-joint specimen

Figure 2 Picture of the hexapod at the TU Delft

2. Literature Review

2.1. Fatigue Principles

In the process of fatigue, a structure or welded connection is subjected to repeated, cyclic stress below the yield stress, which ultimately leads to the materials failing. This phenomenon can be divided into three phases:

- Crack initiation
- Crack growth
- Fracture

In this chapter, two phases of fatigue, initiation and crack growth, are explained for metallic materials (see Figure 3 for all of the steps of the fatigue lifetime). The final phase, failure, is not investigated because it is not relevant to this research. Before the full fracture the ship have had a planned maintenance to find cracks in the crack growth phase. These cracks then are repaired. If the ship has too much fatigue damage the ship is decommissioned, this is usually after 25 years.

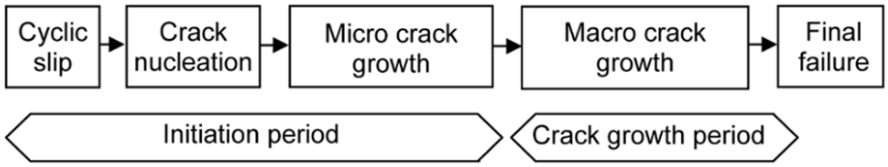

Figure 3 Different phases of the fatigue lifetime (Schijve, 2009)

2.1.1. Fatigue Initiation

Initiation, the first phase, usually has the longest duration in the fatigue process, and the length of this phase is highly unpredictable. If a material has defects from the production process, the initiation phase is shorter than it is for near perfect material. Before looking at what happens at a microscale, the stresses on the grain and the entirety of the material are discussed. On a macroscale, the material has a homogeneous and isotropic behavior, but at the mesoscale, the material is inhomogeneous and anisotropic (see Figure 4). The unequal distribution of the axial stresses causes internal shear between grains. Dislocations move when the shear force applied to them is greater than the shear force they themselves introduce to the lattice (see Figure 5). Following the dislocation movement are complex dislocations that move from one grain to another, and the stress needed for crossing this boundary can be determined with the Hall-Petch equation (see equation 2.1). this equation is governed by dislocation pile up at the grain boundary and a spill over when too much piles up. Another mechanism that these dislocations hit the grain boundaries, which are usually essence a grain boundary is a grain misalignment combined with some rather arbitrary but structured filling of the space in between or shared by the grains. than the inner part of the grain, resulting the slip plane's not leaving the grain in a continuous slip. The neighboring grain, in most cases, has a different orientation.

$$\sigma_y = \sigma_0 + \frac{k_y}{\sqrt{d}} \qquad (2.1)$$

Where σ_y is the yield stress, d is the average grain diameter, σ_0 is the materials constant for the initial stress for the dislocation movement, and k_y is the strengthening coefficient (a constant specific for each material) (Hall, 1951) (Petch, 1953).

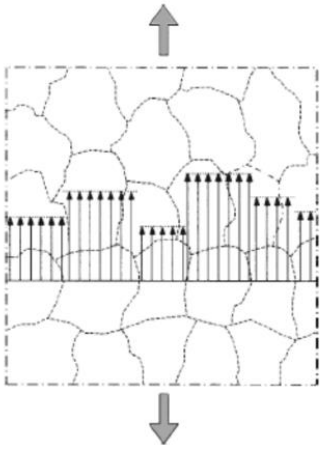

Figure 4 Simplified picture of the inhomogeneous stress distribution from grain to grain due to elastic anisotropy (Schijve, 2009)

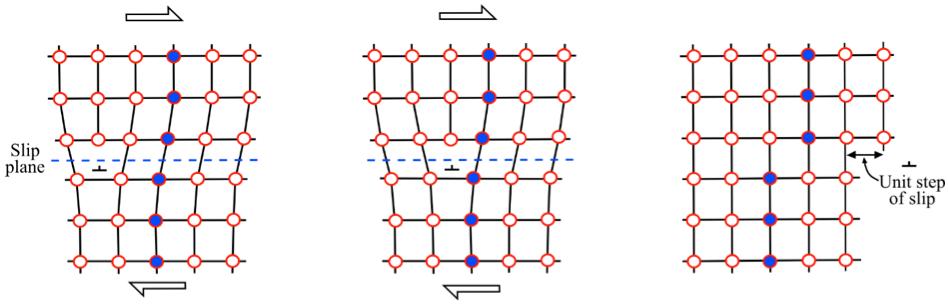

Figure 5 A schematic representation of the movement of a dislocation in a crystal structure (Passchier & Trouw, 2005)

The result of dislocation movement under continuous cyclic loading is that the dislocations end up at the exterior boundary of the material. Here, the dislocations cause microscopic slips of the lattice; this happens because forces from the air or external side of the grain boundary are almost nonexistent. This slip manifests in a persistent slip band (PSB) under cyclic loading (see Figure 5). PSBs cause microscopic stress concentrations. If they occur in a spot were a macroscopic stress concentration occurs, such as a notch in the geometry, then these conditions provide a probable point for crack nucleation (see Figure 7). The angle of the slip planes for tension is 45 degrees, and for torsion, this has an angle of 0 or 90 degrees, as shown in Figure 8.

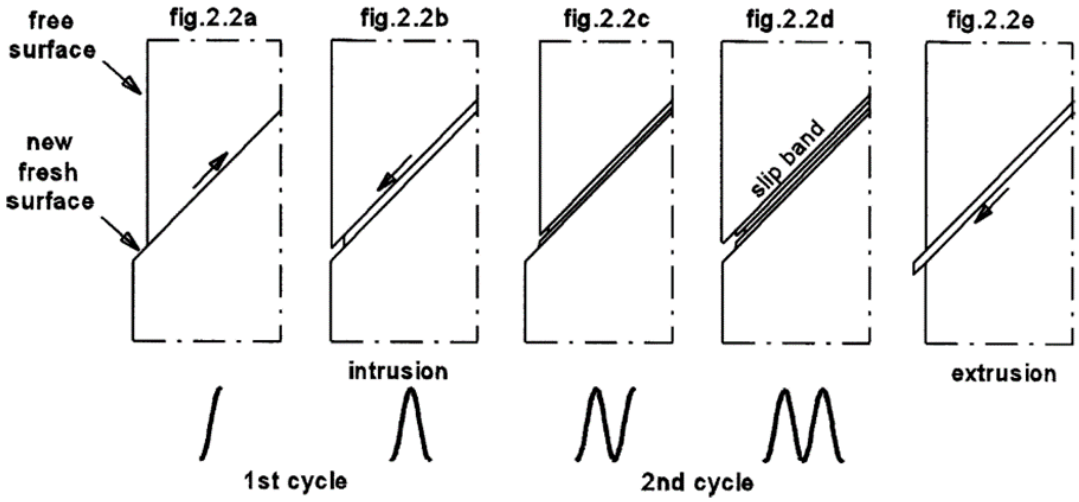

Figure 6 Cycle slip leads to crack nucleation (Schijve, 2009, p. 16)

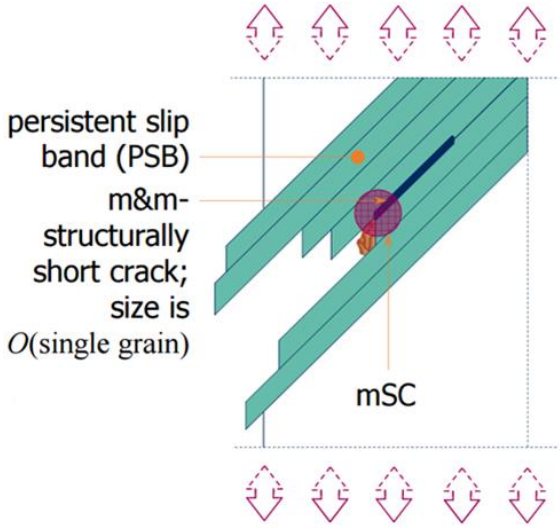

Figure 7 Beginning of a micro-crack in a PSB

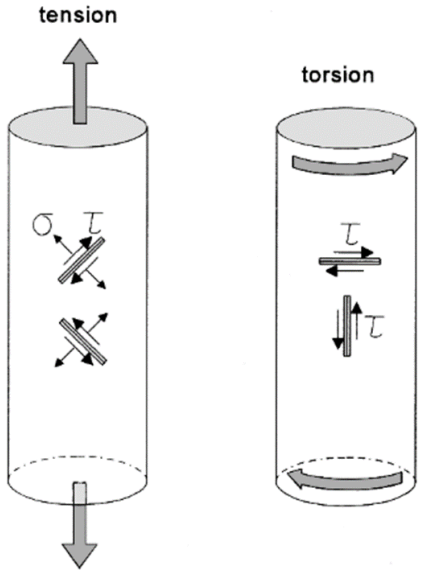

Figure 8 Slip planes with maximum shear stress (Schijve, 2009, p. 47)

The PSBs roughen the surface because of the intrusions and extrusions that develop (see Figure 7). The whole process is irreversible because of the hardening of the material inside the PSBs, which is caused by plastic strain. The impurities and imperfections make the material weaker, and these irregularities are to the edge of the grain. The movement of the defects to the edges purifies the material from within, making it stronger on the inside than on the outside, where the grain roughens (Schijve, 2009). The new surface that is exposed by the forming of PSBs then oxidizes. This process sets the planes; thus, the process is irreversible. In general, the deepest intruded slip plane has the highest microscopic stress concentration, which eventually breaks the bonds of the atoms between the two slip planes induced by microplasticity and creates a micro-crack (see Figure 7). This process takes place in a single grain but can occur simultaneously all over the external boundary of a material.

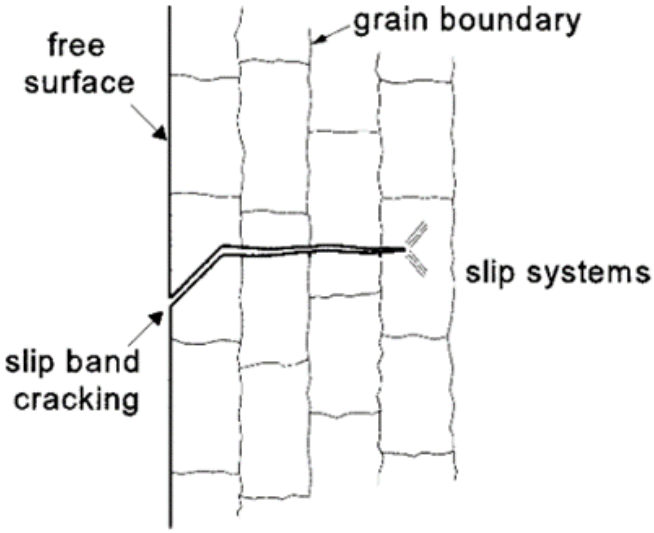

Figure 9 Cross section of a micro crack (Schijve, 2009, p. 19)

The development of a crack is governed by the shear stressors, and it follows the shear plane of 45 degrees for tension and 0 or 90 degrees for torsion. Later, the crack is governed by normal stresses and changes to 90 degrees for tension and 45 degrees for torsion (Schijve, 2009).

In the literature there is not a consensus on where the initiation phase transitions to the crack growth phase. Therefore four definitions are presented, that have been found in literature and in interviewing people. These definitions vary from a couple of lengths of a single grain to 0.2 mm. Choosing one of the definitions can substantially affect the accuracy of the method used for detecting the differences between the initiation and growth phases. This is because the smaller the criterion is, the harder it becomes to detect it. In addition to the existing definitions, AE can help define the differences between the two phases. Thus, a new criterion could be proposed that is based on the AE activity recorded during the fatigue experiments.

The four definitions of initiation-to-growth transition are the following

- "If the crack goes outside the first-grain, the initiation phase stops and the growth phase starts" (Schutz, 1996).

- "The engineering approach of this is that when the crack goes 0.2 mm into the material, it switches from initiation to growth" (Dragt, 2017).

- "When the grain boundaries do not affect the speed of the crack growth, this is the point that the initiation phase will go into the growth phase" (Schijve, 2009).

- "The shift from a (near) surface phenomenon to a material bulk property dependent material" (den Besten, 2017).

2.1.3. Fatigue crack growth

Crack growth is the second phase in the fatigue lifetime (see Figure 3). In this section, the definition that is used for further explanation is the one in which the crack outgrows the first grain (see the previous paragraph).

The crack continues growing until it hits another grain boundary; to cross this boundary, the crack needs a substantial number of extra cycles and extra energy to continue to the next grain (see Figure 10)

The microscopic stress concentration travels along the crack tip, where it breaks the bonds, and into the surrounding area. PSBs continue to form in the future path of the crack (see Figure 11). After

the grain boundary, the same crack propagates in a slightly different direction than it had in the previous grain because it follows the crystal orientation of the grain it is entering (see Figure 11).

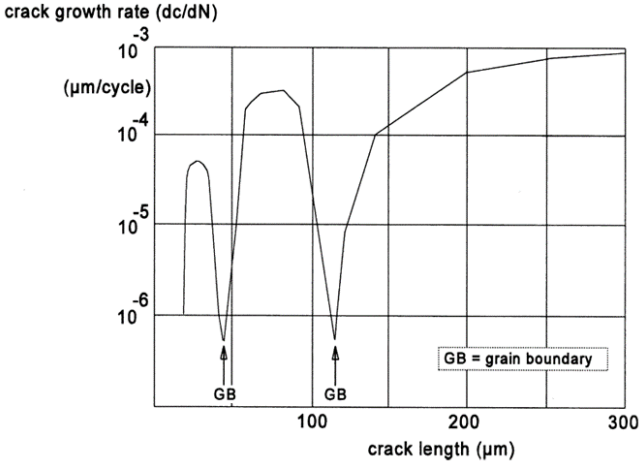

Figure 10 Grain boundary effect on crack growth in an Al-alloy. The crack length was measured along the material surface (Blom, Hedlund, Zhao, Fathalla, & Weiss, 1985)

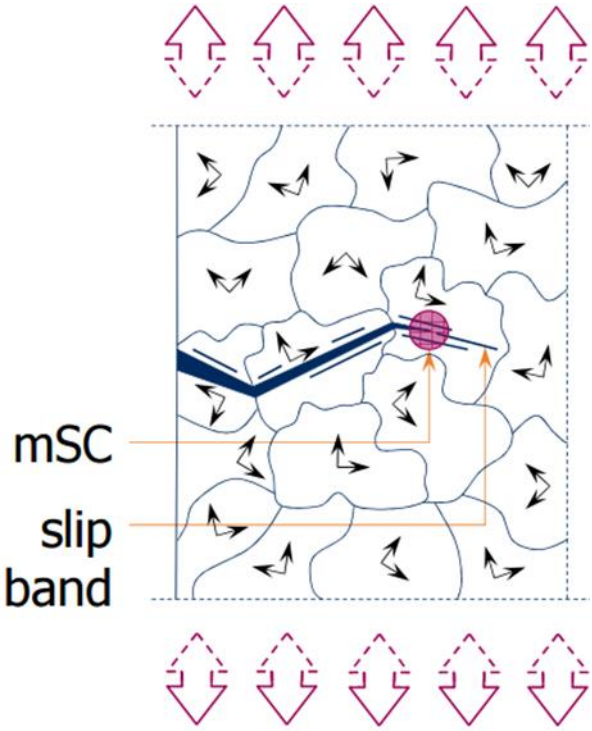

Figure 11 Microcrack going through different grains and changing directions (den Besten, 2017)

Eventually, the crack nucleation, which is a nonlinear mechanism on a microscale, moves into a short crack growth, which is a linear mechanism on the macroscale. Not all of the micro-cracks become macro-cracks; most of the micro-cracks end up stalling because the crack with the longest length in the near vicinity becomes the governing crack (Schijve, 2009). There is a possibility that there are multiple governing cracks. In Figure 12 there are two initiation point one on top and one on the bottom. Both have a stable crack growth this is lite grey, the dark grey is unstable crack growth. The crack grows and forms a crack front, and this is dependent on the material bulk property. The shift from a (near) surface phenomenon to a material bulk property dependent material can be seen as the switch from crack initiation to crack growth (den Besten, 2017); however, there are still many discussions for the exact definition.

In the crack-growth phase, the short crack grows into a long crack, and this represents stable crack growth. The growth of the crack eventually becomes unstable and thus grows faster and faster; this leads to the final fracturing of the structure. This is because the structure loses strength. The crack is a disconnection, and the same force is carried by less material; thus, a higher yield in the material that is not yet damaged also ruptures and fractures eventually.

.

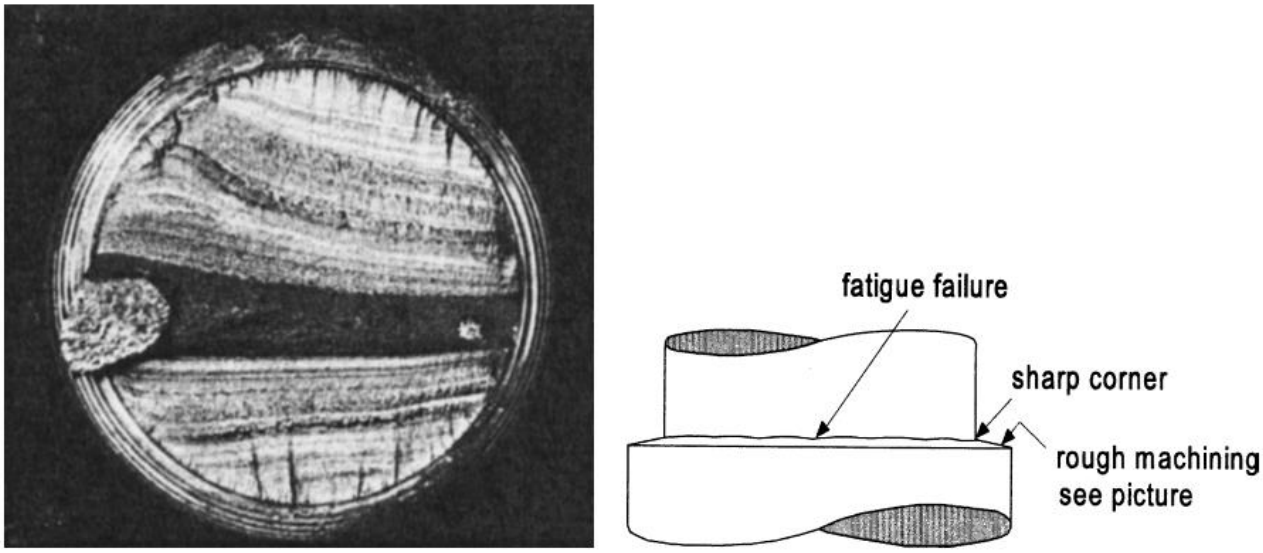

Figure 12 Fracture surface of a fatigue failure in the tiller of a sailing boat as a result of cyclic bending. Crack nucleation at several locations in the sharp corner edge. Overlap of crack nuclei produces lines in the crack growth direction (Schijve, 2009, p. 34)

2.1.3 Fatigue calculation

For the calculation of approximate number of cycles for stable crack growth the British Standards were chosen to calculate the fatigue. First the stress intensity factor is calculated for a double side welded geometry containing two notches with the presumption that the crack is elliptical (Figure 13).

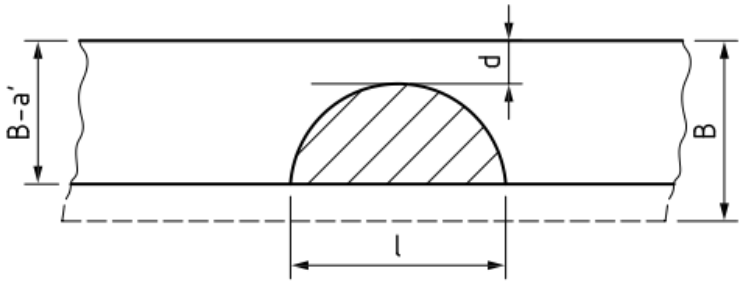

Figure 13 Elliptical crack (BS 7910:2013+A1:2015)

$$M_k = v\left(\frac{z}{B}\right)^w, down\ to\ M_k = 1 \quad (2.2)$$

For equation 2.2 M_k is the stress intensity magnification factor, v and w are calculated via the table in Figure 14, z is initial crack length and B is thickness of material.

Loading mode	L/B	z/B	v	w
Axial	≤2	≤0.05$(L/B)^{0.55}$	0.51$(L/B)^{0.27}$	−0.31
		>0.05$(L/B)^{0.55}$	0.83	−0.15$(L/B)^{0.46}$
	>2	≤0.073	0.615	−0.31
		>0.073	0.83	−0.20
Bending	≤1	≤0.03$(L/B)^{0.55}$	0.45$(L/B)^{0.21}$	−0.31
		>0.03$(L/B)^{0.55}$	0.68	−0.19$(L/B)^{0.21}$
	>1	≤0.03	0.45	−0.31
		>0.03	0.68	−0.19

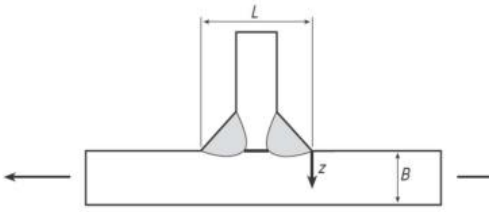

Figure 14 Far field coefficients for double sided weld with the geometry (BS 7910:2013+A1:2015)

Now the far field factor is calculation shown in equation 2.3. Using the geometry from Figure 15

$$Y_{fm} = \sqrt{\frac{2B}{\pi a}\tan\frac{\pi a}{2B}} * \frac{0.752+2.02\left(\frac{a}{b}\right)+0.37\left(1-\sin\frac{\pi a}{2B}\right)^3}{\cos\frac{\pi a}{2B}} \quad (2.3)$$

With these factor and knowing the C, the elastic constant, the stress range (σ) and m, the slope of SN curve. The number of cycles can be calculated (equation 2.4) for the length crack length a.

$$N_g = \frac{1}{C*\sigma^3} * \frac{1}{Y_{fm}*\sqrt{\pi a}^3} \quad (2.4)$$

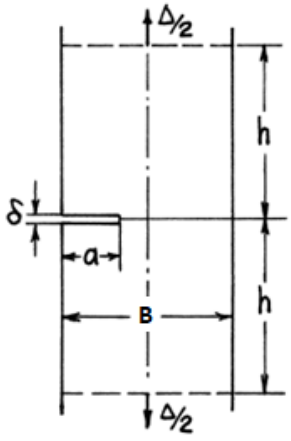

Figure 15 Geometry for far field factor calculation (Tada, Paris, & Irwin, 2000)

2.2. Acoustic Emission

AEs are a phenomena in which changes in the microstructure of a material generate stress waves, and it is used as a procedure for non-destructive testing. In this research, it is used to monitor and locate fatigue cracks in a tubular welded joint specimen. This section focuses on metals because the tubular welded specimen is made of S355 steel.

2.2.1. Background

Portevin and Le Chatelier (1923) reported small noises in the highly deformed aluminum that they were testing under high stress and called them “petit bruit sec.” This was one of the first modern mentions of the later known phenomenon of AE. J. Kaiser (1953) was the first scientist who researched the AE method extensively and is, therefore, considered the father of AE. However, Kaiser did not name the observed sounds as acoustic emissions but as “acoustic phenomena.” In addition, he discovered the irreversibility of dislocations. Later, Schofield (1961) did further research on the phenomenon and provided a detailed explanation of AEs and gave the phenomenon its current name.

Today, the AE method is used to monitor system integrity and production processes, and it is a non-destructive method of monitoring. The primary use of these sensors is to monitor changes in the microstructures, but they can also detect friction and leakage, as well as other pseudo sources. All of these sources can be recorded by sensitive piezoelectric transducers—that is, sensors. The AE method is a way of listening to the material under investigation, and the system AE uses is passive; this means that the material has to be excited via elastic waves.

2.2.2. Stress waves propagation

Stress waves are generated by the sudden release of elastic energy in solids, where the dimensions of the domain are larger than the wavelengths. For thin walled structures these are lamb waves. These waves can be divided into two types: The first is pressure waves (P-waves), which are similar to acoustic waves and, therefore, dilatational. The second is equivoluminal waves, which occur only in solids because of their capability of transferring shear forces. These waves are distortional, and they are also called shear waves (S-waves). Both types are shown in Figure 16.

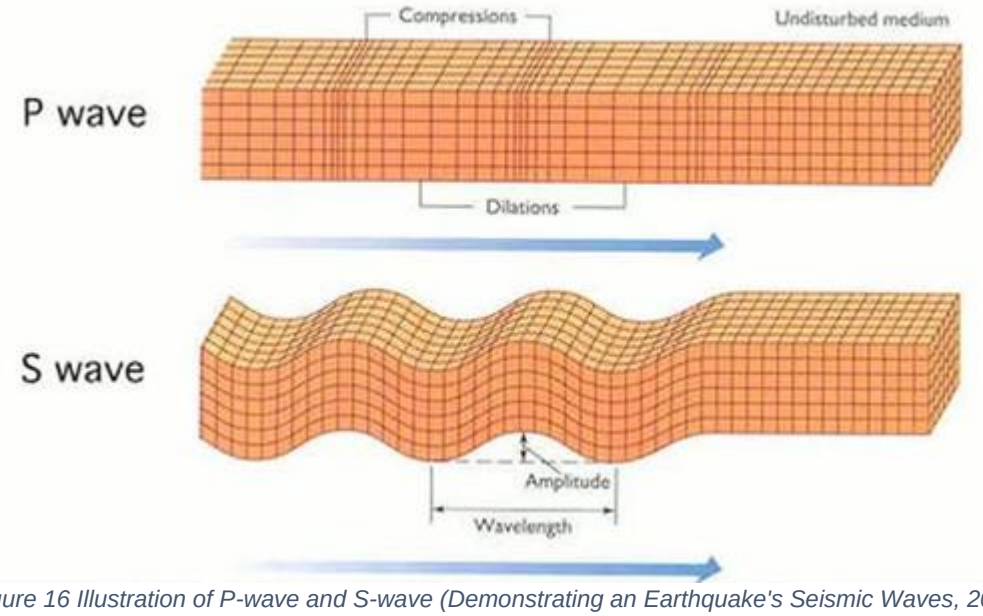

Figure 16 Illustration of P-wave and S-wave (Demonstrating an Earthquake's Seismic Waves, 2017)

The interaction of P- and S-waves with a boundary between two materials or phases (in this case, a solid medium and a gas) generates a surface wave, or Rayleigh wave only in case of a solid-gas interface. This type displaces the free surface of the solid and can, therefore, be observed outside of the medium. AE testing and seismology are based on this principle, with the ultimate goal being to observe the behavior of a surface to deduce what is occurring inside of the material. The particle motion in a Rayleigh wave is elliptical and constrained by the elastic properties of the surface, as shown in Figure 17.

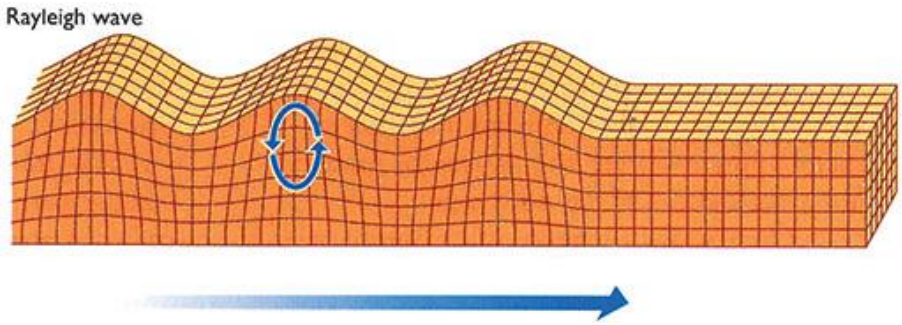

Figure 17 Rayleigh wave (Earthquake: Body Waves & Surface Waves, 2017)

In thin-walled structures, elastic waves may propagate as lamb waves, which occur in a geometry that has two closely spaced boundaries—for example, a plate. The interaction of pressure and shear waves with the free boundaries on both sides of a medium can generate two unique types of Lamb waves—symmetric and antisymmetric (see Figure 18).

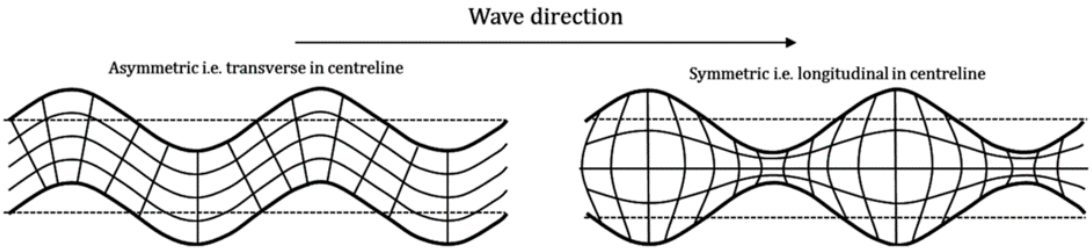

Figure 18 Types of Lamb waves (Marks, 2016)

The Lamb waves can be a higher order of wave modes, which typically carry little energy and are observable only in special conditions. This way, the focus is often put on zeroth-order modes. Low frequency modes are characterized by wavelengths longer than the plate thickness. In general, the zeroth-order modes are considered to be in this lower-frequency ranges. In the low range, the symmetric wave mode is referred to as an extensional mode. Often symbolized as S_0, the antisymmetric wave mode is referred to as the flexural mode, often symbolized as A_0. This for zeroth-order modes in AE applications, the S_0 mode often carries less energy than the A_0 mode; therefore, the A_0 has a dominant amplitude.

A wave originates from a point source and consecutively propagates throughout a medium. In an isotropic material, the velocity of the elastic waves is equal in all directions, unhindered by the local grain properties of polycrystalline materials (Rogers L. , 2001). This is because the wavelengths are significantly larger than the grain size of the material. The speed of the wave propagation depends on the mechanical properties of the material and, in the case of thin-walled structures, on the relation between the elastic properties and the frequency. The elastic waves separate into individual frequency components because each has its own propagation velocity. This relationship between velocity and frequency is referred to as the dispersion relation. The S_0 and A_0 are affected differently by dispersion, as shown in Figure 19 for steel with a material coefficient E=355 MPA.

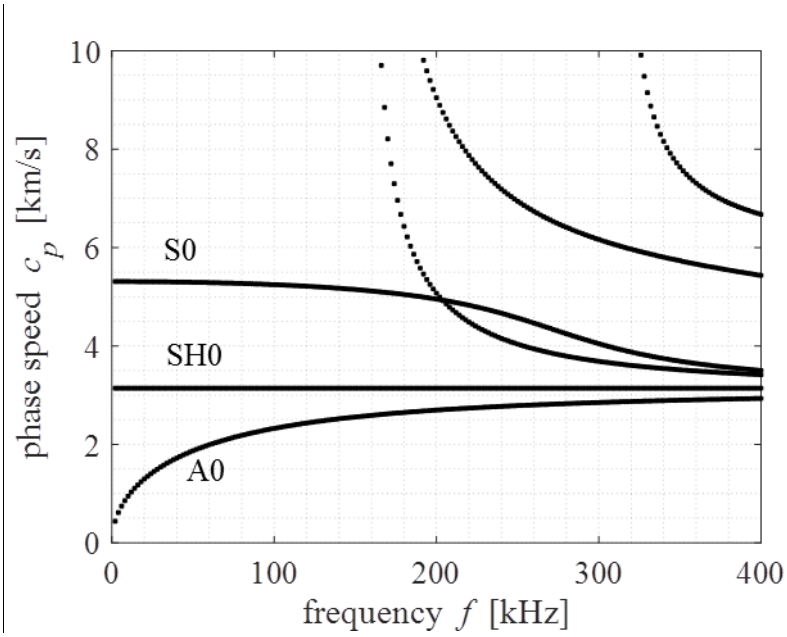

Figure 19 Graph of the dispersion relation of steel for thickness of 10 mm

The velocity of an A_0 component increases with an increasing frequency, but the velocity of the first arrival waves (S_0) decreases with the increasing frequency. At low frequencies, the second arrival waves (A_0) travel at 60% of the speed of the first arrival wave's velocity. This property can cause a sufficient difference in the arrival times of both wave modes of the AE signal when a sensor has a sufficient distance from the source (see Figure 20).

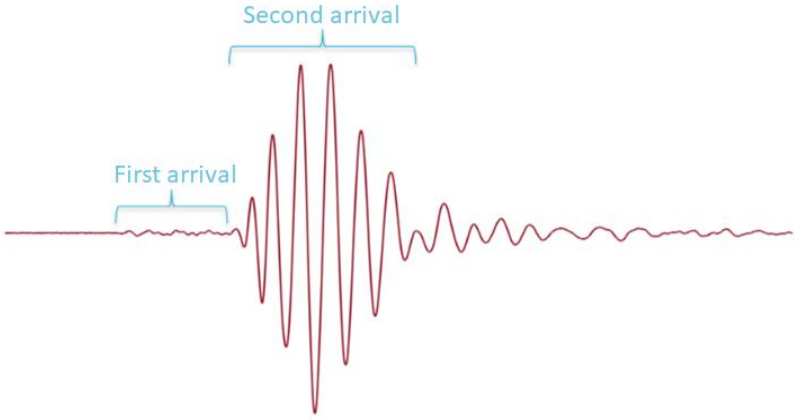

Figure 20 Typical recording of acoustic hit (Scheeren, 2017)

2.2.3. Parametrization of AE signals

The analysis of the recorded AE signals is based on the extraction of the features of the signals captured by the AE sensors. In this section, the different properties of the AE signals are explained.

If the different features are well understood, the signal analysis can be performed more thoroughly. Some features that are explained in this section are shown in Figure 21.

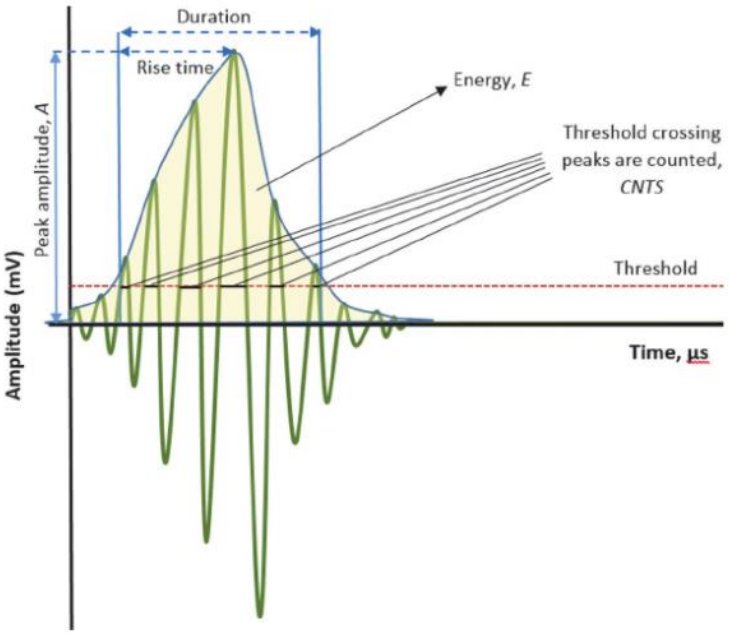

Figure 21 A typical waveform of an AE hit and the features (Sanchez-Molina, 2015)

The following features are shown in Figure 21:

Peak Amplitude: The largest absolute amplitude value of a recorded acoustic signal is the peak amplitude. The amplitude is recorded in the order of μV and is represented in the decibel scale dB_{AE}.

Duration: This is the time that the signal is above the threshold—that is, the time interval from the first time the signal is higher than the threshold to the moment the threshold is no longer crossed.

Rise time: This is the time between the first time the signal crosses the threshold and the peak amplitude.

Energy: If the signal of the hit is squared and the integral is taken, the energy is the result of the equation. This is done by summing up the squared sample values for the duration of the hit and multiplying the answer of the sum with the sampling time.

Counts: This is the number of positive threshold crossings that occurs for the duration of the signal (see Figure 21), so the number of peaks above the threshold are counted for the counts.

Time of arrival: The time of arrival defines the beginning of the acoustic wave and when the signal crosses the threshold positively for the first time. This marks the beginning of the hit.

Root mean square noise: The measurement of the background noise is called the root mean square (RMS) noise. This is calculated by obtaining a short sample of noise, It is typically calculated from a short sample of signal values in the period between two hits.

2.2.4. Acquisition of AE signals

In this project, the goal is to use AE signals to monitor fatigue. Detection of an AE signal is referred to as a hit, which is a signal that surpasses the threshold. If the noise from AE sensors were recorded continuously, the datasets would be of a considerable size (in the couple of hundreds of gigabits per day, especially in a long-term test, where the amount of the data can reach into the terabytes). Most of the recording noise is background sounds; the noise covers the potential fatigue signal, but post-processing these signals to obtain the potential fatigue signals is performed in this thesis. Therefore, the equipment has a threshold. In general, a threshold is set in relation to the background noise: The higher the background noise, the higher the threshold. The minimum of the threshold with the sensors is 27 db_{AE} to counter the analog to digital converter. When the threshold of the sensor is set lower, the sensor provides noise even when there is no physical sound.

2.2.5. Localization

Time picking

Time picking of the signal is crucial for the accuracy of localization. Time picking is a generalized term, it means that the onset of the signal is found by using a specific criterion. In this research, the criterion had two parameters that could be adjusted. The first was the noise window. In the first dozen microseconds, the signal was background noise. The first 20 microseconds of a recorded signal were used to obtain a base level for the background noise. The maximum value in that period is used for the baseline of the threshold. The second parameter is the threshold factor, which is the multiplication factor of the baseline threshold value. The factor varied from 2 to 100, depending on the signals in the event.

In this research, the time picking was done manually, meaning that every event with multiple hits was checked and adjusted if needed, so the signals were time picked at the same point of the waveform (see Figure 22). If the hits of an event are picked at different points, doing so can significantly influence the calculation of the position of the signal's source, because it is calculated on the basis of the different times of arrival. This is why the time picking was done manually and not automated for this research. In general, when the time picking is adequate, the next step of the calculation can be performed.

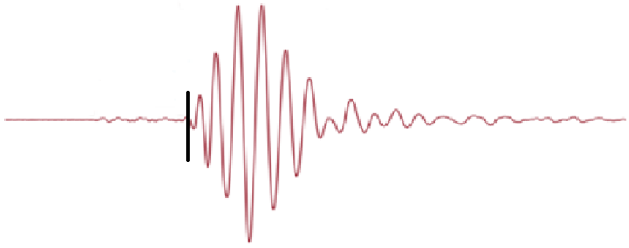

Figure 22 Different time-picking locations on a random signal

Event building

Localization was done for the event, which consisted of multiple hits, and these were produced by the same source. The first hit was the base of the event. The differences in time among the many sensors then made the whole event. The hits had a maximum time difference of 150 microseconds, a setting that was specific for the tubular welded specimen.

Calculation of position

The calculation is a multilateration scheme, meaning that the source was localized on the basis of the differences among the times of arrival for the sensors (see Figure 23). Therefore, the time-picking accuracy was integral to achieving localization accuracy. Different times of arrival led to divergent calculated locations of the source.

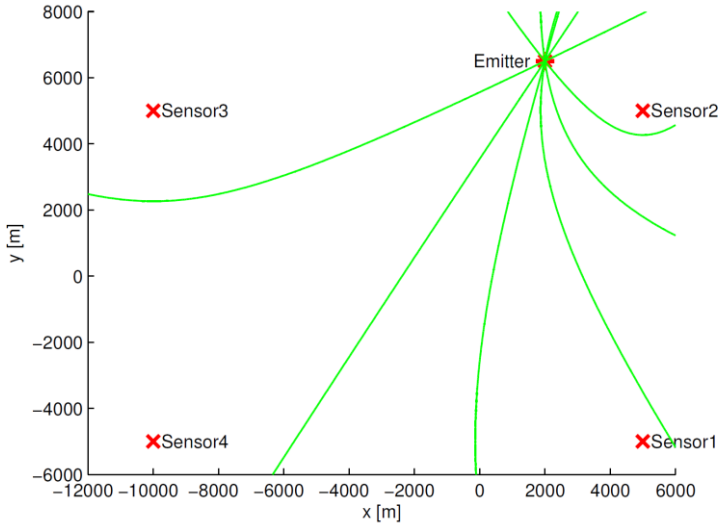

Figure 23 Intersecting hyperboloid sheets showing the time differences of the arrival-based source localization (Steffes, 2014)

The equations used in the calculation

The basis of the localization formula is to use the time difference of arrival in a minimization. The time difference between all the sensors.

$$\arg\min_{x,y,c_g} F\left(x_c, y_c, c_g, \Delta t_{ij}\right), \forall i,j \in [1,2,\dots,n], subject\ to: (x,y) \in \Omega\ and\ c_g \in [c_{S0}(\omega), c_{A0}(\omega)] \quad (2.4)$$

Where;

$$F\left(x_c, y_c, c_g, \Delta t_{ij}\right) = \sum_{j=1}^{n}\left(\Delta t_{ij} - \frac{1}{c_g}\left[\sqrt{(x_i - x_c)^2 + (y_i - y_c)^2} - \sqrt{\left(x_j - x_c\right)^2 + \left(y_j - y_c\right)^2}\right]\right)^2, \forall i \in [1,2,..,n] \quad (2.5)$$

Where x_c and y_c denote the coordinates of the AE source in the plane if the geometry, c_g is the speed of the dominant wave mode, Ω is the physical domain under inspection, c_{S0} and c_{A0} are the group speeds of the fundamental guided wave modes S0 and A0 as function of frequency ω, and F is the generic functional form of the error function associated with the assumed combination of the source localization, speed of the dominant wave mode, and the time picked arrival times of the wave. (Pahlavan, Paulissen et al, 2014)

2.3. State of the art

The AE method had its boom in the 1980s. After this period, it was researched scarcely. In recent years, computer technology has made considerable advances; in particular, large numbers of waveforms can be stored, and all the features can be extracted. Combined with improved sensors, the technology has renewed interest in the relevant research.

In this chapter, the state of art of the AE method is discussed, with a focus on structural-health monitoring and the localization of the crack front.

2.3.1. Structural-Health Monitoring

The AE method is applied mostly in the field of structural-health monitoring and for manufacturing processes. The primary function is to detect fatigue damage and leakage in the structure of pressure vessels.

The localization research is done on a macroscale; therefore this research is focused on finding the position of the fatigue damage in a structure by using multilateration; thus a preliminary study has been done on how accurate the localization can get, the accuracy was in the range of 1mm (Scheeren, 2017). A recent study examined the complexity of thin-walled geometries and determined a method that could

not only make the localization less complicated but also increase the accuracy to decimeters (Pahlavan, Paulissen, Pijpers et al., 2014).

In feature research, waveform parameters are analyzed to evaluate the severity of fatigue damage. This type of analysis was done in a recent study where a distinction was found in the AE signal of a concrete anchor pull-out test, and the distinction could potentially enable the fracture mode to be predicted (Nguyen, Vantomme, & Aggelis, 2016). Another study that is highly relevant to this thesis is "Monitoring on a Mooring Chain Using Acoustic Emission Testing" (Lee, Botten, van der Horn, & Wang, 2013). This study identified quantitatively the differences between crack initiation, crack propagation, and the final fracture, and the identifying was is performed by comparing the different parameters in the different phases.

2.3.2. Crack-front localization

Using AE signals to locate crack fronts is a revolutionary technique. The method digital-image correlation is used to find the crack front inside the material being used, but the method is still in the experimental phase. However, it obtains data from the surface of the specimen and then uses mathematics to reconstruct the crack inside the material. In the AE method, the crack front of a fatigue crack can be tracked by listening to what is occurring inside the material directly by recording on the surface, without derivations of the surface.

2.4. Knowledge gap

In this chapter, the knowledge gap is identified.

Research on determining a qualitative approach to define initiation and growth in acoustic emission

First, it should be mentioned that little research has examined the phase definitions of metal fatigue by using AEs. Only one study was found on this topic. Thus, the present study is pioneering work, and the knowledge gap is considerable in this field. That one particular study implemented monitoring of a mooring chain (Lee, Botten, van der Horn, & Wang, 2013), and the result was derived quantitatively. Furthermore, the mechanisms in the signal were only looked at per parameter per phase for this particular experiment. No clear definition was provided for the initiation signals in different situations, nor was one provided for a growth signal. The fracture signal is not interesting to examine in depth because when the fatigue process eventually produces a fatigue crack, that crack is detected usually. Thus, the goal of this study is to find a method that is applicable to all types of geometries and is easy to use. To fill the knowledge gap, a clear method that can define a signal in its particular phase is needed. Preferably, the distinction between crack initiation and crack growth can be seen as a threshold where on one side it is initiation and the other growth. This will rather be a gray zone where the signal can be both. The main goal is to minimize the gray zone or interval.

Acoustic emission method for fatigue monitoring of a multiaxial fatigue-testing machine with new limits

The traditional way fatigue is tested is with tension. There are multiaxial and torsion-testing machines but not in the order of 1 MN and 30 Hz. Applying the AE method in such a machine has never been done. Thus, a study must be done to determine the feasibility of tracking fatigue in these conditions.

Conclusion

In the ideal case, the difference between initiation and growth can be detected. Because there is not a clear definition of this border and because the AE method has not been used on a multiaxial testing machine, the focus of this thesis is an exploratory study.

3. Research

This chapter explains the equipment that was used in the experiments, as well as the tests that were conducted.

3.1. Equipment used in the experiments

This section introduces the testing machine used, the Hexapod, and explains the AE equipment.

3.1.1. The Hexapod

The TU Delft Hexapod (see Figure 24) is a combination of a Stewart platform with six hydraulic actuators as legs and a hexapedal load cell. With these legs, the top part of the Hexapod can move with six degrees of freedom. The Hexapod is a special kind of machine, and the Stewart platform is used for dynamic testing or the simulation of vehicles that require large movements and small forces. However, the Hexapod generates large movements and high forces to replicate the impacts that marine structures endure because of the changing weather conditions, and it is unique for its kind. The forces can go up to 1 MN, with a frequency up to 30 Hz. The hexapedal load cell is situated under the Stewart platform and records the forces acted on the specimen.

Figure 25 shows the different parts of the machine. For a better understanding of the different parts, the following provides a top-to-bottom explanation. First, there is a total of 12 cylinder hinges at the top of the Hexapod. The traverse connects the top six hinges to each other; the other six are connected to their own bases. The soupplate connects the traverse to the top of the specimen. The bottom of the specimen is connected to the bell, and the bell enables a smooth transfer of stresses to the hexapedal load cell, which is then connected to the floor via the foundations of the .

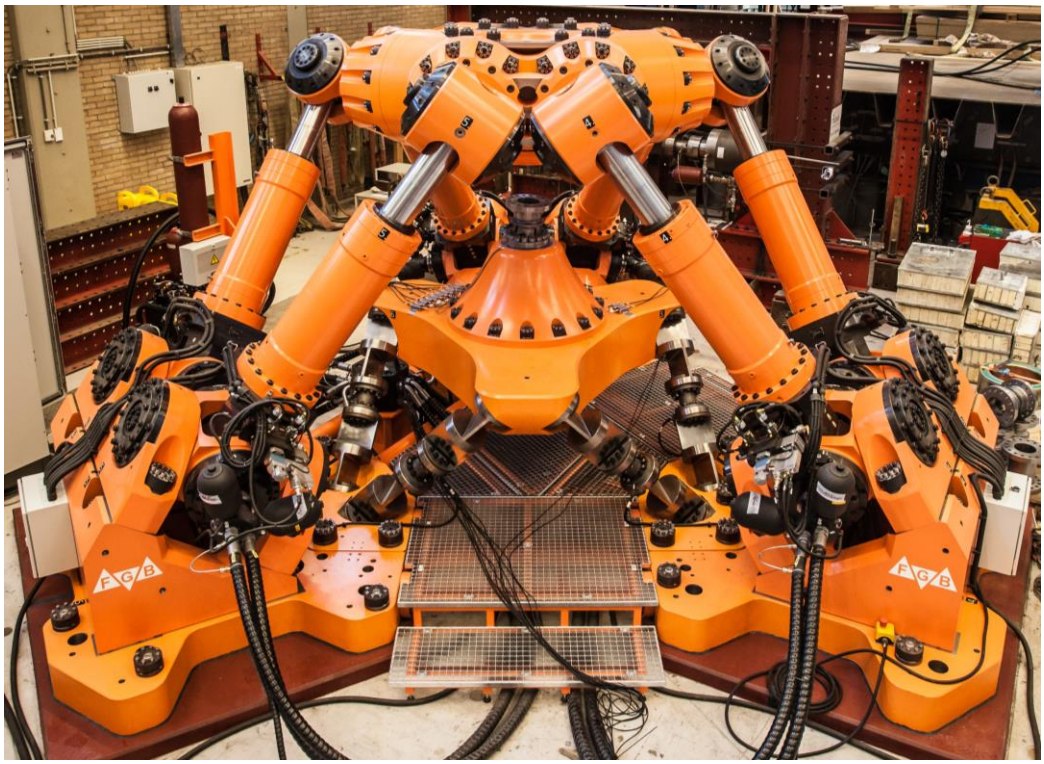

Figure 24 Render of the TU Delft Hexapod (TU Delft, 2018)

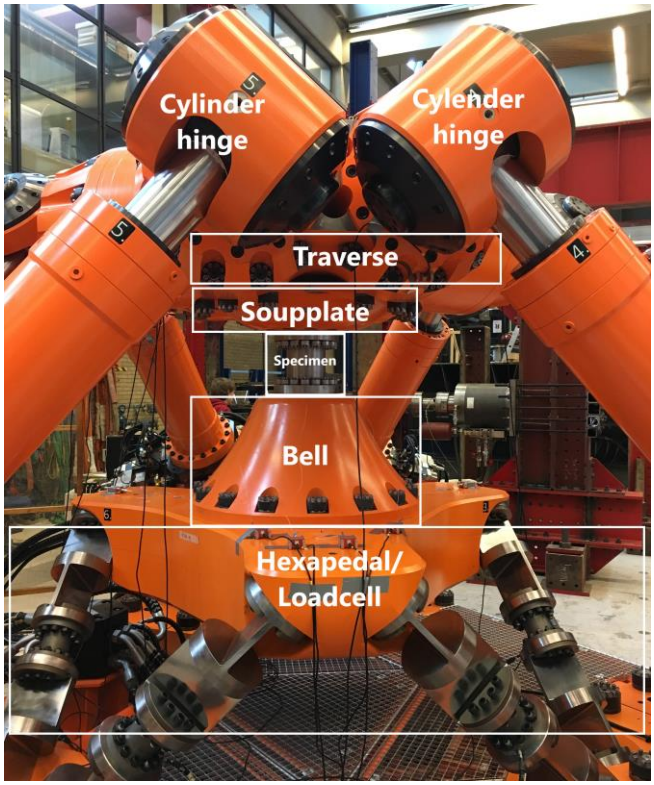

Figure 25 Side view of the Hexapod

3.1.2. The acoustic emission measurement system

There are various types of AE sensors on the market. In general, the larger sensors have a broad resonance frequency range but small sensors only have a high resonance frequency (see Figure 26 for the size differences). The smaller 600 kHz transducers of type VS600-Z2 were used in this research because they could be used on cylindrical specimens with different diameters without the need for disruptive transition pieces.

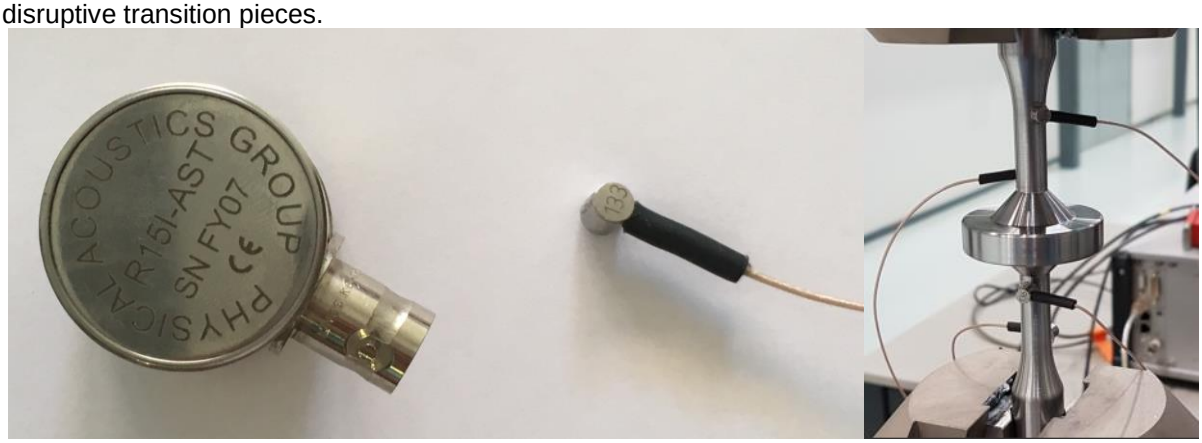

Figure 26: 150 kHz sensor versus 600 kHz sensor and the bar specimen with 600 kHz sensor

The equipment used is produced by Vallen Systeme GmbH (a company that specializes in AE equipment). The AMSY 6 Acoustic Emission Measurement System was used for data-acquisition. This system is suitable for frequencies in a range of 2 kHz to 2.4 MHz (Figure 27). It has two settings: the 2 kHz to 18kHz and the 18 kHz to 2.4 MHz. For this study, the second option was used. Therefore, the receiver was set up in such a way that it would not pick up the frequency of audible sound (Figure 27).

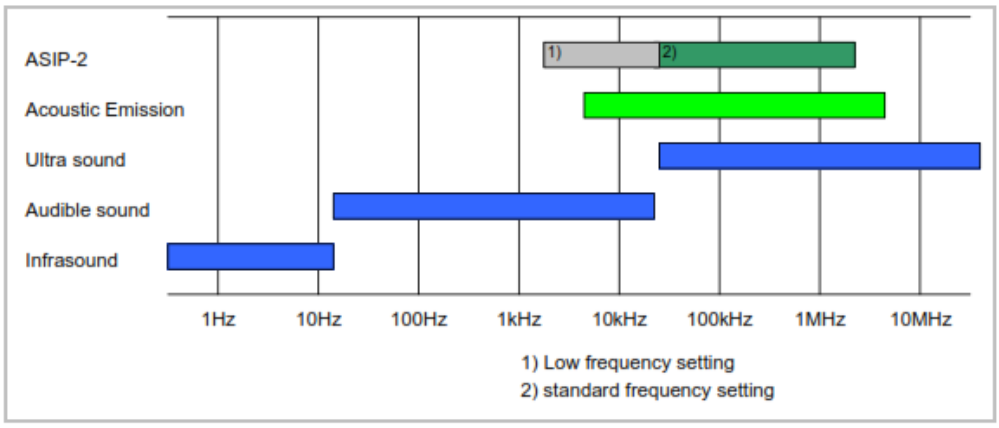

Figure 27 Frequency ranges of infra-, audible, and ultrasound (Vallen Systeme GmbH, 2015, p. 6)

The AMSY-6 system has 18 parallel measurement channels and a PC running with system front-end software that is part of the measurement system. The AE-sensor type is a VS600-Z2 piezoelectric transducer (see Appendix E for full specifics). This system also has AEP5H preamplifiers with 40 dB gain and ASIP-2 signal processing cards (see Figure 28). The system comprises analog-measurement sections, analog-to-digital conversion units, and a digital-signal processing unit.

Figure 28 AE sensor, AEP5H preamplifier and box containing ASIP-2 cards (left to right)

The architecture of the measurement system is shown in Figure 29. The chassis was connected to a USB hub, which sent the data into the computer. The data were preprocessed with Vallen AESuite Software. The resulting information was put into a database that could be read with VisualAE or Matlab with an Sqlite3 MEX.

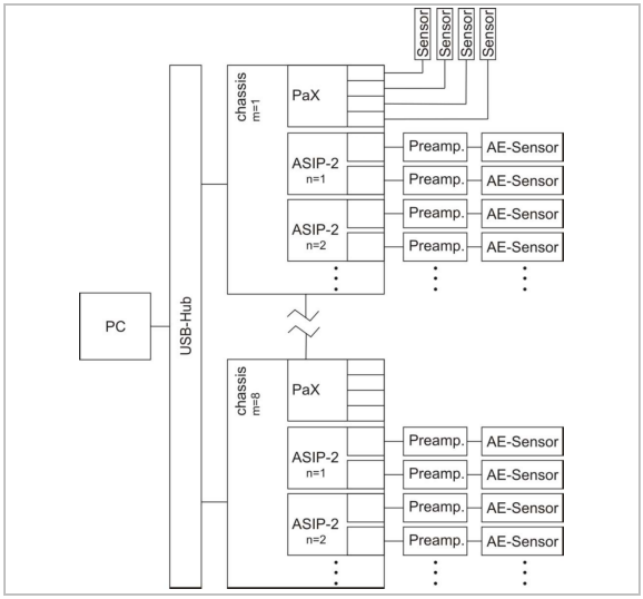

Figure 29 The block diagram of AMSY-6 measurement system (Vallen Systeme GmbH, 2015, p. 9)

3.2. Characterization of the test machine

Before the start of the experiments, the background noise of the Hexapod needed to be characterized in an initial test.

Positioning of the AE sensors

The goal of the characterization test was to measure the background noise. Therefore, the potential sources of noise of the machine were located and quantified. The decay of the signal through the machine toward the specimen was determined as well. This section explains which locations were selected for the sensors and the reasoning behind the choices.

The Hexapod had three identical corners. The measurements focused on specific sources of noise for one of these corners. The sources of noise could be anywhere around this corner section. Two extra sensors were placed on the other two corners and were used to identify the potential sources of noise that came from these corners. There were 17 individual AE sensors available for testing, and they were positioned in the manner shown in Figure 30. Eight sensors were allocated for source localization in these corners. Two sensors were used to detect signals that might come from the other two corners. Three sensors were placed on the load cell (see Figure 25) to measure the noise. One sensor was placed on the ground to determine signals coming through the ground into the Hexapod. Three sensors were placed on the centerline of the specimen.

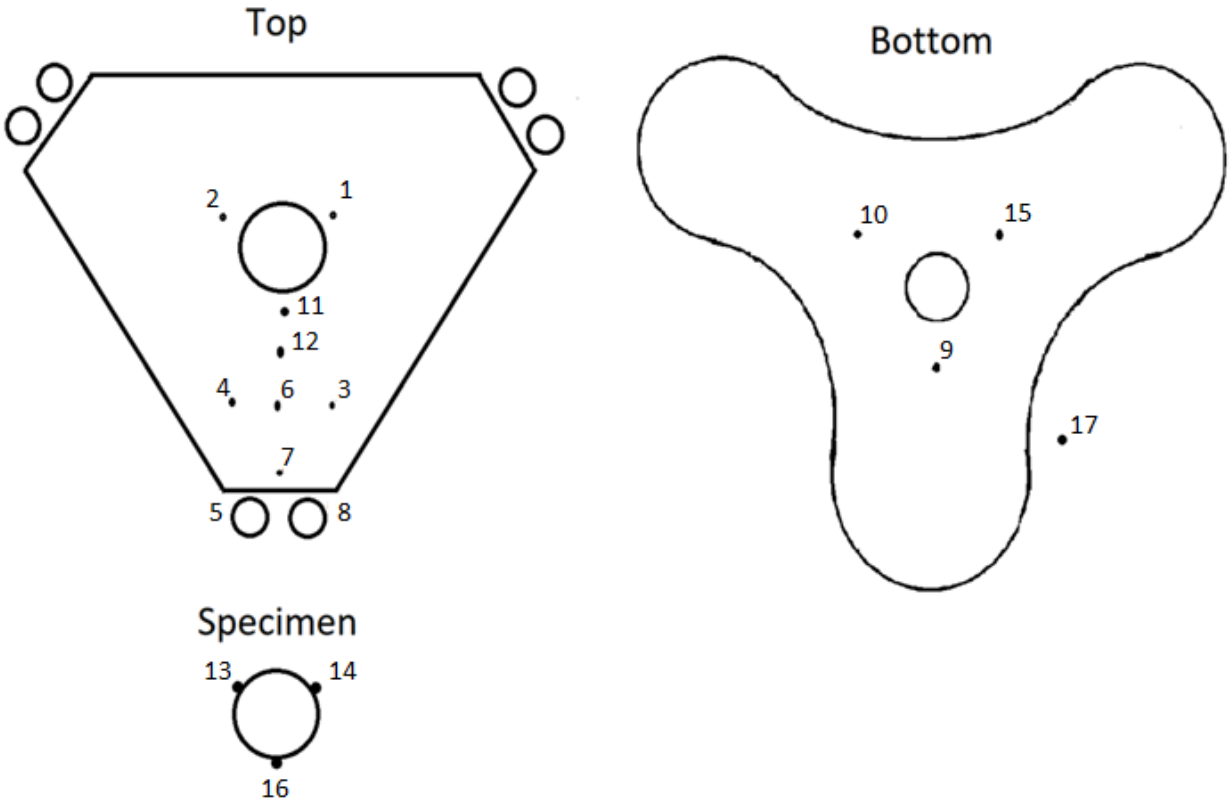

Figure 30 Sensor positioning of the characterization test

Load cases of characterization of the noise test

The test used different movements of the Hexapod to determine the background noise. First, the x-, y-, z-axes were tested on a load of 200 kN with a frequency of 10 Hz. The rotations of all these axes were tested on a load of 25 kN and a frequency of 5 Hz. At the end, a MOSA test (Multiaxial Online Signal Adaption) was conducted; in it, the machine moved in a random manner, with a force of 15 kN and a frequency of 5 Hz. These load tests were performed with a maximum duration of 10 minutes.

Results

The primary goals of the characterization test was to determine what kind of noise was arriving at the specimen and to specify its origin. During all of the different load cases, the signals on the specimen had a minimum duration of 500 microseconds (see appendix A). The sensors with the shortest signal duration and the highest amplitude were found at the top hinges of the Hexapod (sensors 5 and 8).

Conclusion

The background noise that the Hexapod produced did not resemble fatigue signals. The background noise was easily filtered out by the guard sensors and by cutting signals longer than 500 microseconds. The experiments with samples with fatigue did not have to adjust to or compensate for the background noise of the Hexapod during short-term testing.

3.3. Experiments

In this subsection, all of the tests with AE sensors on the tubular welded specimen are explained, and an RMS analysis is conducted.

3.3.1. The test procedure

For accurate installation of the sensors at the predetermined locations, two molds were made from rubber (see Figure 31 and Figure 32). These molds were cut with a laser and provided a positioning accuracy of 0.2 mm.

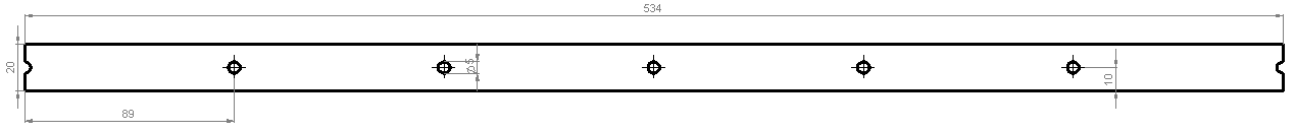

Figure 31 Specific mold 1 technical drawing

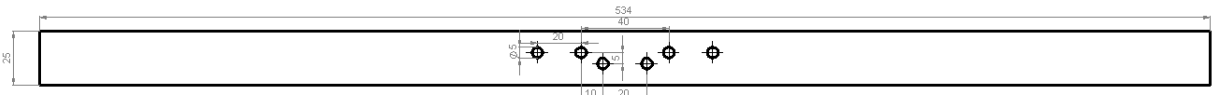

Figure 32 Specific mold 2 technical drawing

The first mold (Figure 31) was made to ensure that the sensors were positioned equally around the specimen. In the mold, the sensor was 10 mm above the weld and 89 mm from the adjacent sensors (see Figure 33). The second mold (Figure 32) was made for monitoring a crack with an expected location. As seen in Figure 34, the sensors were put around the probable location of the crack. They were spread only in the x-direction. Spreading the sensors in the y-direction was not possible because of the strain gauges that were located near the possible crack initiation.

Figure 33 Installation of sensors with mold 1

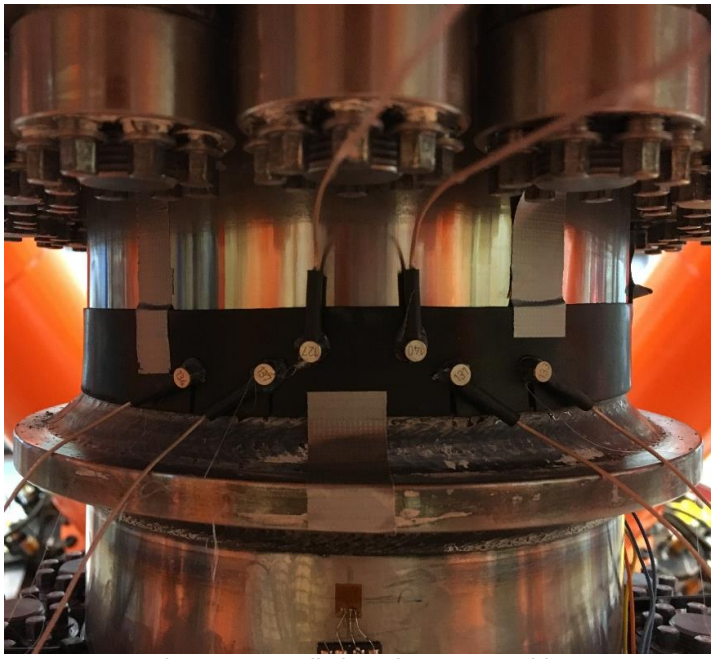

Figure 34 Installation of sensors mold 2

After the sensors were positioned, the mold could be removed. Before the system could be used, a test was needed to confirm that all of the sensors worked correctly. The pencil lead break (PLB) test was used to calibrate the sensors. A PLB test generates a Hsu-Nielsen source, which is a simulated AE source in accordance with ASTM-E976. A PLB test is conducted by breaking a pencil's lead with a guiding ring. Usually, the pencil lead has a diameter of 0.35 mm or 0.5 mm and a 2H hardness (see Figure 35). In this study, the PLB test was repeated for a minimum of 10 times per sensor for consistent comparison.

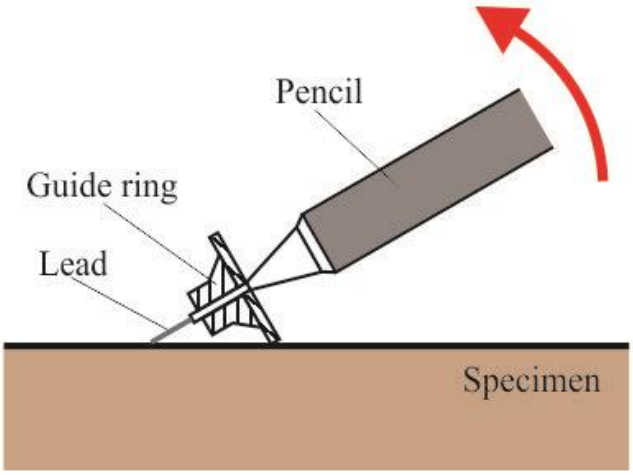

Figure 35 Illustration of a Hsu-Nielson source application (ZfP-Wiki, 2018)

3.3.2. Tension and bending experiments

In this study, three experiments were performed with entirely different configurations of the AE sensors. There were two tension tests with similar loads, with one having sensors only on one side of the weld (10 AE sensors; see Figure 1) and the other having sensors on two sides of the weld (16 AE sensors). The bending test had 11 sensors on one side of the weld. The selection of the data coming from the experiment for further processing will be done in this chapter. For a technical drawing of the specimen see Appendix C.

The first tension test

In the setup for the test, six sensors were placed above the weld, with a spacing of 89 mm between the adjacent sensors. All of the sensors were 10 mm above the weld (see Figure 36). In addition to these sensors, four other sensors (two sensors on the top and two at the bottom) were for picking up signals that could come from outside the specimen. For this test, there was no room to put the sensors under the weld because of the strain gauges that were situated on the specimen, as shown in Figure 36 and Figure 37. In this test, the load was applied in the Z-direction (tension) with a stress range of 175 MPa and a frequency range between 5 Hz and 7 Hz .

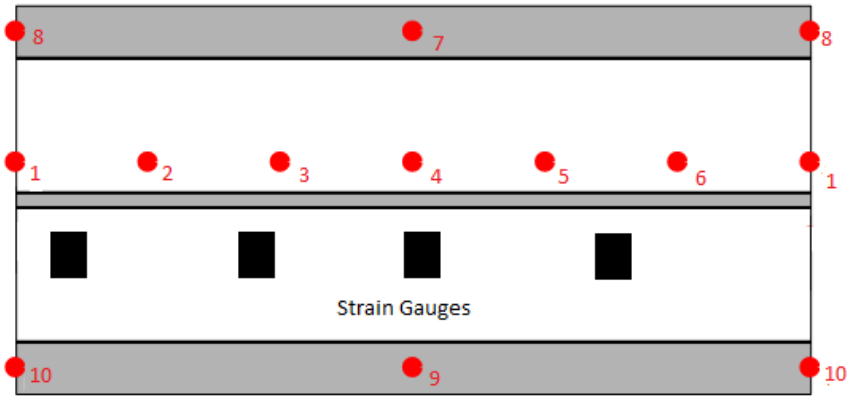

Figure 36 Flat pattern of sensor positioning with strain gauges

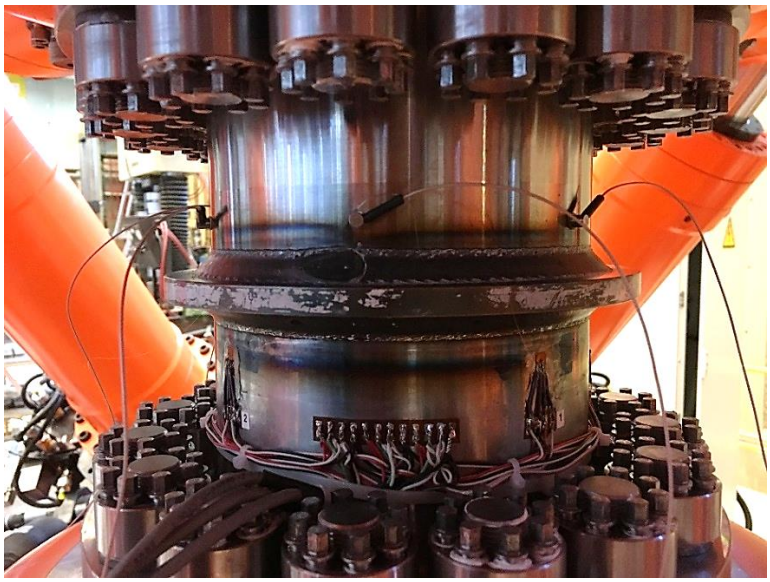

Figure 37 Specimen with the sample under tension

After 5.2 million cycles, the sample showed fatigue damage, with the crack almost breaking the sample into two pieces (see Figure 38). The crack started under the start-stop of the weld, which was the weakest point of the weld.

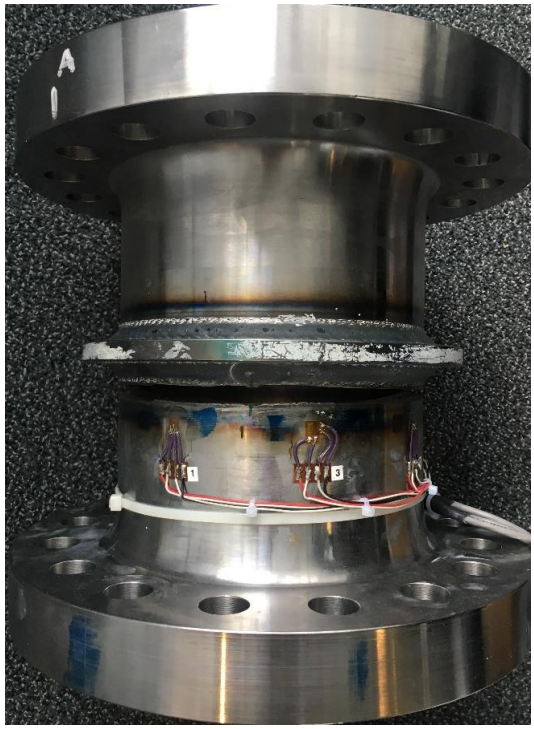

Figure 38 First tension-test specimen with a crack

Results

The crack formed on the other side of the weld. Therefore, the data of this tension test was not used in the results section. The test revealed that there was a settling time of the specimen or the machine or both. The settling time was the period that the specimen needed to not produce an elevated background noise. This could be seen with the RMS values of the test (see Figure 39) for the first part of 50,000 seconds (about 14 hours). This had an elevated RMS value, so this first part of the test was referred to as the settling time. The problem in this time period was that the background noise was too high. Therefore, the threshold was set higher than the signals produced by the specimen. In essence, this means that no useful information was recorded during the settling time.

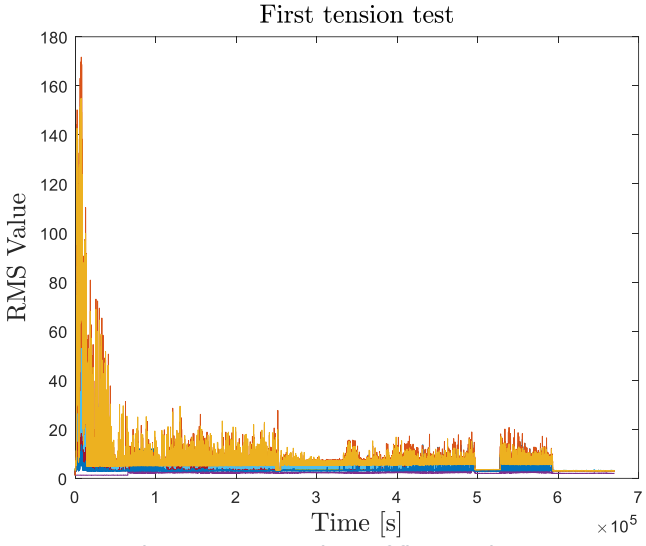

Figure 39 RMS values of first tension test

The Second Tension test

The second tension test was essentially the same as the first one; however, this time there were no strain gauges were placed on the specimen. Therefore, there was space for six extra sensors, which brought the total for this test to 16. The load was applied in the Z-direction, with a stress range of 175 Mpa. Twelve sensors were placed around the weld and four on the edges of the specimen (see Figure 40 and Figure 41).

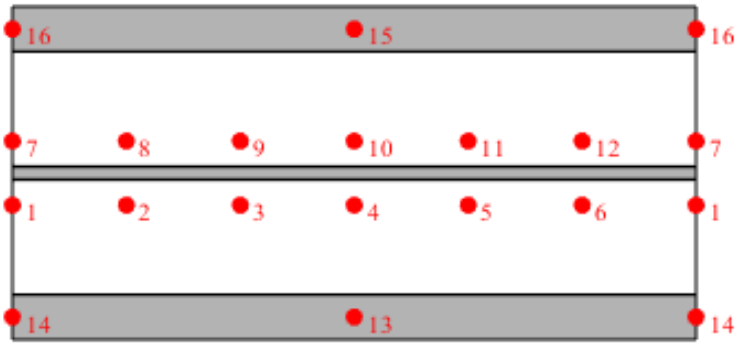

Figure 40 Flat pattern of sensor positioning for second test

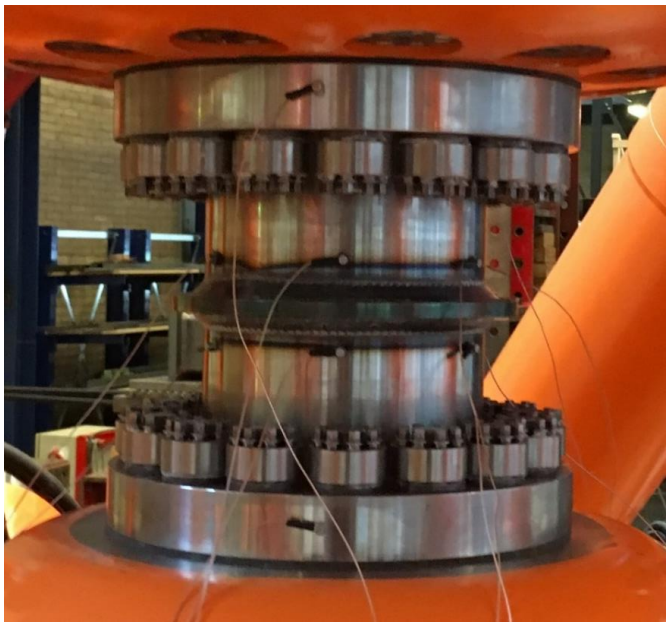

Figure 41 Specimen with 16 sensors for the tension test

After 10.4 million cycles, the test was stopped because the crack had become visible (see Figure 42), and the Hexapod started to reposition the traverse.

Results

The second tension test was split into two parts. The first part went from the start to 8.5 million cycles and then from 8.5 million to the end of the test. Between these parts, the test was halted for a week. The settling period was $5.35 * 10^4 s$ (almost 15 hours), or 0.375 million cycles, as can be seen in Figure 43. In the second part, there was no settling time of the specimen (see Figure 44). The RMS absolute max was reached only at the beginning of the test; moreover, an RMS value higher than 100 was not reached by the end of the test. For the second part, the hits passed the threshold only at the very end of the fatigue test. The full analysis of the second tension test is performed in the next chapter.

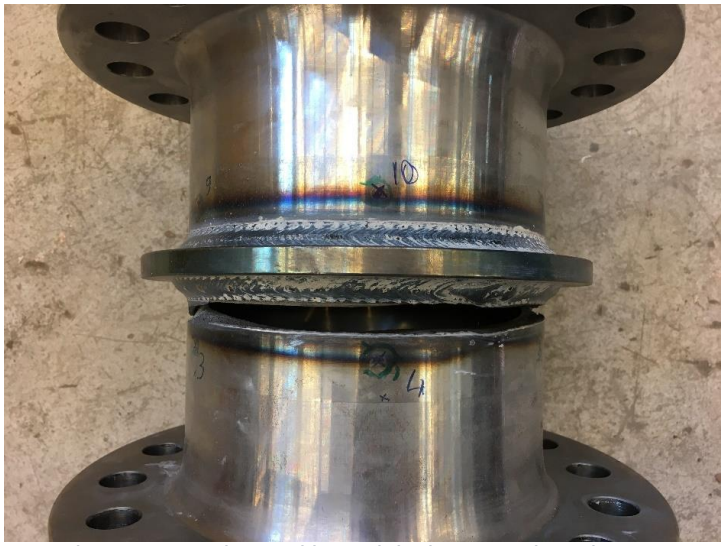

Figure 42 Specimen with crack in the second tension test

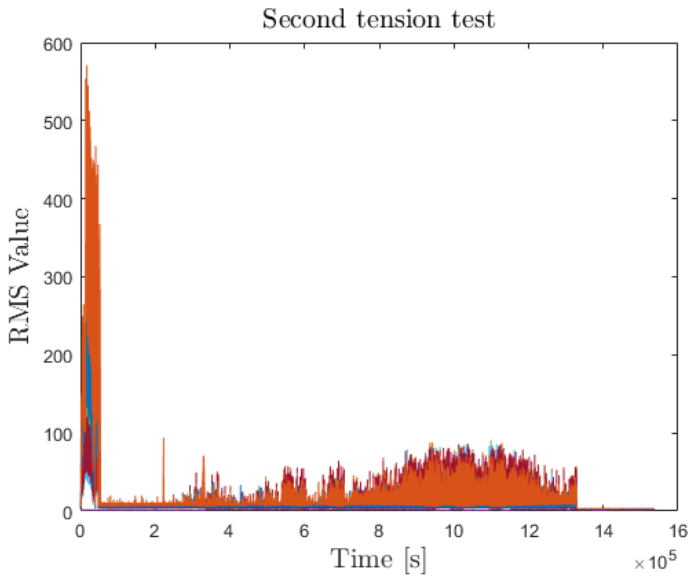

Figure 43 Second tension test RMS from 0 to 8.5 million cycles

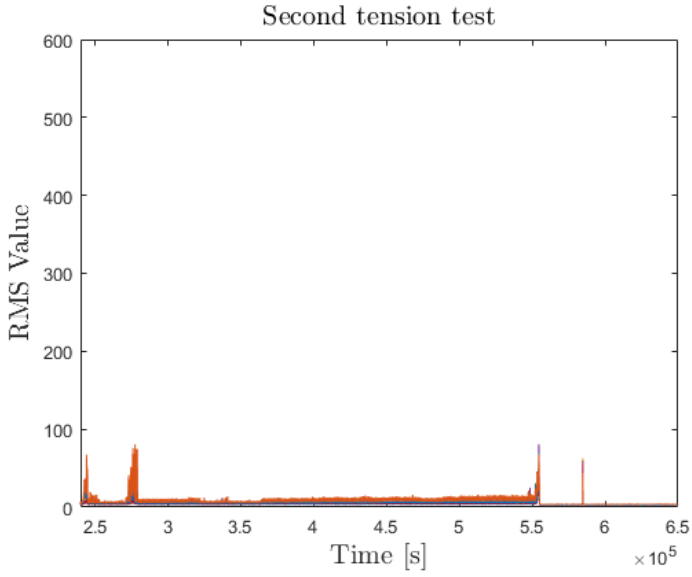

Figure 44 Second tension test RMS from 8.5 to 10.5 million cycles

Bending test

The bending test is one that involves rotation around the x-axis. In addition, strain gauges were placed on the specimen in this test, similar to the first tension test. Before testing, the exact location of the future crack is known, this is because the maximum stress line is known in bending. Therefore, the configuration of mold 2 was used (see Figure 34). This geometry of sensor placement provided a more accurate localization of the signal (see Figure 45). The offset of two sensors (sensors 3 and 4) made it possible to calculate with more depth.

Results

The specimen failed within the first 8 hours of the test with a stress range of 320 MPa and 74.777 cycles, this is during the settling time (for the RMS value, see Figure 46). This means that there were no signals recorded in the entirety of the experiment, so these tests are not considered in the next chapter.

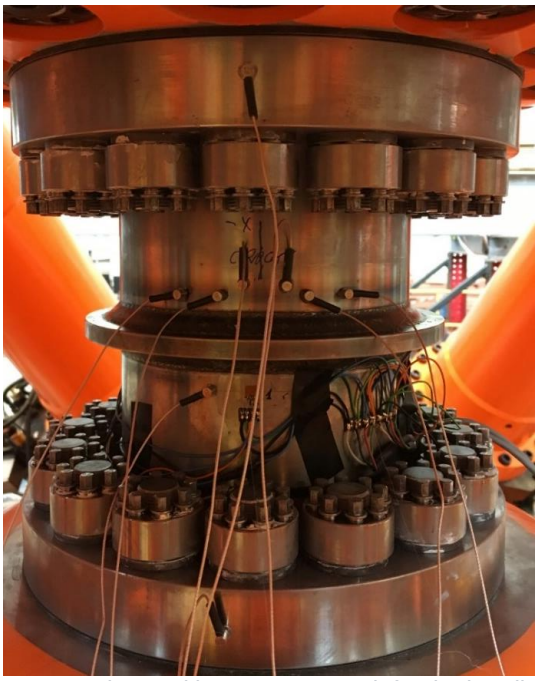

Figure 45 Specimen with 11 sensors on it for the bending test

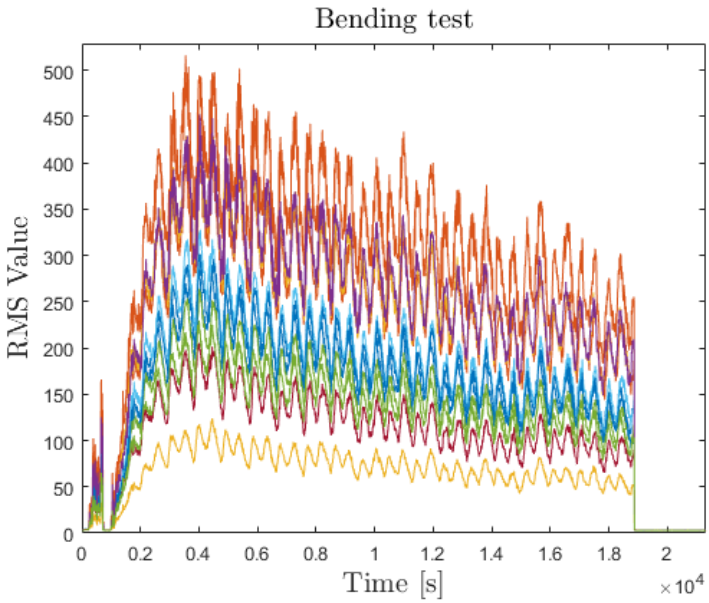

Figure 46 RMS value of the bending test

3.4. Conclusion

A noise characterization test was performed on a Hexapod, and the results provided the foundation for the analysis of the fatigue experiments (covered in the next chapter). The characterization experiments revealed a settling time in the beginning of the experiments, and this effect was conveyed by the RMS values. The settling time was a problem for the short-duration experiments, because the AEs could not be distinguished from the background noise during tests shorter than 14 hours. In regard to the longer tests, the first 14 hours of the data acquisition were discarded.

Because the sensors in the first tension test had not been placed on the side of the weld where the crack developed, the related data is not analyzed in the next chapter. The bending test was shorter than the settling time; thus, it did not produce any useful data to be analyzed. The only test that is analyzed in the next chapter is the second tension test, because its sufficient duration allowed a reasonable amount of AE activity to be detected after the settling time, with the AE sensors placed near the origin of the crack.

4. Results and analysis

In this chapter, the test results are analyzed and presented. The considered dataset was acquired during a tension test with AE sensors on both sides of the weld.

Before the analysis of the test is provided, some background information for the analysis is provided. The assessment of the data consists of the whole dataset and later sections of the dataset will be analyzed in more detail. Both times being analysis in a global sense and only the sections having a localization calculation. First, the entire dataset is analyzed, and the data are analyzed in a parametric study but on a global scale. A local analysis in a global context is not done here, because there were millions of signals acquired and processing them would require too much time. This was one of the reasons why the data were reduced to section of a certain length.

The intention behind using sections was to process the data in different periods of the fatigue lifetime. The multiple sections can be compared throughout the fatigue lifetime. The sections had a specific length of time (600 seconds), and all segments were of equal duration. The time between the sections was about 50,000 seconds when possible. For every segment, the average amplitude and the hit rate per cycle were calculated in the global analysis.

The local analysis was focused on estimating the source positions of a certain number of arbitrarily selected events for each segment. These source positions were used to track the progression of the initiation and growth of the fatigue crack. The structure and details of the analysis are discussed next.

4.1. Structure of the data analysis

The approach for the data analysis is visually represented in the diagram in Figure 47. The analysis began with recording the AE signals on the specimen. A global parametric analysis is conducted on the full dataset—in particular, a parametric study of all the hits. In specific the duration of the signals, to identify possible fatigue signals. Data from the characterization of the noise could be compared with what happened during testing, with and without fatigue (section 3.2). For a more detailed analysis, the full dataset was divided into 24 sections, each with a duration of about 600 seconds. The first 22 segments were samples taken about 50,000 seconds apart from one another. The last two segments were samples taken close to the fracture. With these 24 segments, another parametric study was conducted on the average amplitude and hits per cycle. In addition, the locations of the source events were estimated in a local analysis. To obtain accurate estimations of the time differences of the arrival scheme employed in this analysis, the times of arrival of the signals needed to be determined. In addition to the local and global analyses, a fatigue analysis with the British standards was conducted. All of these aspects of the analyses are analyzed after the postprocessing conclusions are made with all of the information obtained during the total analysis.

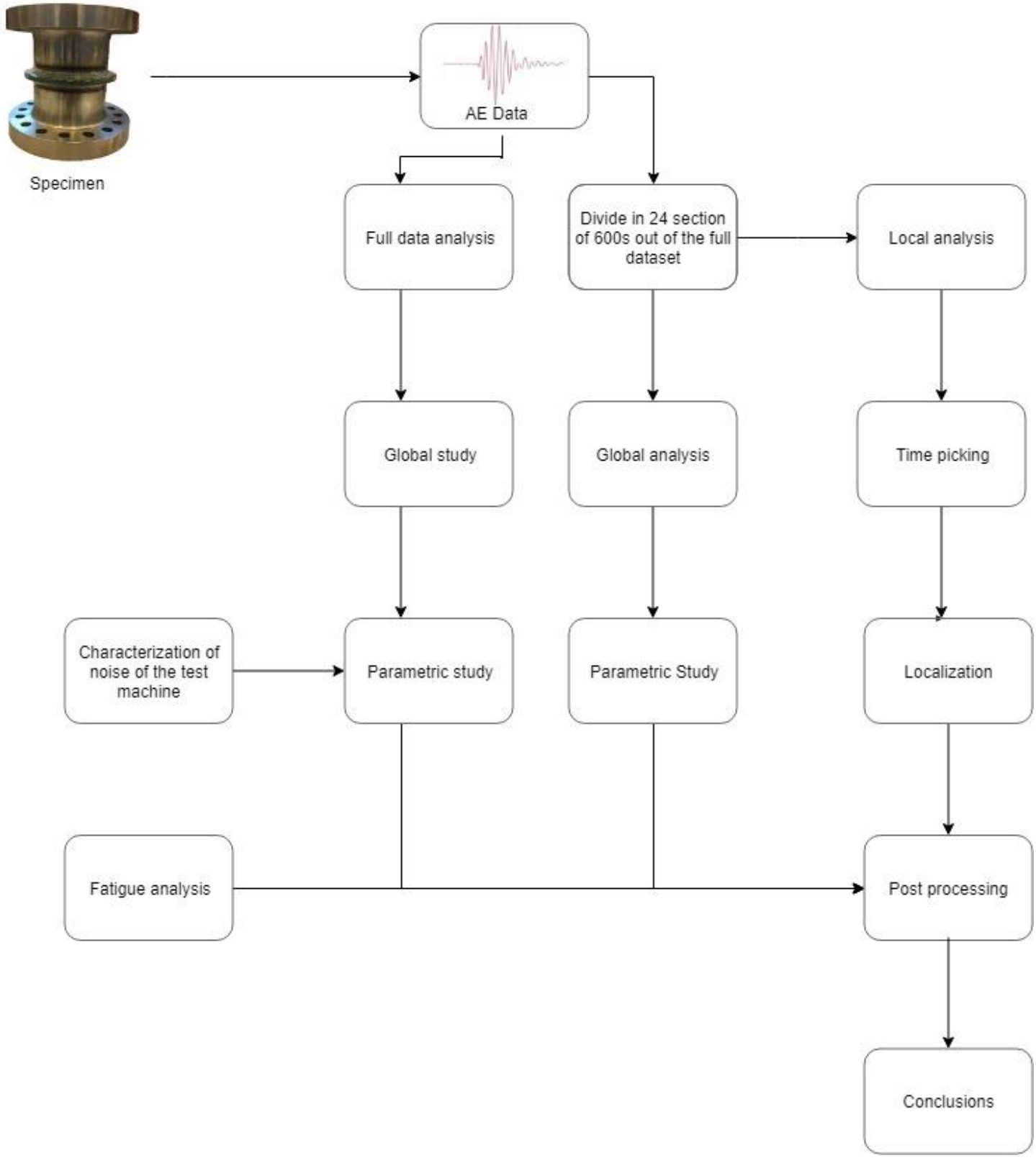

Figure 47 Diagram of the analysis structure

4.2. Parametric study of the entire data set

In this chapter, the global parametric study on the test (see 3.3) is presented and compared with the noise characterization test (see 3.2).

Duration of the signal

The duration can reveal nearby signals that possibly contain fatigue signals. Because fatigue can heard only when the fatigue crack grows, which produces a stress wave. These stress waves are short bursts, and the further they move, the longer they become because of dispersion. If there is fatigue, the signals do not have a duration longer than 500 microseconds. Looking at the duration of the signal is the first step of the data analysis. According to the noise characterization test, hardly any signals were shorter than 500 microseconds (see appendix A). Noise characterization tests were performed with a machined nonnotched specimen. As such, the accumulation of fatigue damage was unlikely to occur during this test.

For the comparison between the test without fatigue and with fatigue, the sensors on the specimen were compared because these were the only sensors that were in the same position in both tests. For the characterization test, sensors 13 and 14 were chosen (for position see Figure 30). The sensors used for comparing the second tension test, sensors 5 and 7 are used. The results of the noise characterization test for the duration on the tubular with no weld are shown in Figure 48. The graphs show that there were no signals with durations shorter than 500 microseconds and barely any signals with durations between 500 and 1000 microseconds. In the second tension test, 16 sensors were placed on the specimen (see Figure 40); in the noise characterization test, only 3 were used. Therefore, the choice was made to compare the sensors that were closest to the location of the crack initiation (sensor 5 in Figure 40). Sensor 7 was chosen because it was the sensor farthest away from the crack initiation but was still next to the weld and was not on the edges of the specimen. When the signals of

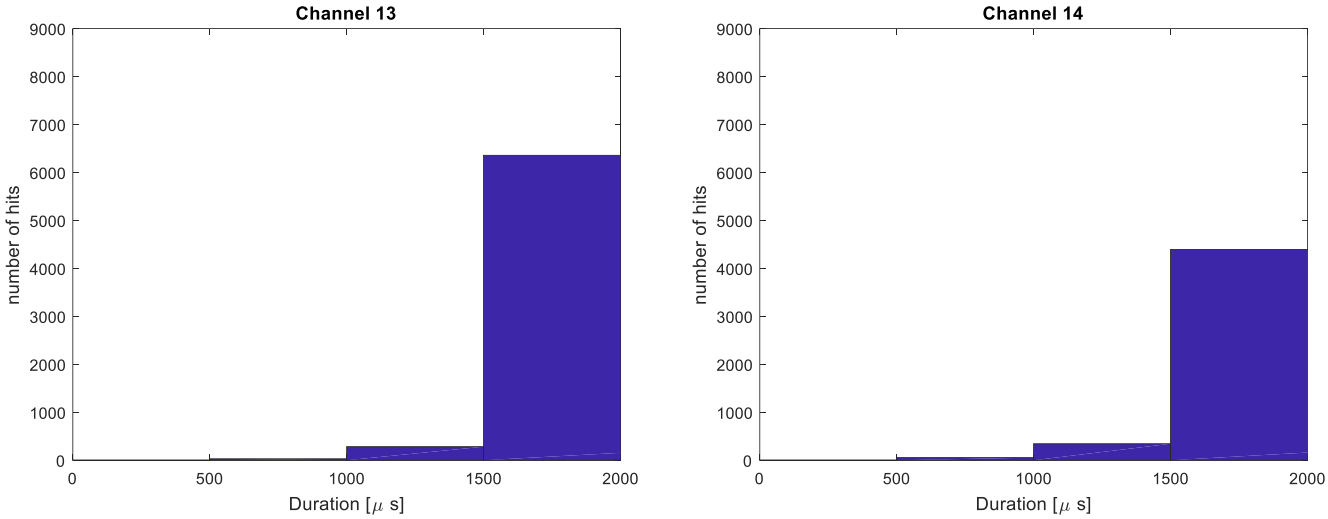

Figure 48 Bar chart of the signal duration of the sensors on the specimen during the characterization test

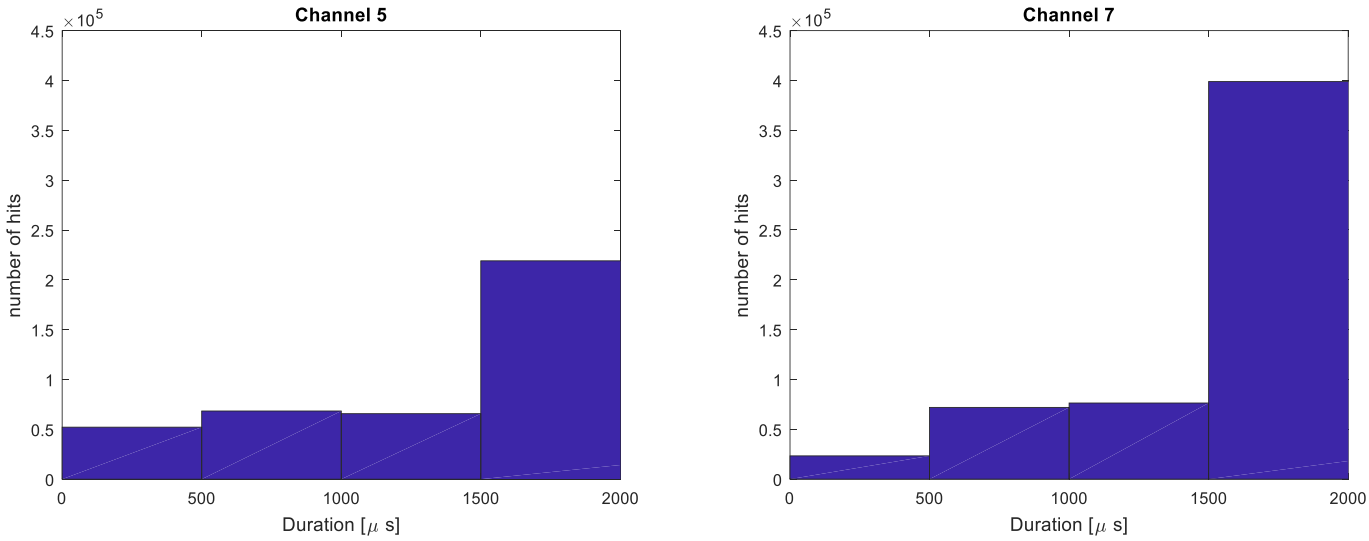

Figure 49 Bar chart of the signal duration of the sensors on the specimen during the second tension test

the second tension test are compared, it can be seen that there were numerous signals with durations shorter than 500 microseconds (see Figure 49).

Conclusion

The goal of comparing the signal durations was to determine whether there was a significant difference between the AE signals for specimens with or without fatigue. According to the data, there was a significant difference. There were no signals shorter than 500 microsecond (see Figure 48). The signals of the specimen with a fatigue crack (see Figure 49) had a significant amount of signals that were shorter than 1000 microseconds. Therefore, two conclusions can be drawn: Fatigue was present in the second tension test, and the testing machine did not produce signals that mimicked fatigue signals.

4.3. Parametric Study of Individual Sections

In this section, the parametric study on the global and local analysis of the 600-second sections are explained and analyzed.

As previously mentioned, a global analysis and a local analysis are performed in section 4.5, and the full dataset was analyzed in 4.2. From that data, 24 sections that were 600 seconds long were obtained. The first 22 sections, which contained AE data recorded between 1.75 million and 8.5 million cycles, were separated by intervals of 50,000 seconds. The testing halted after section 22 and restarted a week later. After the test recommenced, the threshold was crossed only at the end of the experiment. Therefore, the last two sections, recorded between 10.31 and 10.34 million load cycles, were taken at the end of the fatigue lifetime, as shown in Figure 56, and thus during the fracture phase.

During the second tension test, the Hexapod did not apply a constant loading frequency; thus, the 600-second sections did not comprise same number of cycles. The frequency change, in theory, did not noticeably affect fatigue lifetime if the cycles are considered and not the time. In general, fatigue is expressed in cycles under a constant stress; therefore, conversion from the time to cycles is the only good representation of the data.

For the conversion, the frequencies during the experiment must be known. The frequencies of the experiment are shown in Figure 50. The frequencies and time were removed from the equation by multiplying them with each other. The multiplication provided the total number of cycles. Thus, the different sections at different frequencies became comparable because the fatigue growth then was conveyed by the number of cycles and the magnitude of the stress.

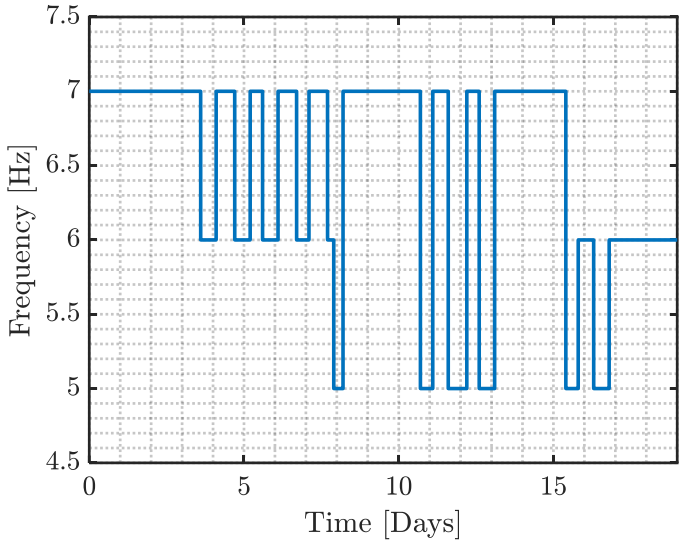

Figure 50 Graph of frequency change of second tension test

4.3.1. Maximum Displacement

Over the course of the test, the oscillating displacement of the Hexapod changed because of the plastic deformation of the specimen. In Figure 51, the maximum displacement of each cycle is shown for the whole test. There is a discontinuity in the graph because at 8.8 million cycles, the machine stopped and the reference changed. For comparison with the other parameters, the maximum displacement of each section was taken, as shown in Figure 52.

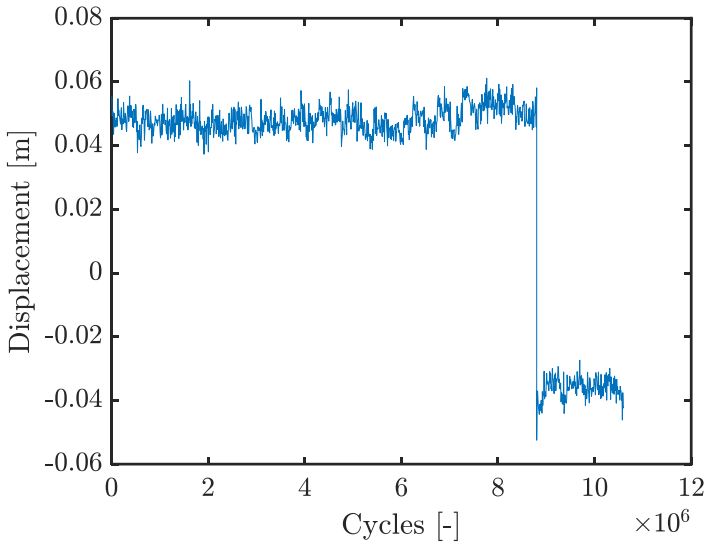

Figure 51 All of the data points of the maximum displacement

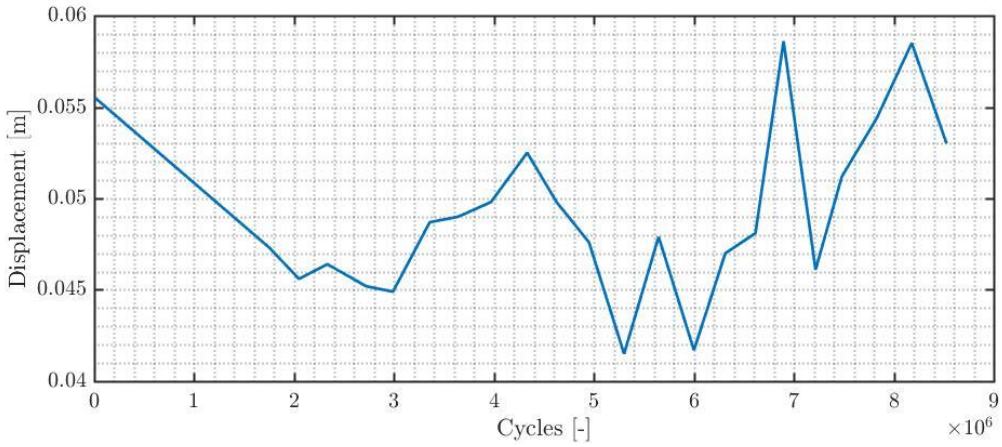

Figure 52 The maximum displacement of each section

4.3.2. Average amplitude per section

The average amplitudes for each individual channel was calculated in decibels (dB) for every 600-second section. The following three graphs provide a better view of the amplitudes in the different locations (see Figure 53, Figure 54, and Figure 55). Figure 53 shows the amplitudes of the sensors around the initiation of the crack, so the sensors 3,5 and 9-11 (for locations of sensors see Figure 40). Figure 54 shows the amplitudes of the sensors that were not around the initiation of the crack and not on the edges. Figure 55 shows the amplitudes of the sensors on the edges of the specimen.

As conveyed by the graphs, the average amplitudes in all three groups increased to 89.5 dB at 6.3 million cycles and then slowly declined until the fracturing occurred. Only for channel 16 did the amplitude increase again after the drop and as the end of the test approached. Near sensor 16, there was a source that elevated the amplitude of all the adjacent channels. This elevation occurred in channels 7 and 12, which were the closest to channel 16 (see Figure 40). Channel 13 was the farthest away and had the lowest average amplitude of all the sensors (see Figure 55).

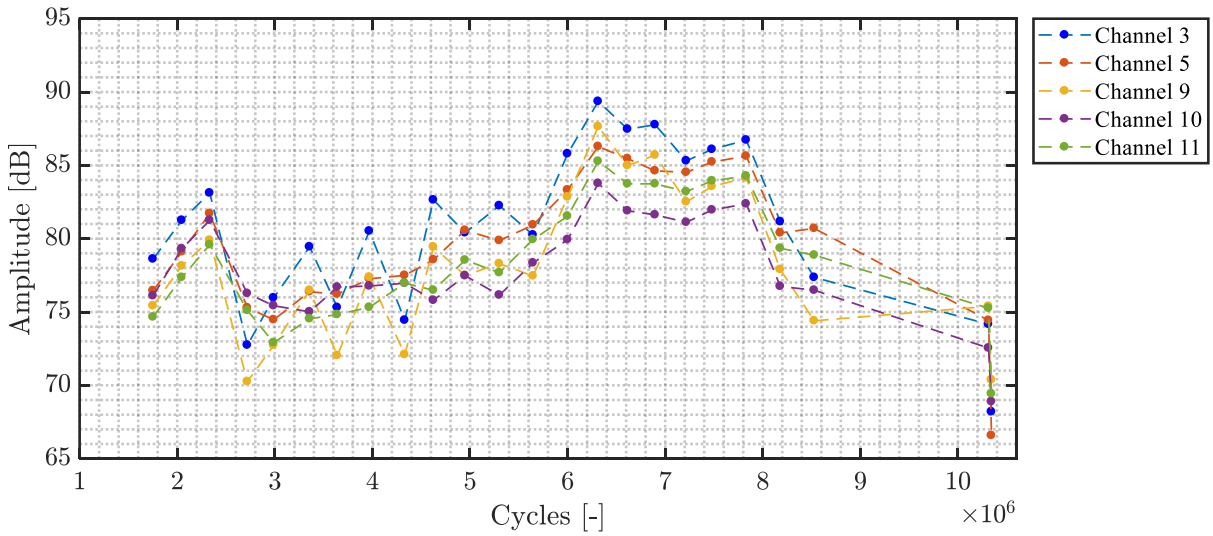

Figure 53 Average amplitude of sensors around the initiation of the crack

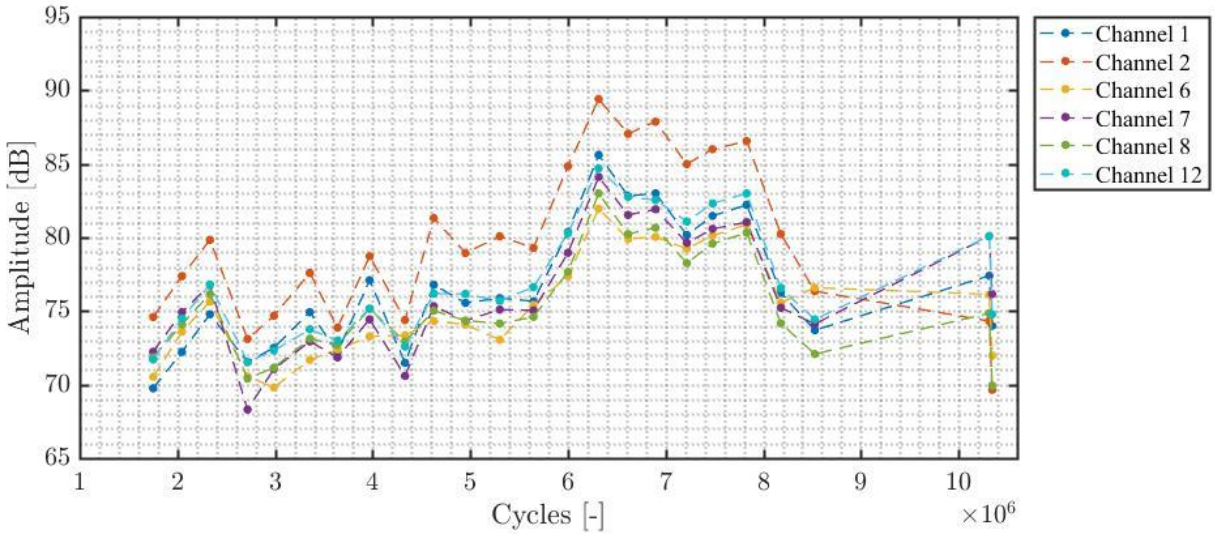

Figure 54 Average amplitude of sensors not around the initiation of the crack

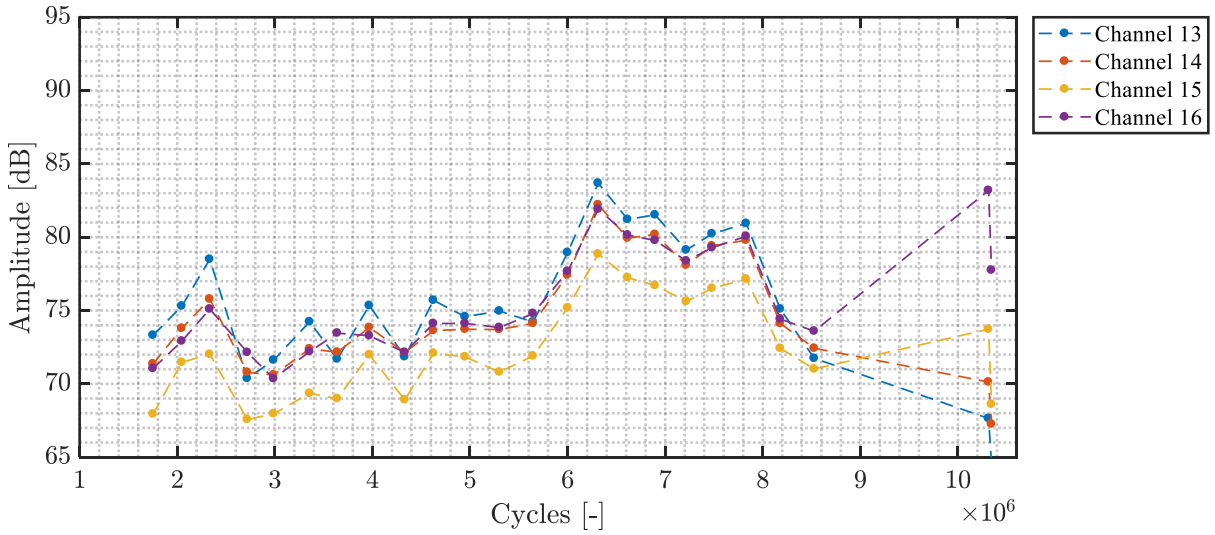

Figure 55 Average amplitude of sensors that are on the edges of the specimen

4.3.3. Hits rate per cycle per section

In general, the hit rate is a good measurement of activity. In the test, a higher number of hits per cycle signified a higher amount of fatigue in the vicinity of the sensors. If the growth of a fatigue crack growth is very active, the hit rate per cycle should go up. In this paper, not all of the channels are shown, because their trends were similar to those of the sensors that are shown. The channels that were chosen were channel 5 and channel 7(for all channel see Appendix D), for the same reason as before (see 4.2.). However, because channel 16 recorded high activity at the end of the experiment, it is considered for this evaluation of the hit rate per cycle. The following graphs display trends similar to those in the average-amplitude graphs (see Figure 53, Figure 54, and Figure 55). There was a peak in the first part (from 0 to 8.8 million cycles) at 6.3 million cycles, but the second part (from 8.8 to 10.6 million cycles) showed a higher peak. Though the first peak occurred around 0.2 hits per cycle and the second peak around 0.35 hits per cycle for channel 5, this trend was observed in all channels. However, channel 16 provided unique results: There were similarities in the first part, but the second part was significantly different. The starting point was nearly the same but lower in general; this was because Sensor 16 was initially far away from the source. In the second part, channel 16 had the highest hit rate per cycle, the second highest occurred in channel 7, and the lowest occurred in channel 5. This means that the source was in the vicinity of sensor 16.

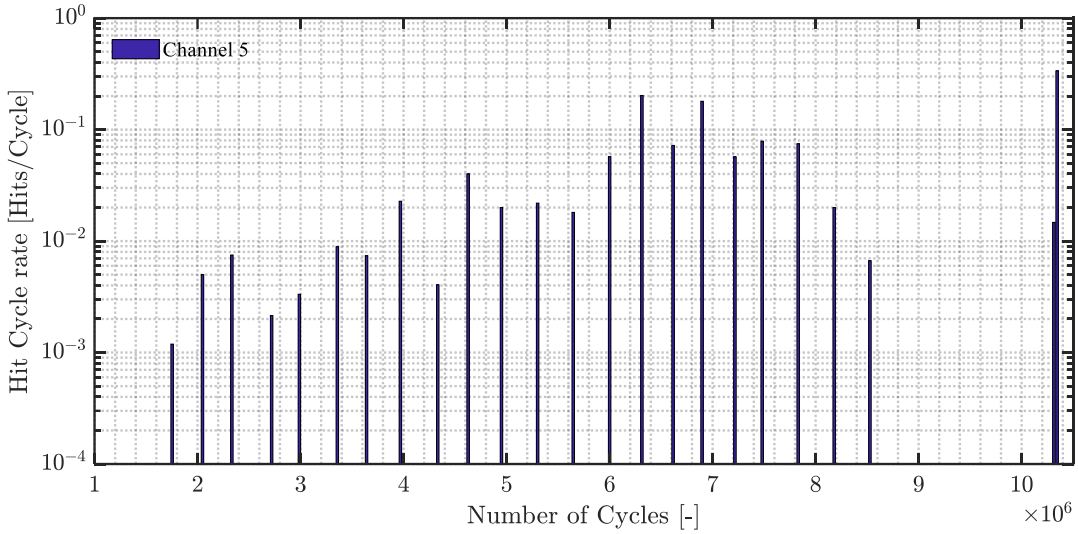

Figure 56 Sensor 5 hits per cycle over time for the different sections

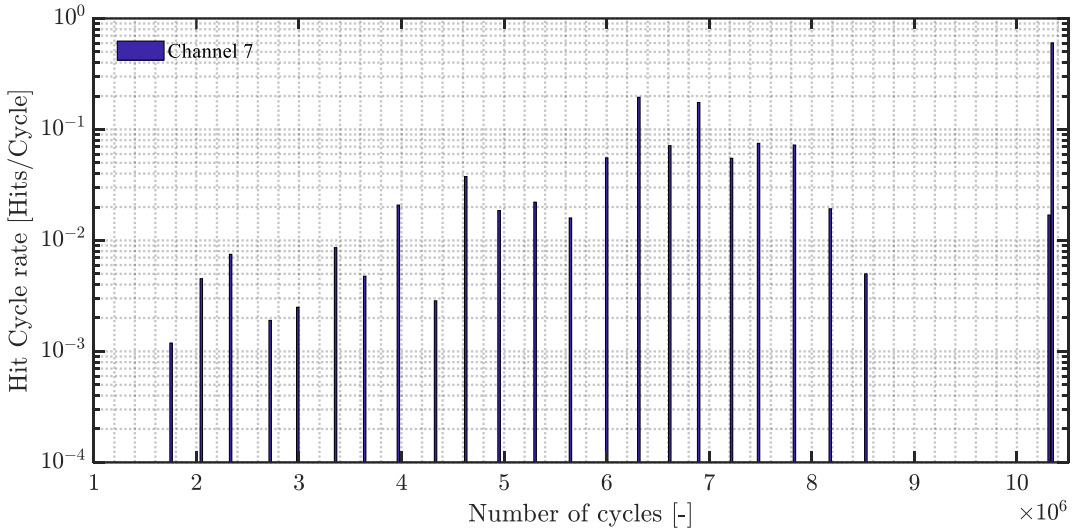

Figure 57 Sensor 7 hits per cycle over time for the different parts

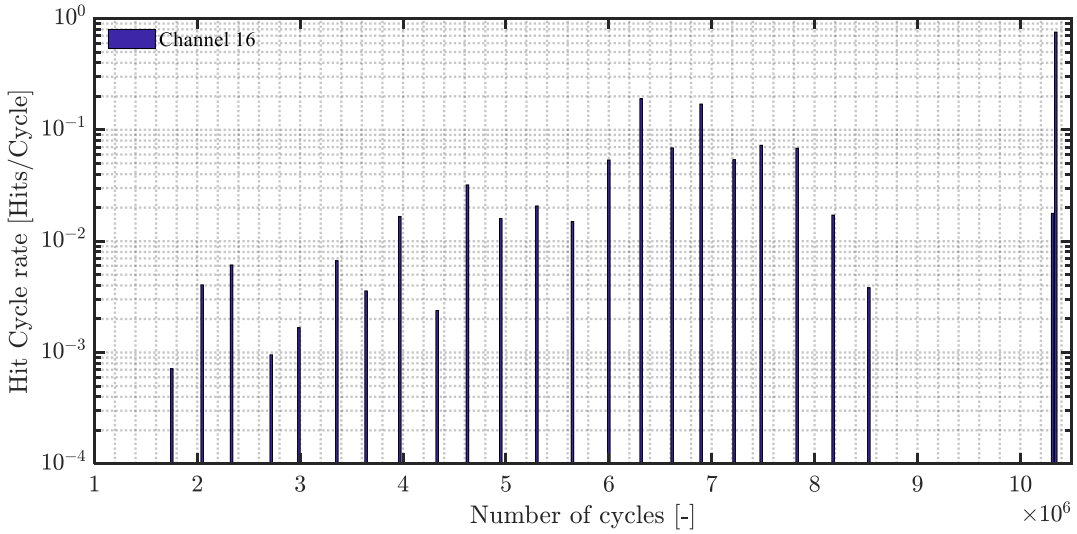

Figure 58 Sensor 16 hit per cycle over time for the different Sections

4.3.4. Discussion

When the average amplitude was compared with the hit cycle rate, there was a similarity between 0 and 8.8 million cycles. Both had the same shape, and the peaks occurred at the same point (6.3 million cycles).

From 8.8 to 10.6 million cycles, the hit rates per cycle were significantly different, in the sense that the average amplitude and hit rate per cycle showed an inverse trend. Where the average amplitude decreased to a minimum, the hits per cycle increased to a maximum. This was the case for the channels that were not close to channel 16.

Channel 16 caused significant increases in the average amplitude and the hits per cycle. There are two possible reasons for this:

- Changes occurred in the mounting of the specimen in the Hexapod during the time the test was halted, leading to friction in the bolts used for mounting.
- Changes occurred in the orientation of the traverse, leading to a different loading and friction in the bolts used for mounting.

When only the first 8.8 million cycles are considered, the activity reduction from 6.3 to 8.5 million cycles is striking. This was not expected; in the fatigue lifetime, the activity should increase because the crack should be growing faster since more stress is traveling through a smaller surface. A possible explanation is that the fatigue crack was propagating through the specimen, meaning the crack front was becoming larger. When the crack had grown to through-thickness, the limit of the crack front size was reached. This was where the activity was expected to be at its maximum. This could not be visibly confirmed because accessibility to the specimen was limited during testing. When the crack continued to grow, the crack front decreased in size, leading the crack front line to decrease to the thickness of the specimen.

A second explanation is that there were multiple nucleations in the initiation phase. At the peak, one crack becomes governing during the crack growth phase and therefore the activity declines.

4.3.5. Conclusion

The average amplitude and hits per cycle showed similar activity in the first part. In the second part, only channel 16 detected fatigue signals coming from the crack. This should be investigated further.

4.4. Fatigue Calculation

In the previous chapter, the theory of how the peak of the graphs at 6.3 million cycles in regards to crack growth. Is this point the point where the crack is through and through, therefore a fatigue calculation is done to see in what range the crack hits the through and though point.

The British standards for fatigue guidelines (BS 7910-2013) were used to calculate the stable crack growth in the specimen, and the values $m = 3$ and a $C = 3 * 10^{-13}$ were used. The loading of the experiment was 175 MPa with an estimated initial crack of 0.01 mm. The stable crack growth in the specimen, calculated with the British standards, had an approximate duration of 1.5 million cycles for an elliptical crack front (see Figure 13). The shape of the stable crack was confirmed on the specimen via a postinspection (see Figure 59).

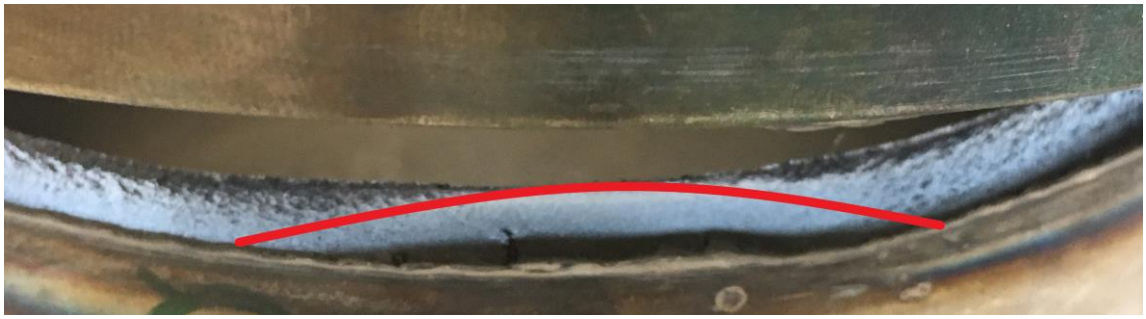

Figure 59 Picture of stable crack front growth

4.5. Localization of the AE sources

The localization of AE sources was an essential insight for this research because the sources were assumed to be coinciding with the crack front. The goal was to monitor the crack propagation by means of tracing the source locations of the AE signals during fatigue testing. The results are shown in this section.

4.5.1. Results

Localization was done for each event that was composed of multiple hits. For the calculation of the source position, the time picking per hit was essential for the accurate localization. The sensors that were used for the localization were 1–3, 5, and 6 (see Figure 60). Sensor 4 malfunctioned and thus did not record the stress waves in the same manner as the other sensors or even a signal at all.

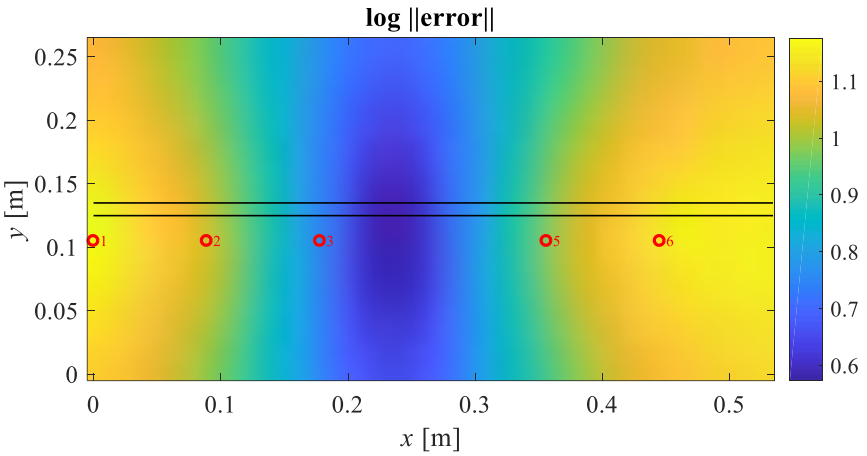

Figure 60 Localization graph of a single hit

Every event with more than two hits had an uncertainty contour, as shown in Figure 60. For the local analysis, five events of every section until section 22 where randomly selected with a random function. Section 23 and 24 were not addressed in this analysis because the source came from the edges and not from the crack. The uncertainty contours of these sections were not in the theoretical space and thus not that useful (see Figure 61).

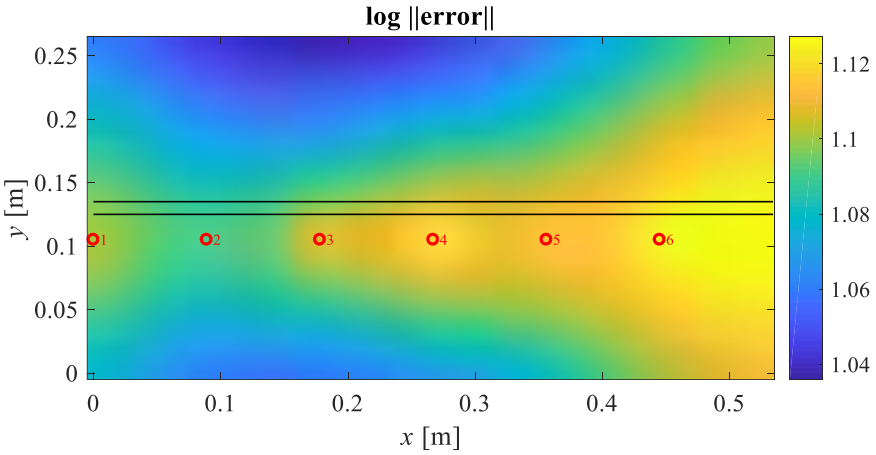

Figure 61 Localization graph of section 23

The calculation of the location gave a single point for every event that was analyzed. There were five location points per section, so there were 110 location points in total. In Figure 62, the locations are ordered per set of million cycles, starting with the interval of 1 million cycles and then proceeding to 2 million cycles and ending on 8–9 million cycles. In Figure 63, the detected length is illustrated in the same interval definition used in Figure 62. The crack growth can be clearly seen in the two figures. The actual size of the mode 1 crack was 250 mm after failure. The detected crack was 230 mm long. In addition, there seemed to be a hole in the middle, where no sources were calculated. The final crack had a length of 280mm with mode one length and potential further cracking during the opening of the crack. Therefore only 250 length that was visual before opening is considered here.

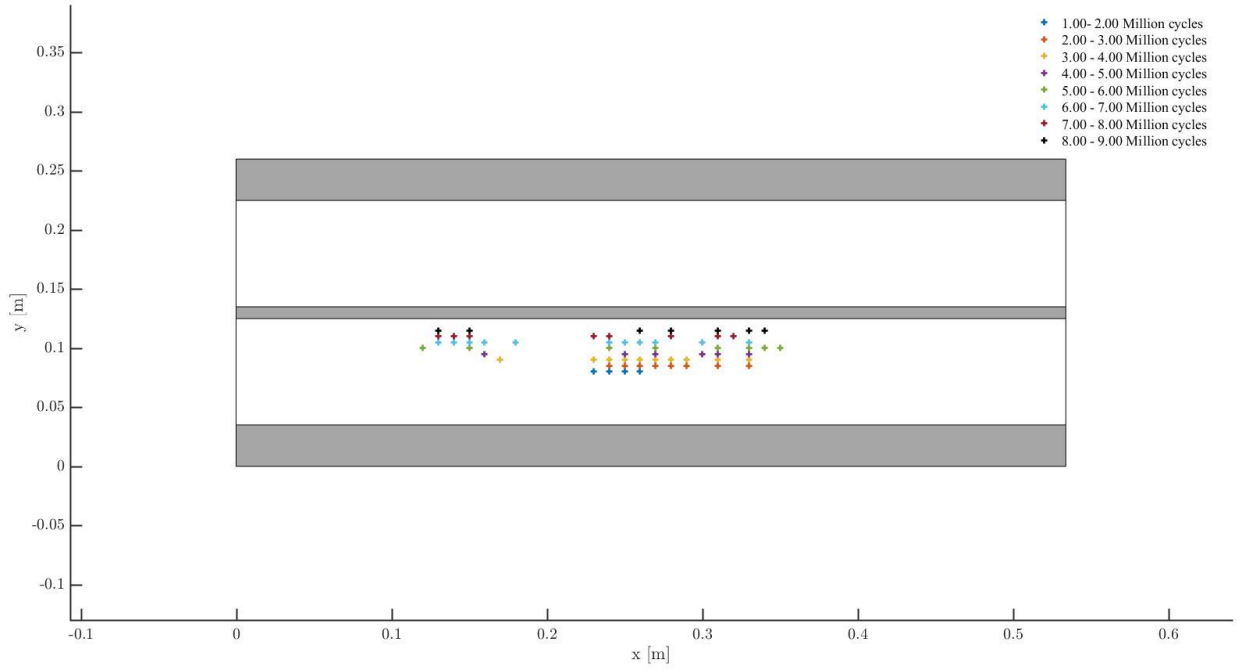

Figure 62 Locations of all the analyzed sources

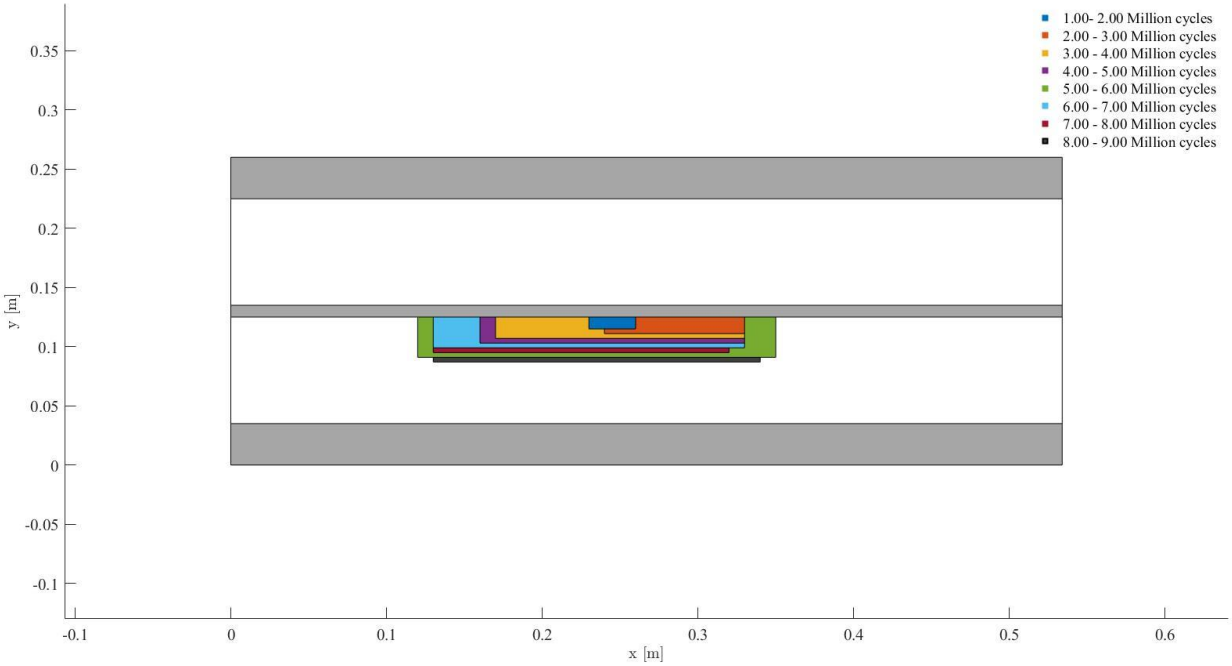

Figure 63 Length of detected crack per million cycles

4.5.2. Conclusion

The localization of the crack in the second tension test had a length of 230 mm, as detected via the AE method. This was only an 8% difference with the actual mode 1 crack with a length of 250 mm. This was within the 10%, so it can be concluded that the localization worked, even though not all of the dataset could be used for localization. In the last part of the monitoring of the specimen, no recorded events were found that would be useful for finding the crack length at 10.35 million cycles.

4.6. Discussion

All of the previous paragraphs explained a piece of the results separately, in this paragraph these pieces are combined to discuss what might have occurred during the second tension test.

First the duration of the signals where compared with a situation with fatigue and a situation without fatigue. The results that came out of the comparison is that there is a clear difference and this can be used in real life practices to identify possible fatigue signals in the field.

The average amplitude and the hit rate per cycle show very similar trends until 8.8 million cycles. The peaks for all the sensors occur at 6.3 million cycles and stays around this elevation until the 6.9 million cycles. In this period the displacement of the traverse is rises to a maximum. This may indicate that there is a great increase in the crack length in this period. However, the localized sources of the AE signals seem to indicate that the maximum crack length is reached right before these peaks in activity. This can be the result of the randomly selected signals, The sample may not represent all the data in the 6.3 to 6.9 million cycles period to a full extend. This is most likely also the case in the 2 to 3 million cycles period (Figure 63), where the crack seems to only grow in one direction but probably grew in both directions.

The possibility that the crack was in stable crack growth until 6.3 million cycles is debunked by the fatigue calculation. The stable crack growth that was calculated to last 1.5 million cycles. This has also been confirmed visually on the specimen (Figure 59). From the data it seems that crack growth reduced in activity after 6.3 million cycles. This is peculiar, because according to the literature the crack should grow exponentially until fracture when subjected to a constant cyclic stress. One explanation could be that the transition of crack growth from mode 1 to mode 3 requires more energy. When mode 3 crack growth was starting the traverse started to reposition, and therefore this length of the mode 3 crack was not taken into account. This mode 3 crack can also be created elongated during the opening of the specimen after the end of the experiment while in the machine,

For the part between 8.8 and 10.6 million cycles something really peculiar happened. The signals with sources outside of the crack development area overshadowed the recording in close proximity of the crack. We do not know what happens near the crack, because we cannot distinguish/detect it. (Figure 36). This is likely because the traverse repositioned itself and therefore the bolts connecting the specimen to the traverse started making noise this can been seen throughout the data.

The localization of the crack and its length tracing was successful and traced it early in the fatigue lifetime. This is seen in the blue section of Figure 61, here the fatigue calculation and the blue section match. The length of the eventual crack was 280mm after opening, this is mode 1 and mode 3 combined. The crack length that was measured before opening was quite accurate if looked at the numbers. The crack detected was 230 mm long the mode 1 crack, the measured length was 250mm. the detected crack still has a lot of uncertainty so the length detected is not to be seen accurate to the mm.

5. Conclusions

The first subquestion, “what is the ultrasonic background noise of the Hexapod, and in what way does it interfere with AEs from the fatigue cracks in the test specimen?”. From the characterization test and the experiments a clear method for identifying fatigue in a specimen has been derived, this is only true for data of a certain quality. If there is a significant amount of signals shorter than 500 microseconds the specimen will have most likely damage signals in it.

The settling of the specimen after mounting interferes with the data recording on the Hexapod. After this settling period, the machine does not interfere with the AE coming from the specimen in uniaxial direction. In the experiment the traverse started to repositioning itself. The settling time ending can easily be measured with the RMS. If the RMS drops significantly the settling time has come to an end. The settling time interferes with the AE data collection in a certain time period. In the two uniaxial experiments the settling time was around 14 hours. Since these tests had a long testing duration, the recording of the fatigue lifetime was not significantly affected by background noise of the settling time. The bending test had a duration of 8 hours and therefore did not surpass the 14 hour threshold which means the AE could not be analyzed. So, answering the first subquestion, the results show that the Hexapod has an influence on the AE. However, for long experiments in uniaxial direction, the settling time has a minimal impact.

Next the second subquestion of this thesis, which is “which features of the signal can be acquired and processed robustly for standard welded T-joints in laboratory conditions?” is answered. The main features of the signal that are useful is the duration, average amplitude and the hits per cycle. These gave a decent picture of what was happening with the specimen in tension.

The third question is “what are the essential features of AE signals released by fatigue cracks under multiaxial loading?” This question could not be answered because there were no multiaxial experiments and therefore nothing can be said about the features in the multiaxial case.

The answer of the main research question “*Is it possible to detect a fatigue crack with the AE method, and how can the crack length and position be estimated in the tubular welded T-joint specimen for multiaxial loading”.* The localization algorithm of tracing and locating the crack was successful. The localization could already trace the crack early in the crack growth phase. The correlation between the fatigue calculation and the tracking match.

The results of this feature study gave a peak at 6.3 million cycle, the maximum length detected was between 5-6 million cycles. This might suggest that after this peak the reduction of activity is caused by the switch from mode 1 to mode 3 crack growth.

In conclusion the title of this thesis is answered “Feasibility of Acoustic Emission Methods for Fatigue Monitoring in Tubular Double Side Welded T-joints”. Yes it is considered feasible for specimen to be monitored with AE although the case study was uniaxial it is believed that this can be applied for multiaxial testing.

6. Recommendations

Applying AE of specimens under multiaxial loading:
For further research, more specimens should be tested with AE in the Hexapod to gather more data to compare with the results of this thesis. These test should have again a tension and eventually multiaxial test to see if other sources emerge other than fatigue signals.

Redesigning the connection of the Hexapod to the specimen:
The bolting system of the hexapod is not ideal for the current testing with AE. Looking for alternative connections for this testing machine. This should eliminate the connection being governing when the traverse changes direction. This will be a future problem for multiaxial testing. Next to the bolting system, further research of the settling time to determine the exact cause of this phenomenon with the goal to eliminate it for future tests.

Robust and reliable automatic time picking scheme:
For the automation and processing of an immense amount of data, the development of a robust time picking scheme for the localization and therefore more signals can be processed for the localization of the crack. Therefore giving more data point and giving a more accurate picture of the crack development.

7. Reflection

This thesis did not have a smooth ride. During the 18 months the main research question changed significantly multiple times during the research in part of having a too ambitious goal, delays and cancelation of certain experiments. The greatest contributor for the extensive delay of the Bar specimen that was eventually canceled after a year of failed experiments. The new focus became testing on the newly commissioned Hexapod. The characterization test was done at the end of January. The first real test data come in at the end of May this was then processed and eventually I will be graduating at the end of August. This was not ideal for me because I am more of a practical person than a theoretical one. The lack of data to process meant I was emerge in the literature, there was not a lot of specific literature because this is state of the art research that was being conducted. So a broad study into Fatigue and AE was don. I noticed that the moment I had data to process, my comprehension of the AE and the implication of it grew astronomically. Because this graduation took so long the end was a real sprint to finish the thesis and to make it into a respectable thesis report. I noticed my writing skills have improved but it was not a talented writer. The fact that I'm dyslexic did not help the process. Eventually the dyslexia font I used to read with ease helped me read for long periods and the great guidance I got from a the people around me, the thesis could finally be finished.

In hindsight I would have done things differently but that is also part of the process. Next time I would make that I am not dependent on experiment where I cannot fix the problem myself. Because I work in a workshop this could have helped me greatly. If I am fully responsible for the experiment I think I would find a way to make it work and not have to wait. This process would probably give me insights in the phenomenon I would be studying. I notice that working and discussing with other people works much better for me than doing it all alone in a bubble. The last months I had an intense cooperation with Pooria and Bart, this helped me a lot to improve my thesis.

8. Bibliography

Blom, A., Hedlund, A., Zhao, W., Fathalla, A., & Weiss, B. (1985). Short fatigue crack growth in Al 2024 and Al 7475. Behaviour of short fatigue cracks. Sheffield : EGF 1.

Demonstrating an Earthquake's Seismic Waves. (2017, Juni 21). Retrieved from http://ocean.si.edu: http://ocean.si.edu/ocean-videos/demonstrating-earthquakes-seismic-waves

den Besten, H. (2017, May 01). *Fatigue and Fracture in Marine Structures*. Retrieved from https://blackboard.tudelft.nl/bbcswebdav/pid-2940234-dt-content-rid-10271909_2/courses/41456-161704/OE44085%2301b_FatigueAndFractureFundamentalsInMaterials.pdf

Dragt, S. (2017, May 01). Private Confersation at Maritime Match day. Delft.

Earthquake: Body Waves & Surface Waves. (2017, June 29). Retrieved from construction and design: http://www.constructionandesign.com/2016/02/earthquake-body-waves-surface-waves.html

Hall, E. (1951). The Deformation and Ageing of Mild Steel: III Discussion of Results. *Proc. Phys. Soc. London.* , 64:747.

Kaiser, J. (1953). Experimental Observations and Theoretical Interpretations of Sound Measurement During Tensile Loading of Metals. *Archiv fur das Eisenhuttenwesen Vol. 24, No. 1/2*, 43-45.

Lee, A., Botten, S. F., van der Horn, E., & Wang, G. (2013). Structural Health Monitoring on Mooring Chain Using Acoustic Emission Testing. *Prads2013.* Changwon City, Korea.

Marks, R. (2016, January 7). *Lamb Wave Interaction with Adhesively Bonded Stiffeners and Disbonds Using 3D Vibrometry*. Retrieved from mdpi: http://www.mdpi.com/2076-3417/6/1/12/htm

Nguyen, P., Vantomme, J., & Aggelis, D. (2016). Acoustic Emission Monitoring of Reinforcing Bars Pull-Out. *World Conference on Non-Destructive Testing.*

Pahlavan, P., Paulissen, J., Pijpers, R., Hakkesteeg, H., & Jansen, R. (2014). Acoustic Emission Health Monitoring of Steel Bridges. *European Workshop on Structural Health Monitoring*, (pp. 49-62).

Passchier, C., & Trouw, R. (2005). *Microtectonics.* New York: Springer.

Petch, N. (1953). The Cleavage Strenght of Polycrystals. *J. Iron Steel Inst London*, 173:25-28.

Portevin, A., & Le Chatelier, F. (1923). 176. *Compte. Rendu.*, 507-510.

Rogers, L. (2001). *Structural and Engineering Monitoring by Acoustic Emission Methods-Fundamentals and Applications.* London: Technical Investigation Department Lloyd`s Register.

Rogers, L. (2001). *Structural and Engineering Monitoring by Acoustic Emission Methods: Fundamentals and Applications.* London: Technical Investigation Department Lloyd`s Register of Shipping.

Sanchez-Molina, D. (2015, July). *A Stochastic Model for Soft Tissue Failure using Acoustic Emission data*. Retrieved from Researchgate.net: https://www.researchgate.net/publication/280945844_A_Stochastic_Model_for_Soft_Tissue_Failure_using_Acoustic_Emission_data

Scheeren, B. (2017). *On the Development of a Volumetric Acoustic Emission Fatigue Crack Monitoring System.* Delft: TU Delft.

Schijve, J. (2009). *Fatigue of Structures and Materials .* Delft, the Netherlands: Springer.

Schofield, B. (1961). *Acoustic emission under applied stress.* Boston: Lessels and associates.

Schutz, W. (1996). A history of fatigue. *Engineering Fracture Mechanics*, 263-300.

Steffes, C. (2014). *Field Experiments for TDoA-based Localisation of GSM Base Stations. Sensor Data Fusion: Trends, Solutions, Applications.*

Tada, H., Paris, P. C., & Irwin, G. R. (2000). *The Stress Analysis of Cracks Handbook.* New York: ASME Press.

TU Delft. (2018, Marche 21). Retrieved from https://www.tudelft.nl/en/3me/organisation/organisation/departments/maritime-and-transport-technology/research/ship-and-offshore-structures/facilities/hexapod/

Vallen Systeme GmbH. (2015). *AMSY-6 System Description.* Icking, Germany.

ZfP-Wiki. (2018, July 26). Retrieved from ZfP Lehrstuhl fur Zerstoringsfreie Prufung: http://zfp.cbm.bgu.tum.de/mediawiki/images/5/5b/Hsu_nielson_v2.jpg

Appendix A

Here all the histograms of the calibration test on the hexapod with on the x axis the duration and on the y axis the amount of hits in that Section of the duration.

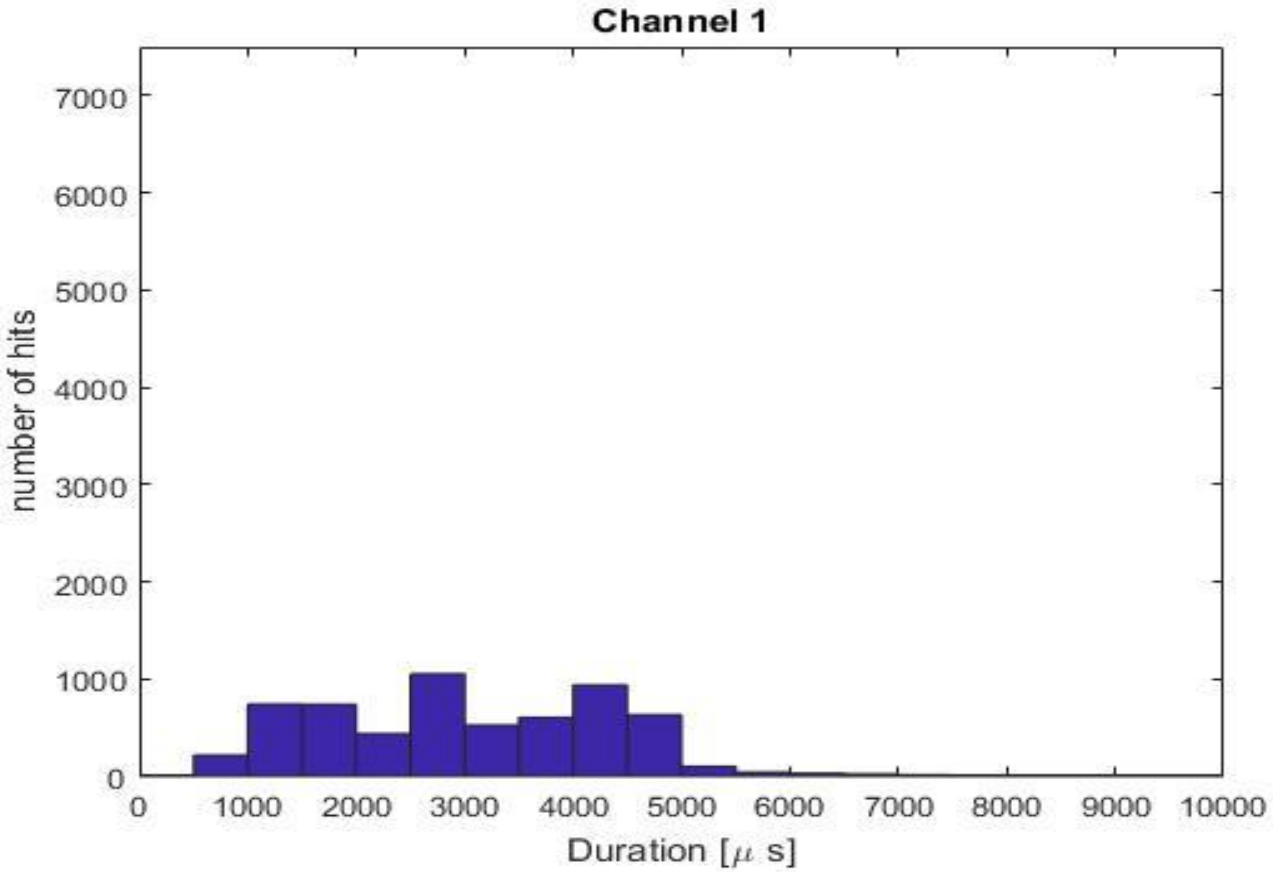

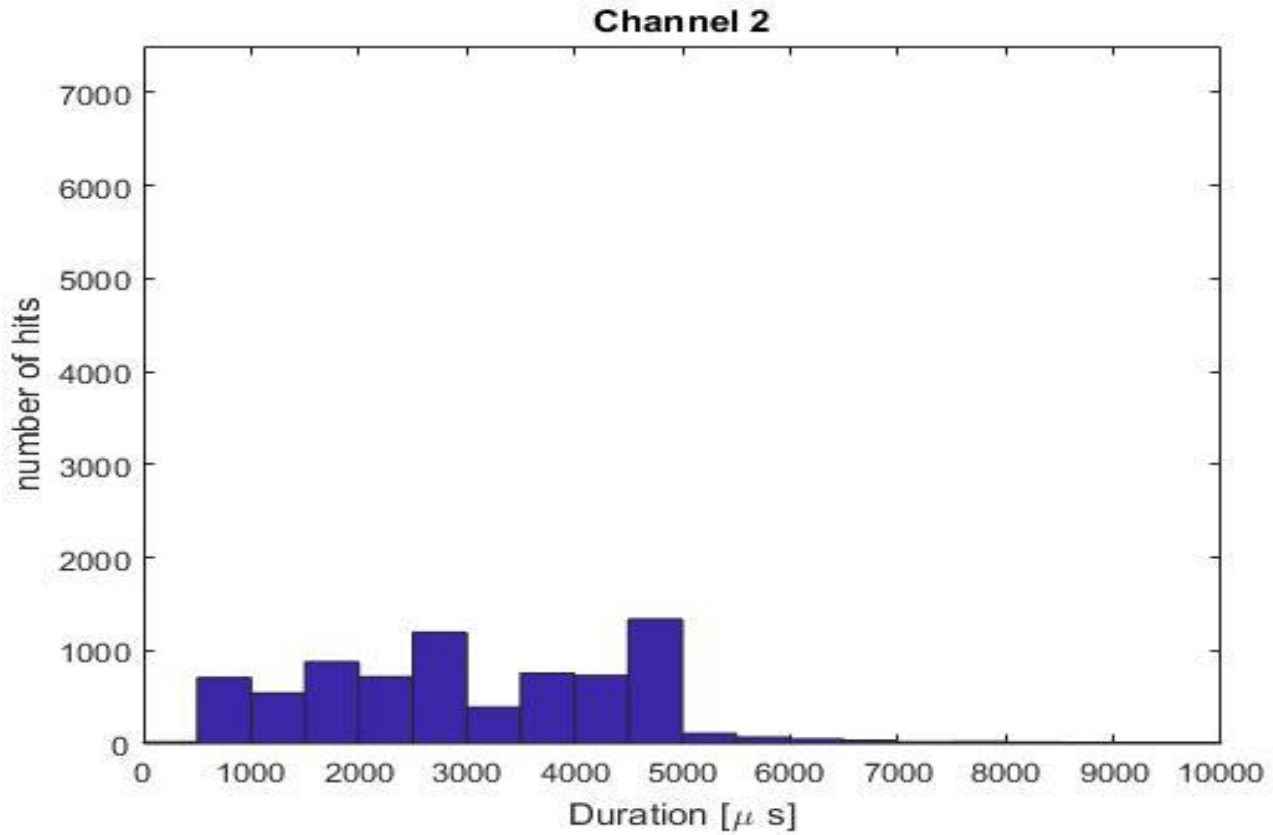

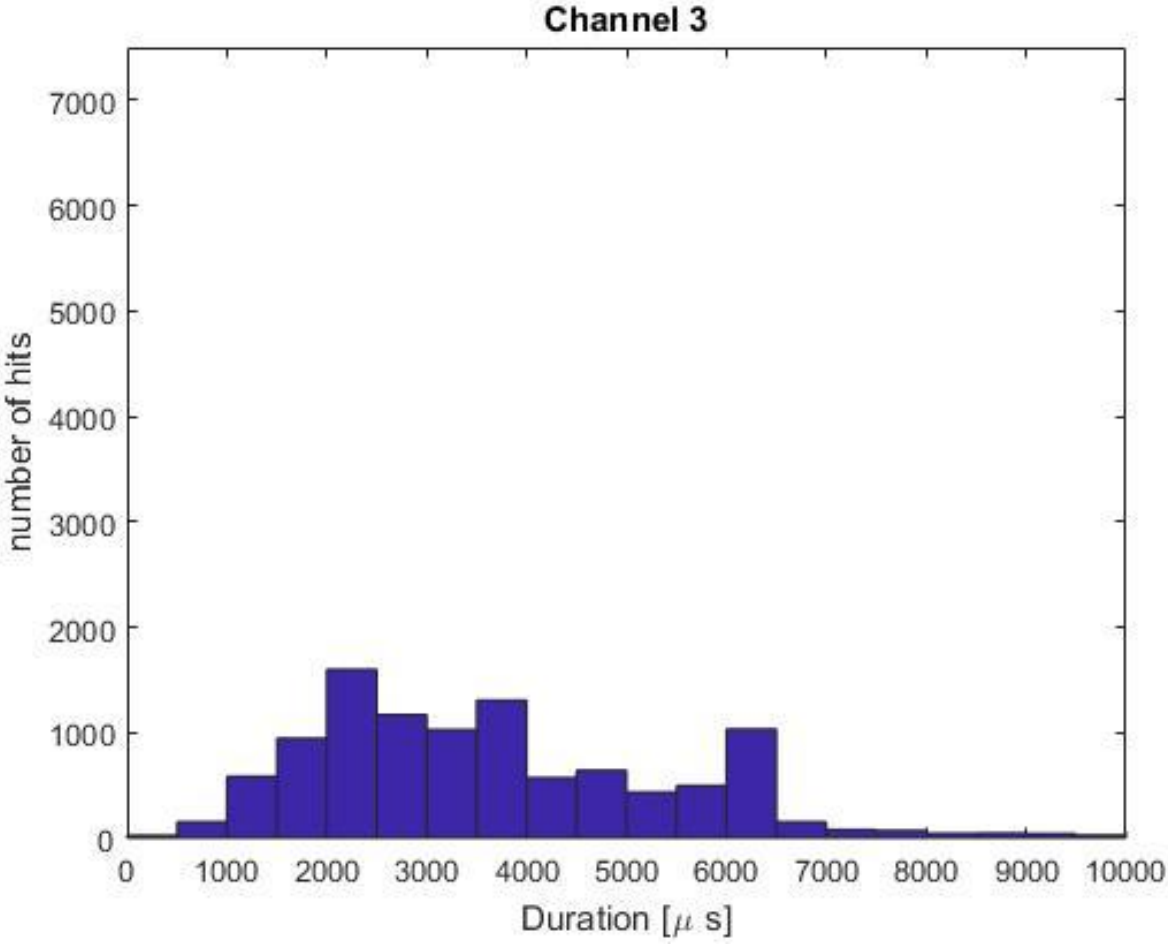
Channel 3
number of hits
Duration [μ s]
0
1000
2000
3000
4000
5000
6000
7000
8000
9000
10000

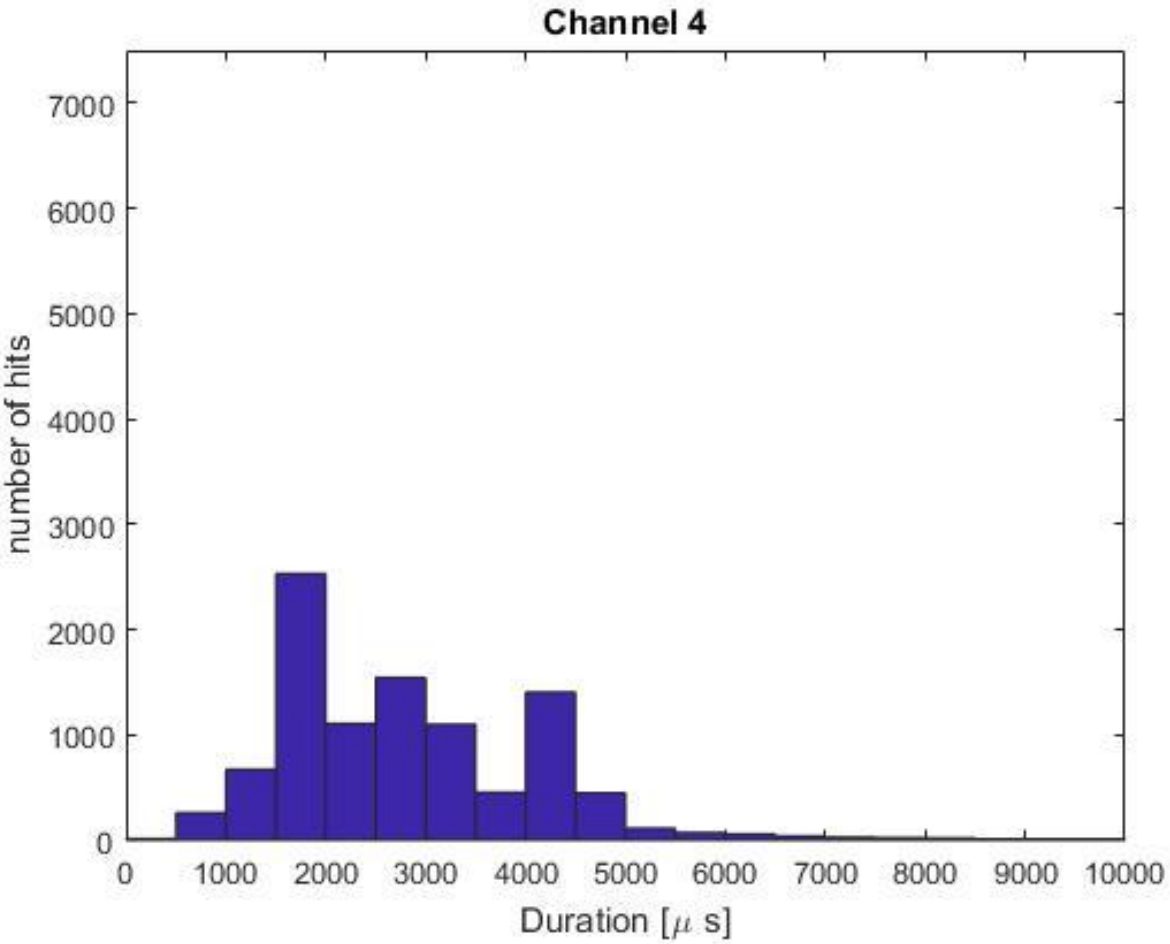
Channel 4
number of hits
Duration [μ s]
0
1000
2000
3000
4000
5000
6000
7000
8000
9000
10000

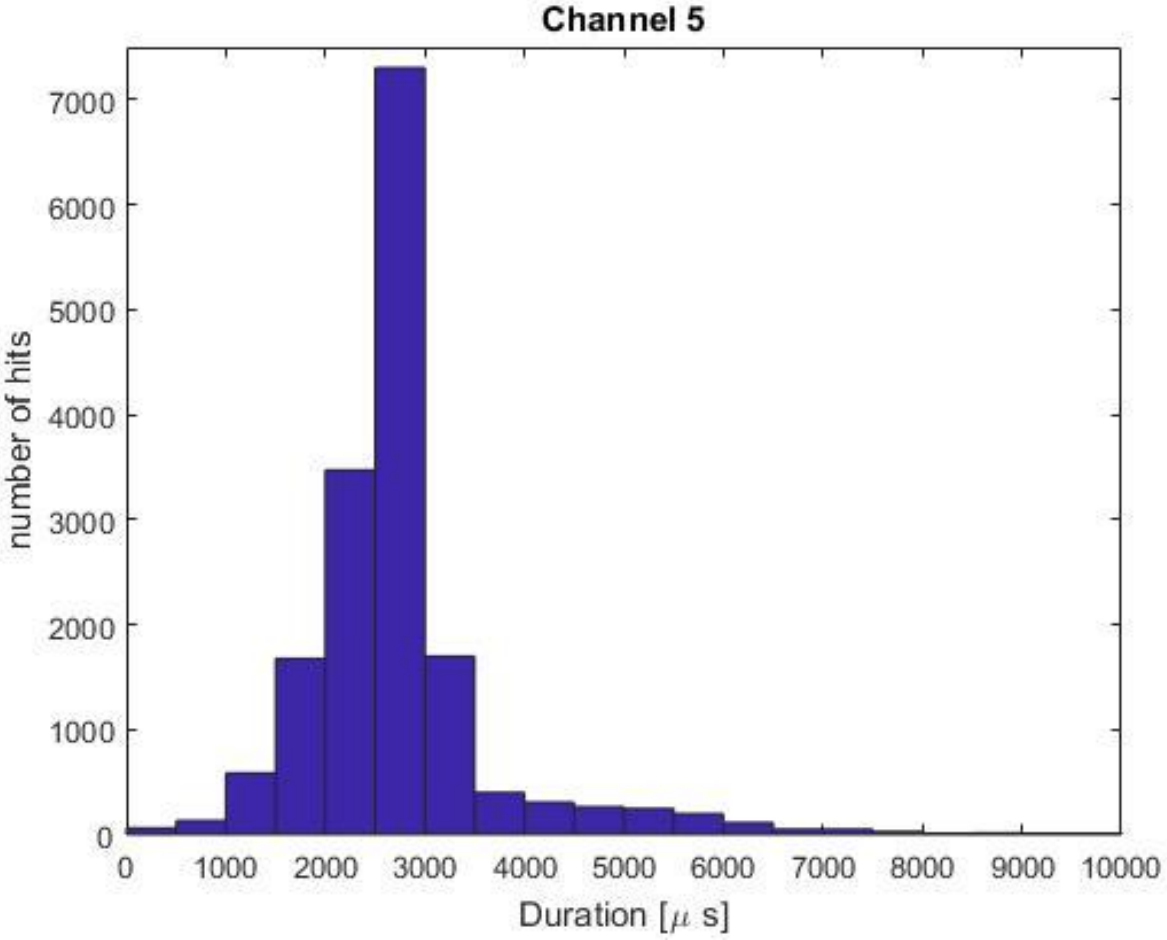
Channel 5
number of hits
Duration [μ s]
0
1000
2000
3000
4000
5000
6000
7000
8000
9000
10000

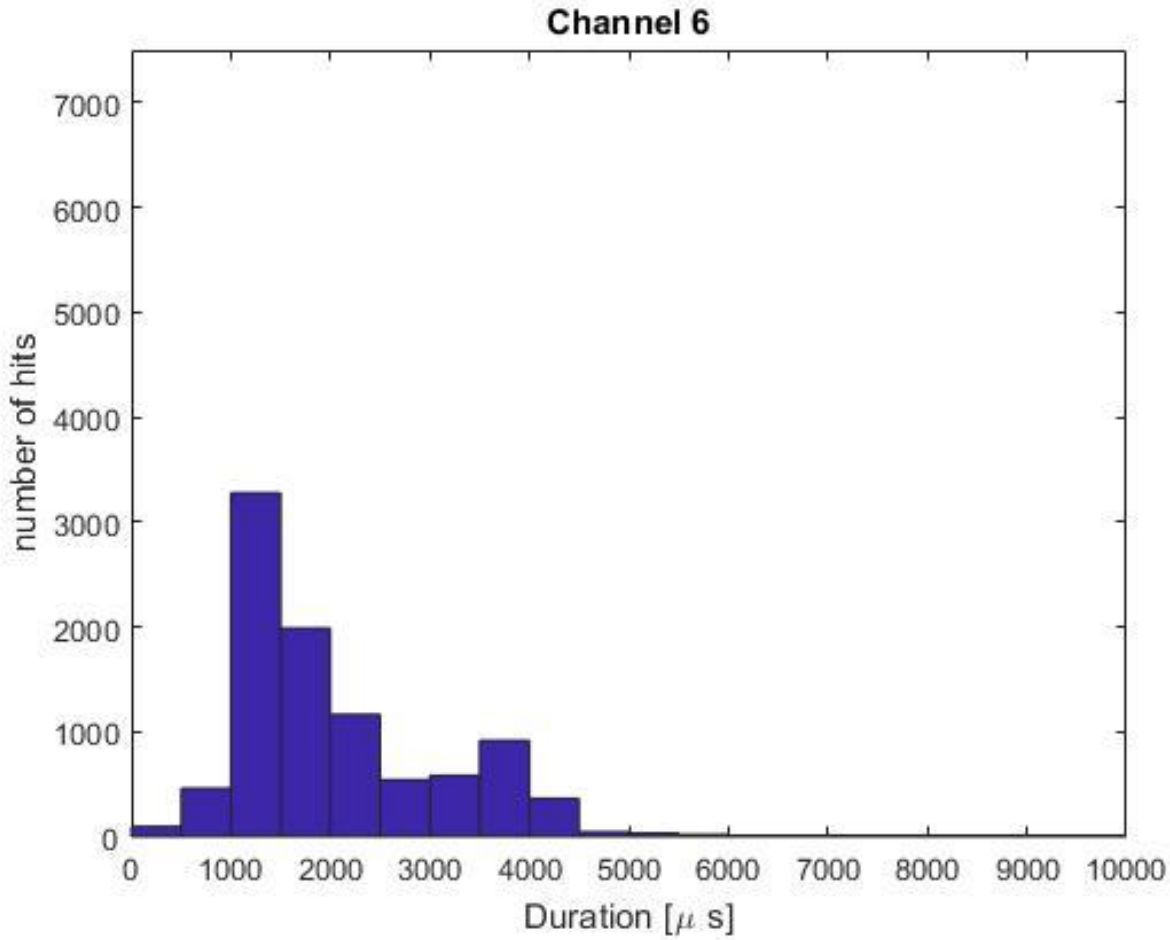
Channel 6
number of hits
Duration [μ s]
0
1000
2000
3000
4000
5000
6000
7000
8000
9000
10000

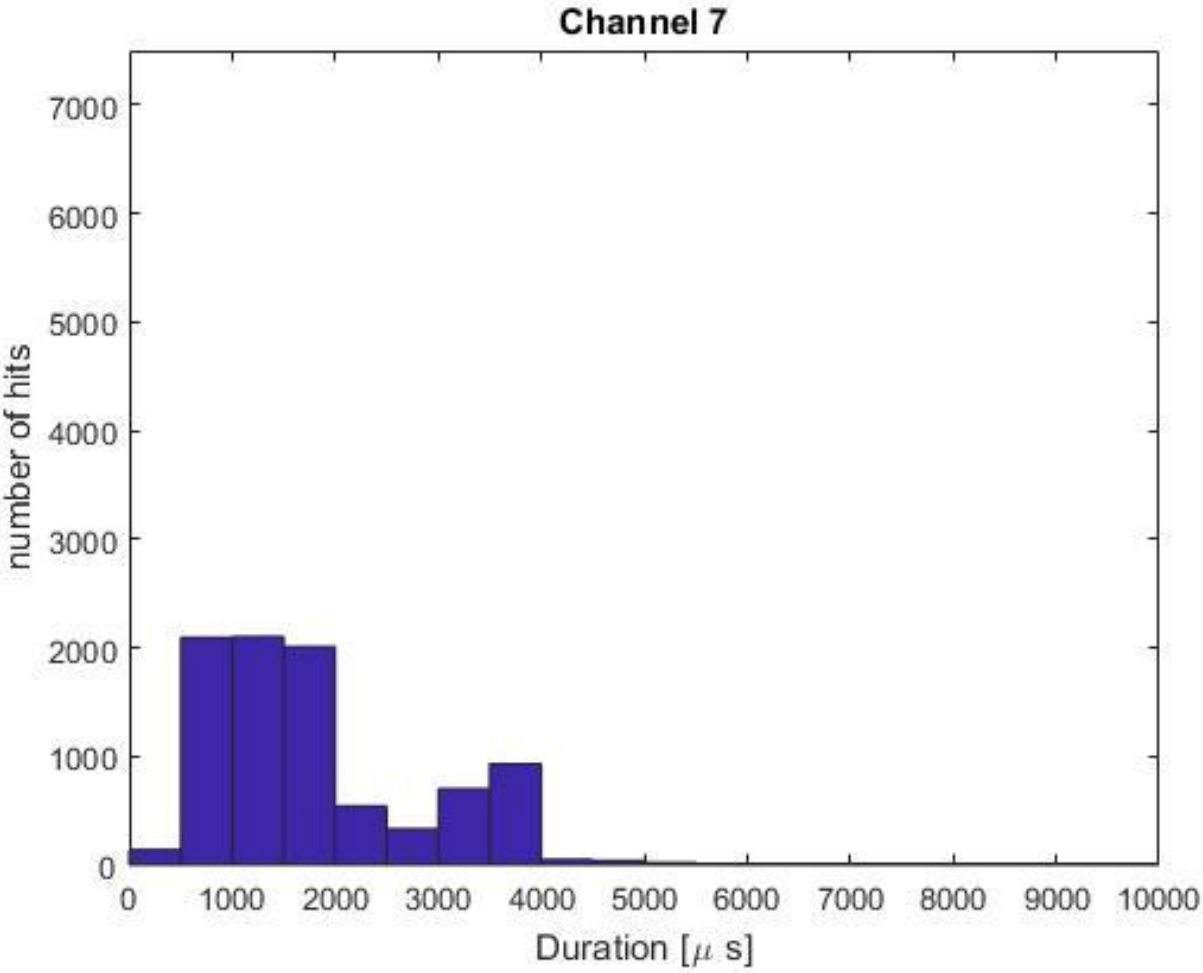
Channel 7
number of hits
Duration [μ s]
0
1000
2000
3000
4000
5000
6000
7000
8000
9000
10000

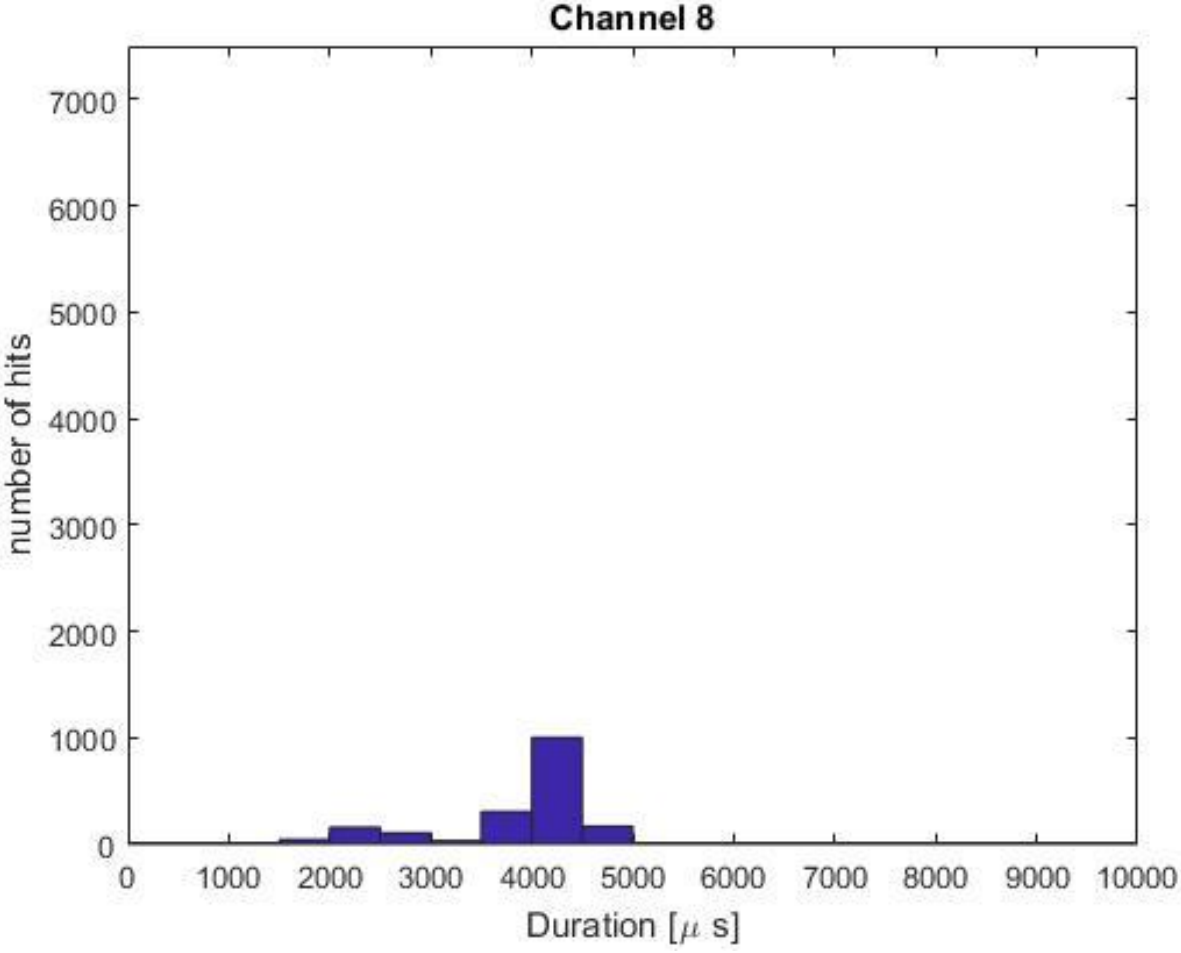
Channel 8
number of hits
Duration [μ s]
0
1000
2000
3000
4000
5000
6000
7000
8000
9000
10000

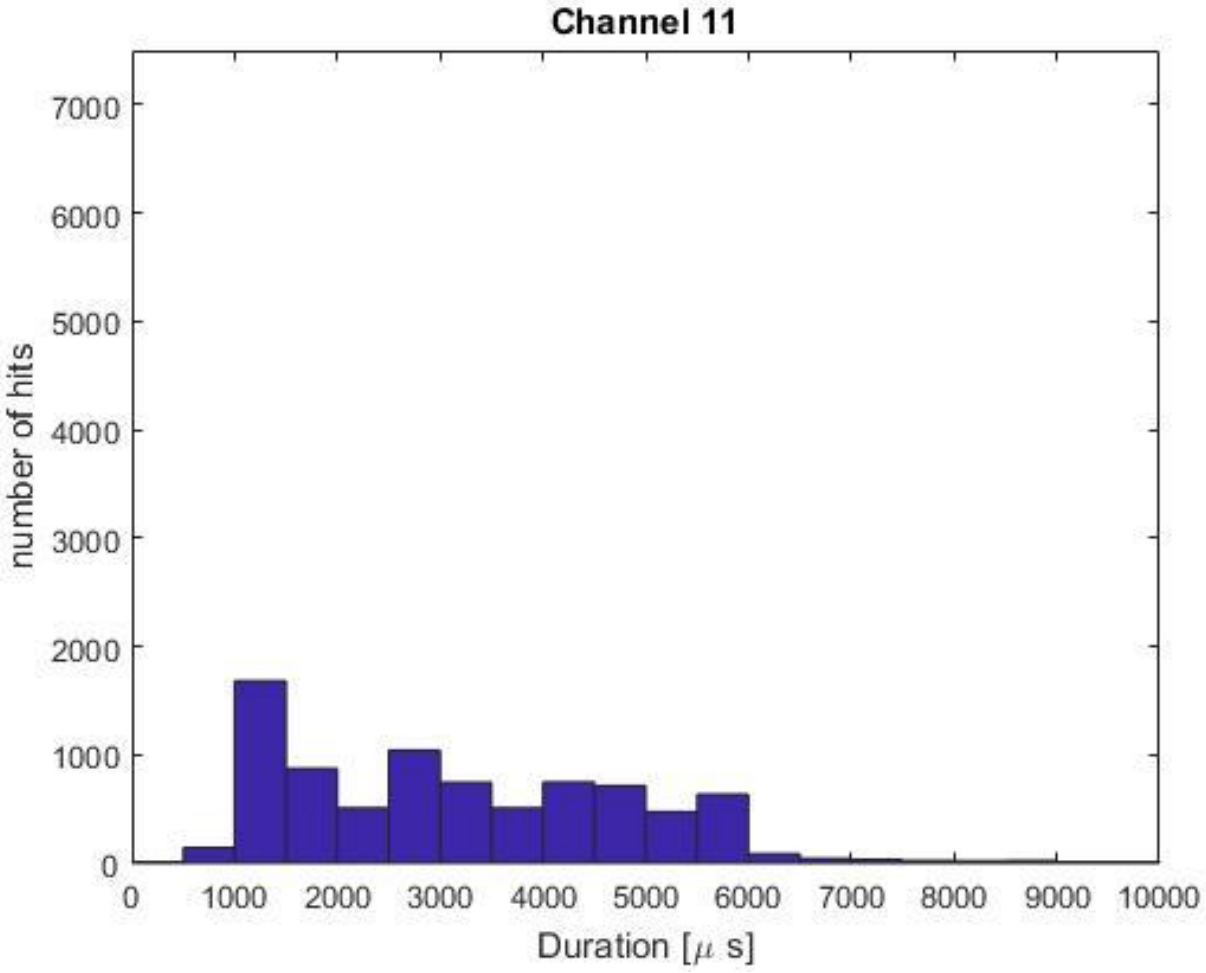
Channel 11
number of hits
Duration [μ s]
0
1000
2000
3000
4000
5000
6000
7000
8000
9000
10000

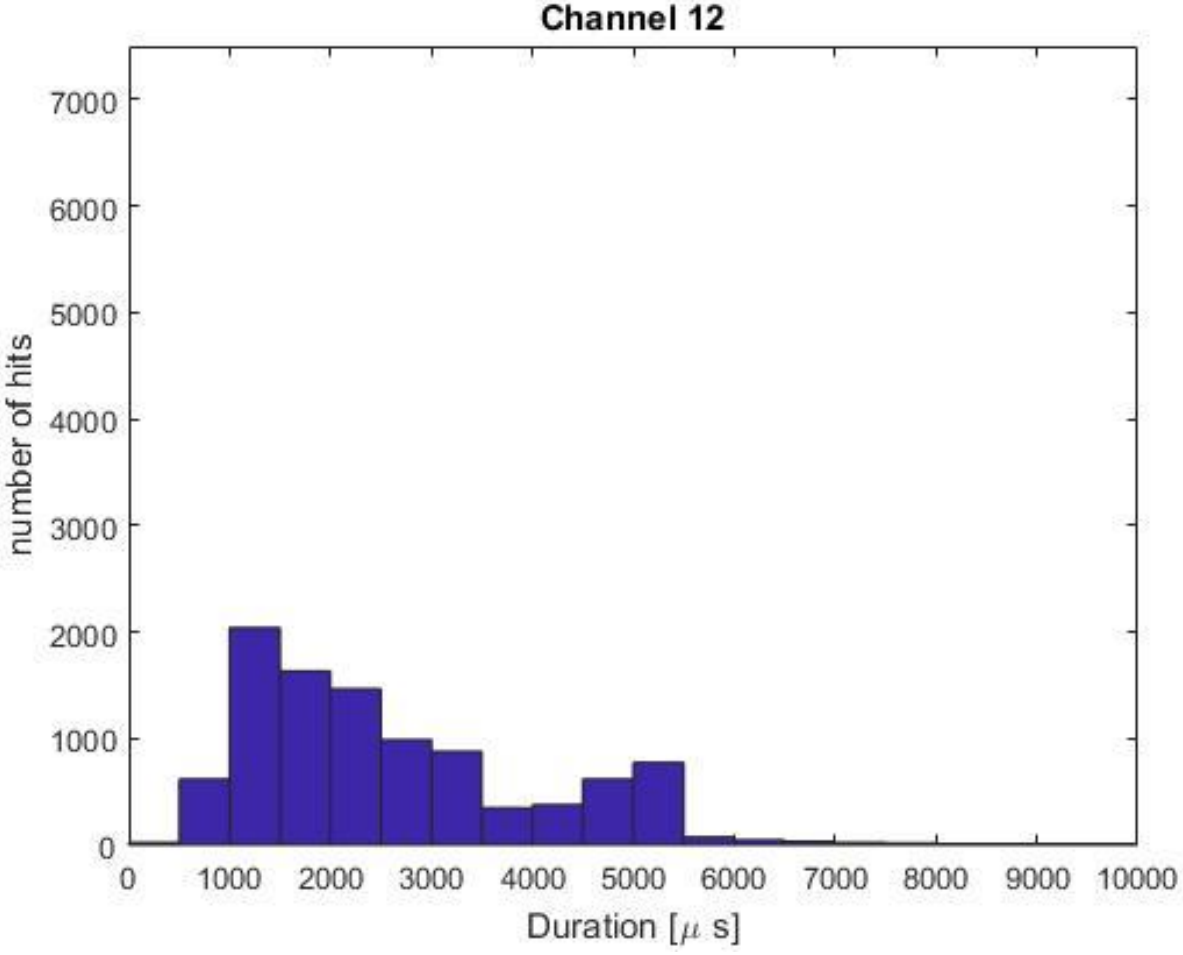
Channel 12
number of hits
Duration [μ s]
0
1000
2000
3000
4000
5000
6000
7000
8000
9000
10000

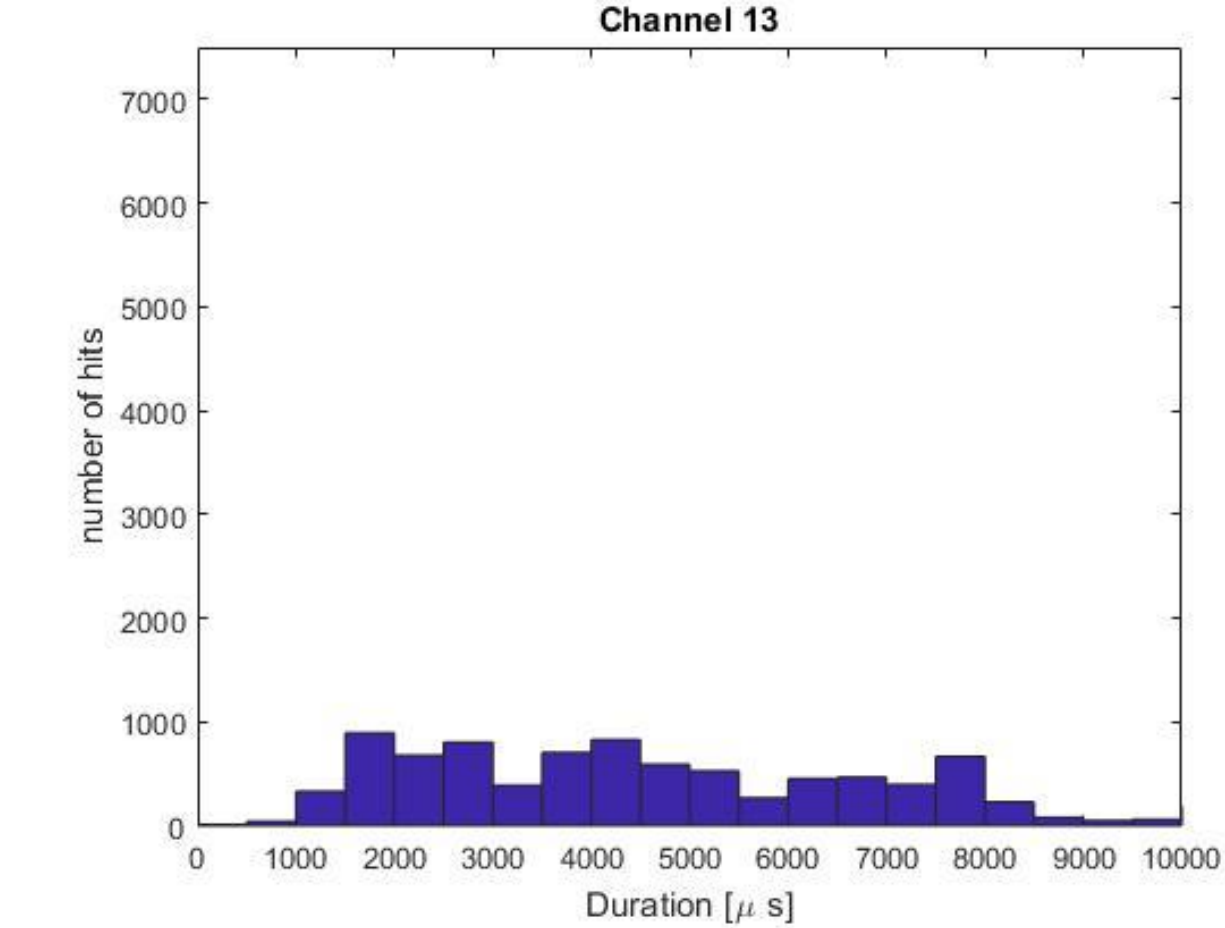
Channel 13
number of hits
Duration [μ s]
0
1000
2000
3000
4000
5000
6000
7000
8000
9000
10000

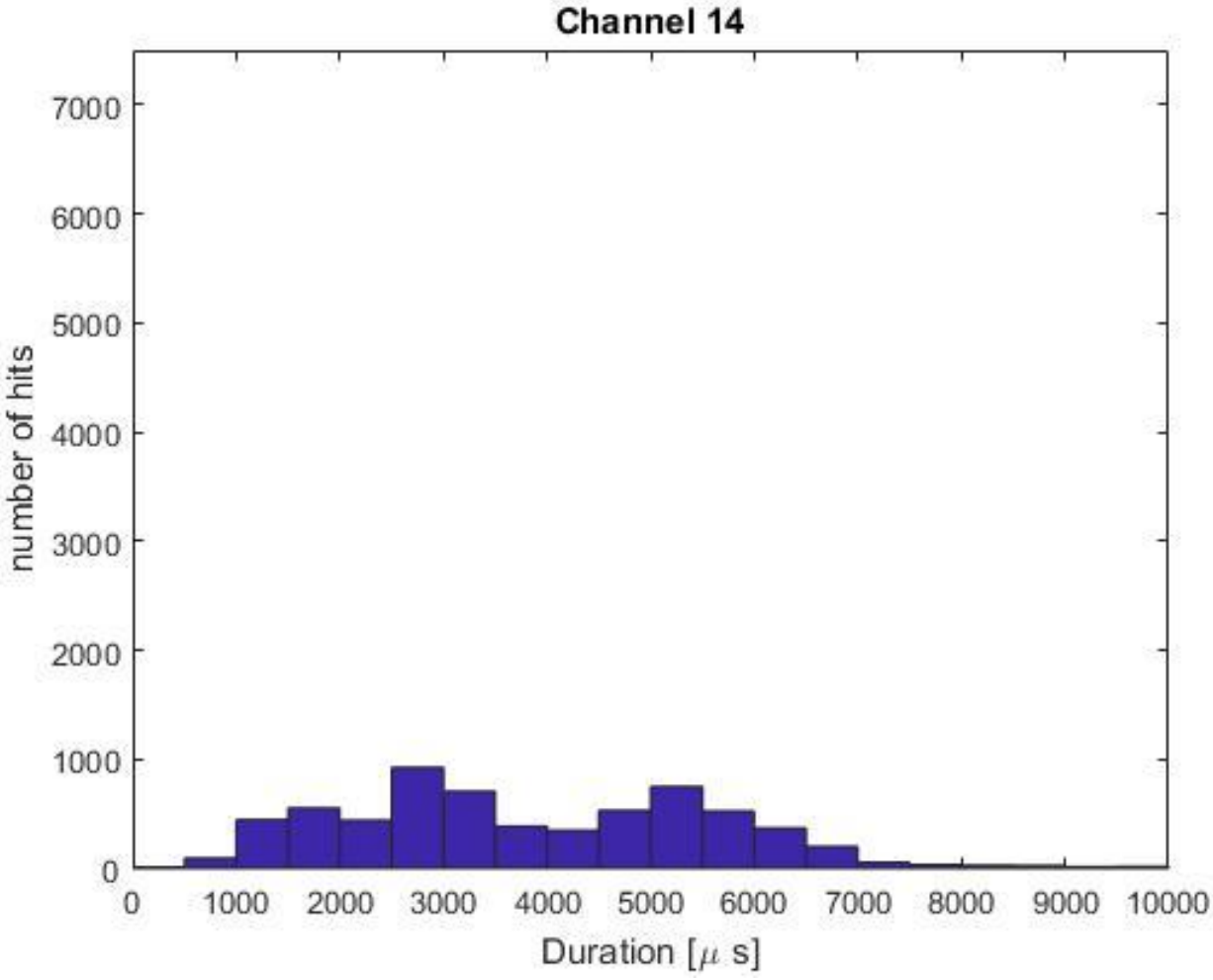
Channel 14
number of hits
Duration [μ s]
0
1000
2000
3000
4000
5000
6000
7000
8000
9000
10000

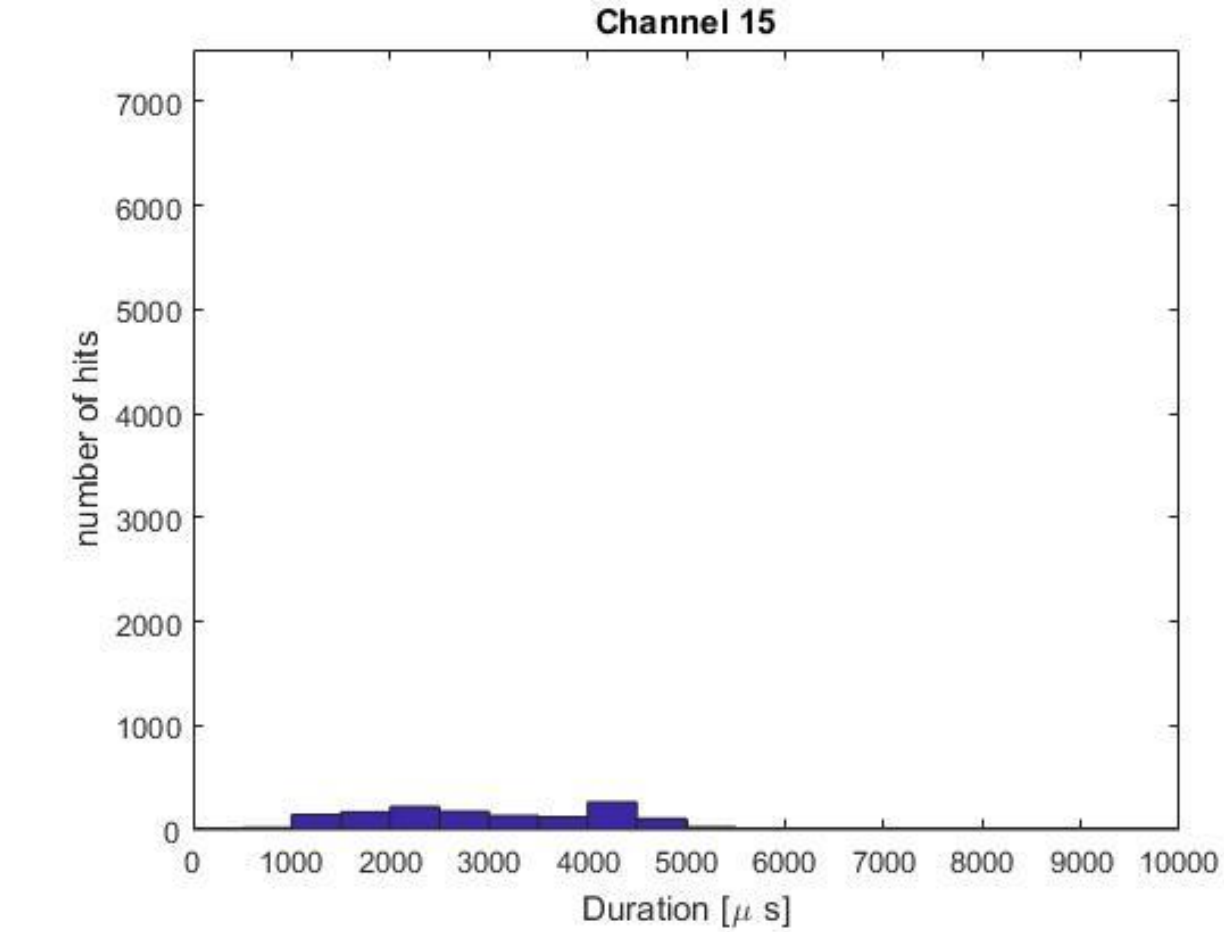
Channel 15
number of hits
Duration [μ s]
0
1000
2000
3000
4000
5000
6000
7000
8000
9000
10000

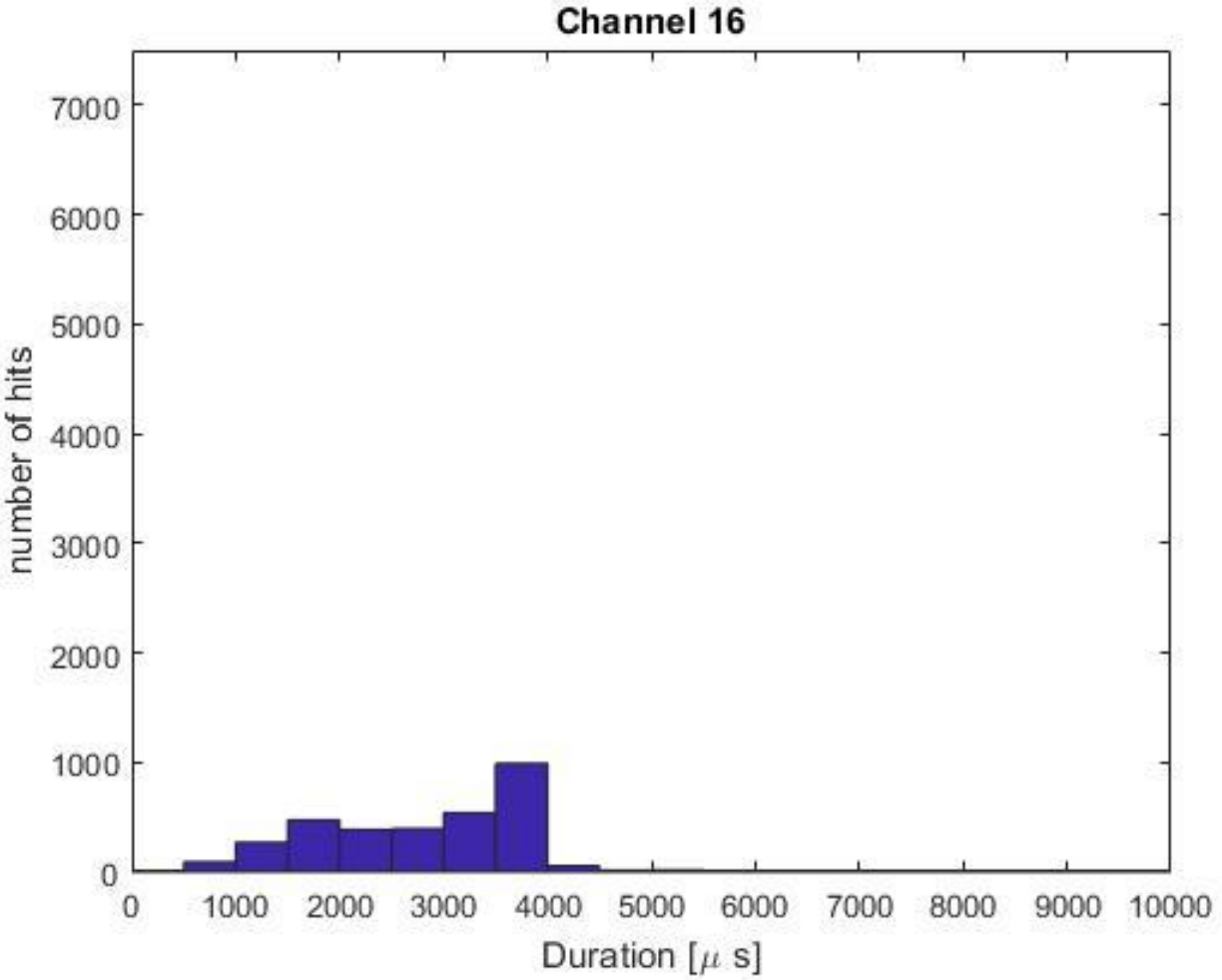
Channel 16
number of hits
Duration [μ s]
0
1000
2000
3000
4000
5000
6000
7000
8000
9000
10000

Appendix B

Proposal PLB test Welded specimen

This test is to see how a weld influences the Acoustic emission propagation will go through the weld.

Why?:

For future tests with the hexapod, a welded sample (see Figure 62) will be tested until fracture, this fracture will be caused by fatigue damage. Because it is welded on two sides, there are no means of knowing where the crack will start on the top or at the bottom of the weld. Now the question arises, what the influence is of the welded material on a signal going through it and how the signal changes?

How:

The test that will be set up, consists of a welded sample that is used in the research of 4D-Fatigue. This sample will not be mounted in the any machinery. the main sensors are positioned above the topside of the weld of the specimen. The sensor will be about 10mm from the weld and right under in the same position a second main sensor under the weld will also be 10mm from the weld. Around the Main sensor (sensor 1 and 5), Control sensors (sensor 2-4 and 6-8, see figure 1) will be placed with the same distance the two main sensors are apart from each other, this will be a distance of 50mm. for the sensors two and three, the thickness of the material is the same. For the control sensor 4 the thickness varies because this sensor is near the flange and the material gets thicker closer to the flange. The test itself will have 10 PLB (pencil lead break) test per sensor for calibration and have 20 pulsing cycles for later analysis.

Results:

Out of the data generated by the PLB test, there is on one side the signal going through the welded material and the other signal going through the steel. These features of the signal can be compared, this will give an insight of how the thickness and the weld changes the signal on sample.

Figure 64 Experimental set-up

Appendix C

Tubular specimen technical drawing

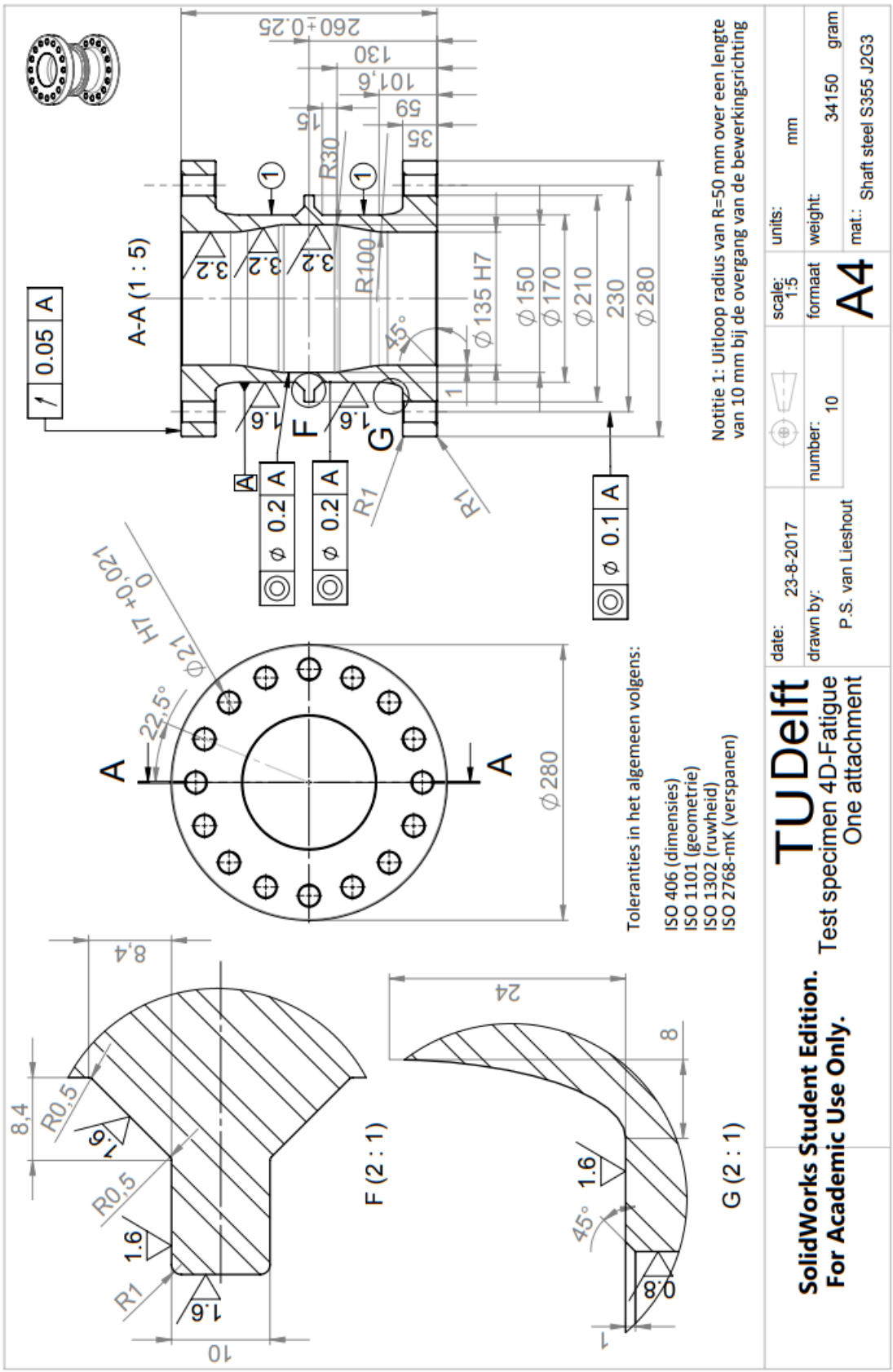

Appendix D

Graphs of the Hit Cycle rate per Channel

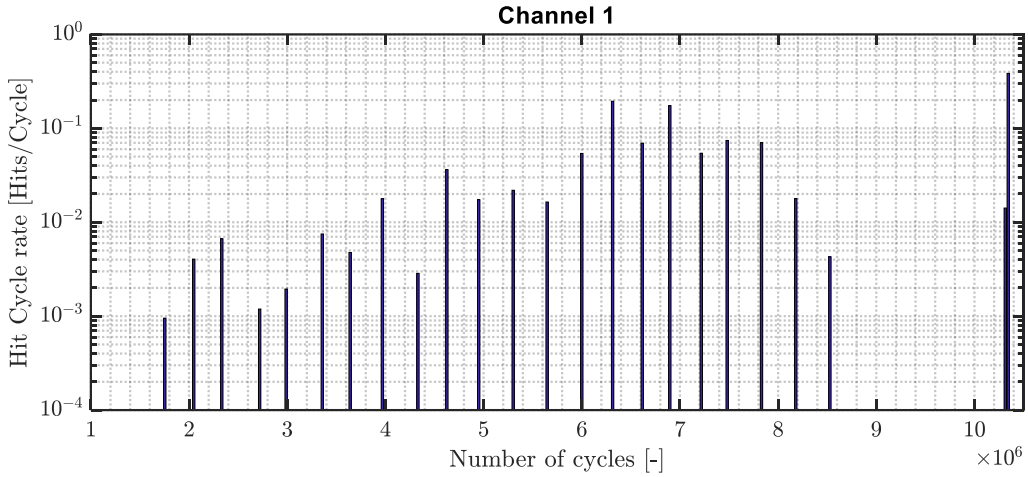

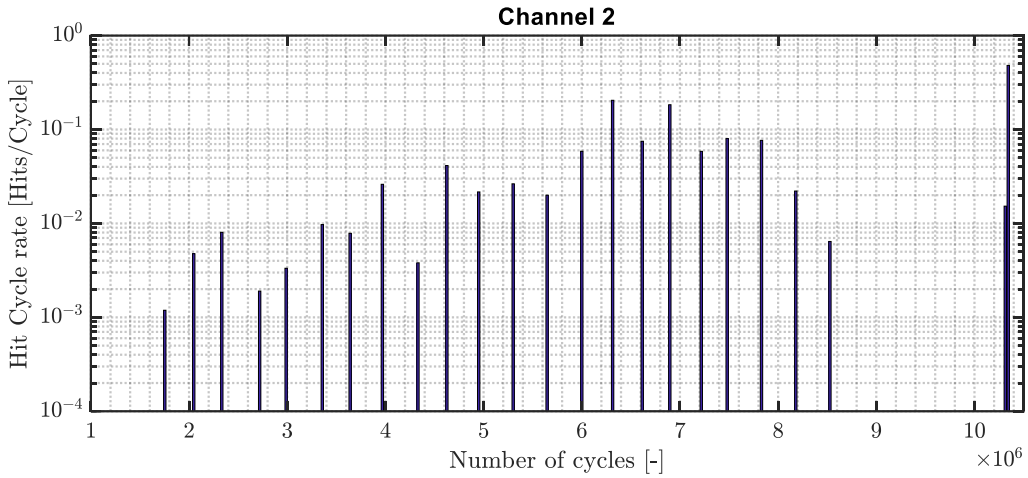

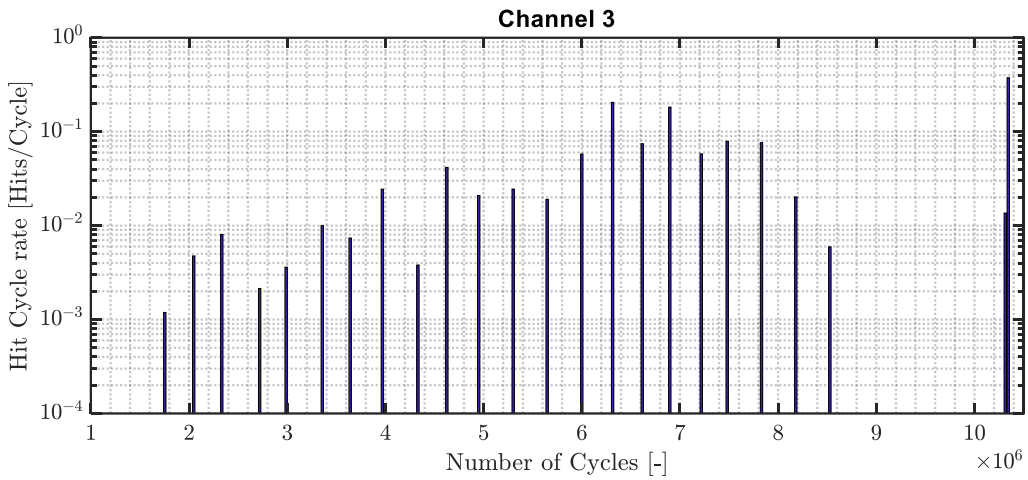

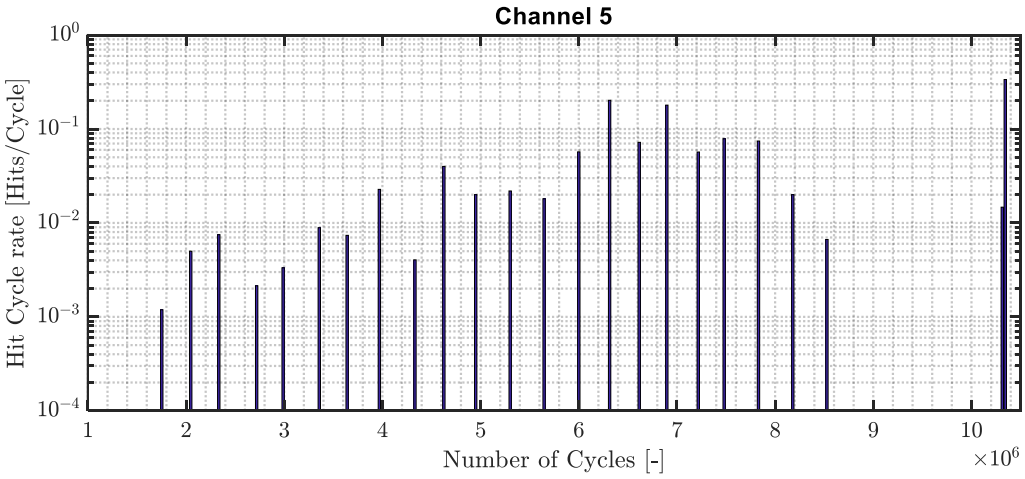
Channel 5
Hit Cycle rate [Hits/Cycle]
10^{0}
10^{-1}
10^{-2}
10^{-3}
10^{-4}
1 2 3 4 5 6 7 8 9 10
Number of Cycles [-]
$\times 10^{6}$

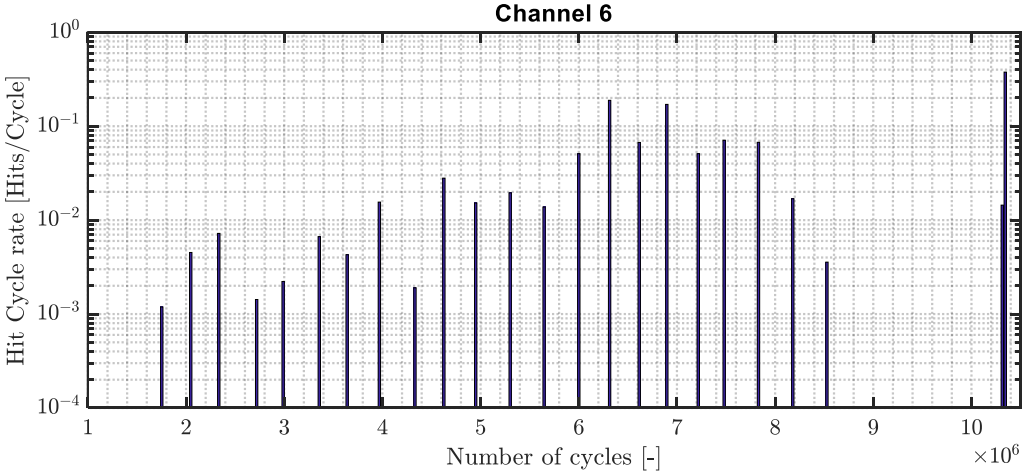
Channel 6
Hit Cycle rate [Hits/Cycle]
10^{0}
10^{-1}
10^{-2}
10^{-3}
10^{-4}
1 2 3 4 5 6 7 8 9 10
Number of cycles [-]
$\times 10^{6}$

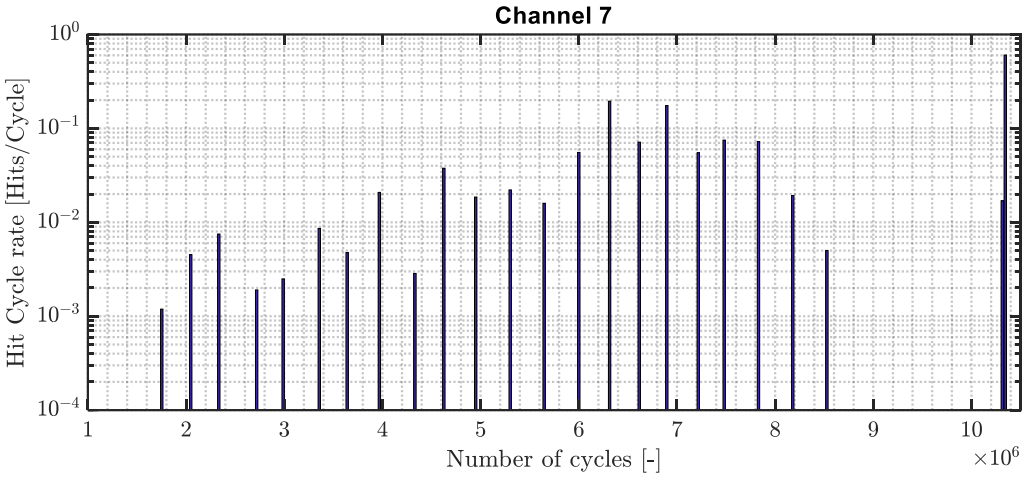
Channel 7
Hit Cycle rate [Hits/Cycle]
10^{0}
10^{-1}
10^{-2}
10^{-3}
10^{-4}
1 2 3 4 5 6 7 8 9 10
Number of cycles [-]
$\times 10^{6}$

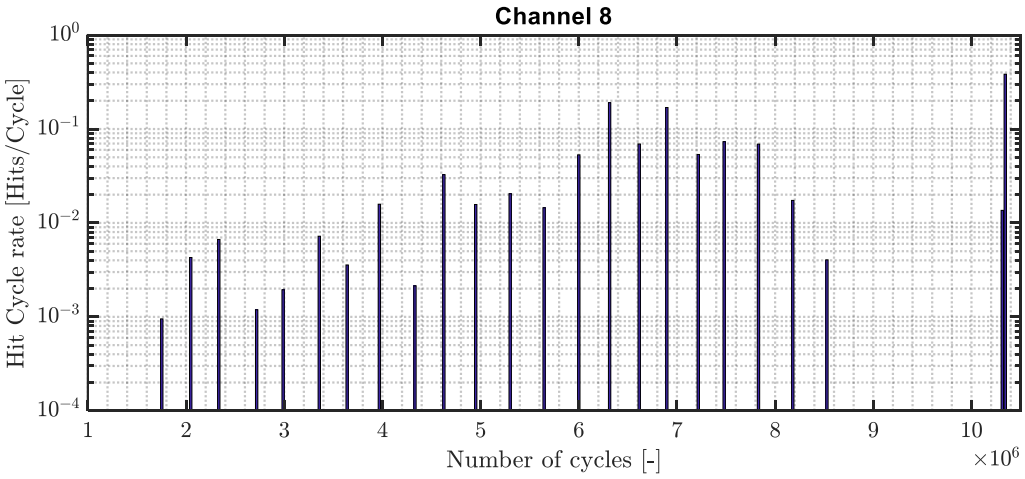
Channel 8
Hit Cycle rate [Hits/Cycle]
10^{0}
10^{-1}
10^{-2}
10^{-3}
10^{-4}
1 2 3 4 5 6 7 8 9 10
Number of cycles [-]
$\times 10^{6}$

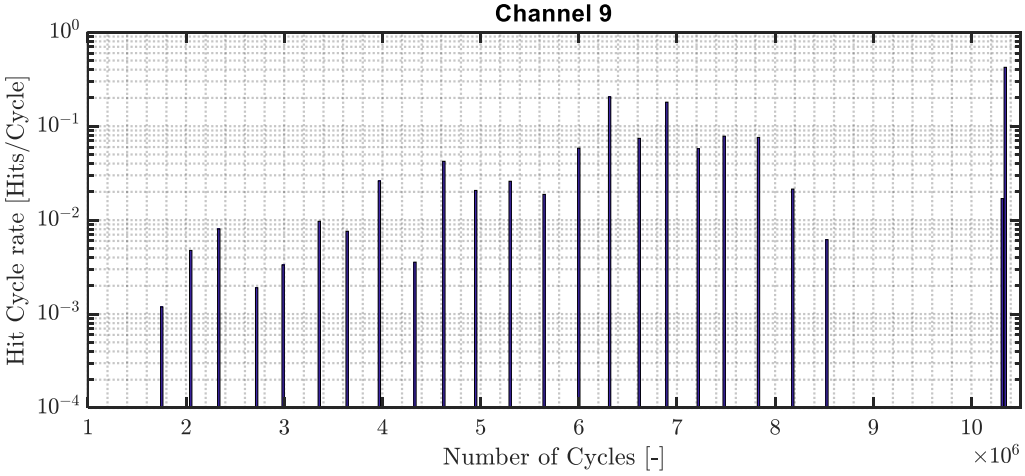
Channel 9
Hit Cycle rate [Hits/Cycle]
10^{0}
10^{-1}
10^{-2}
10^{-3}
10^{-4}
1 2 3 4 5 6 7 8 9 10
Number of Cycles [-]
$\times 10^{6}$

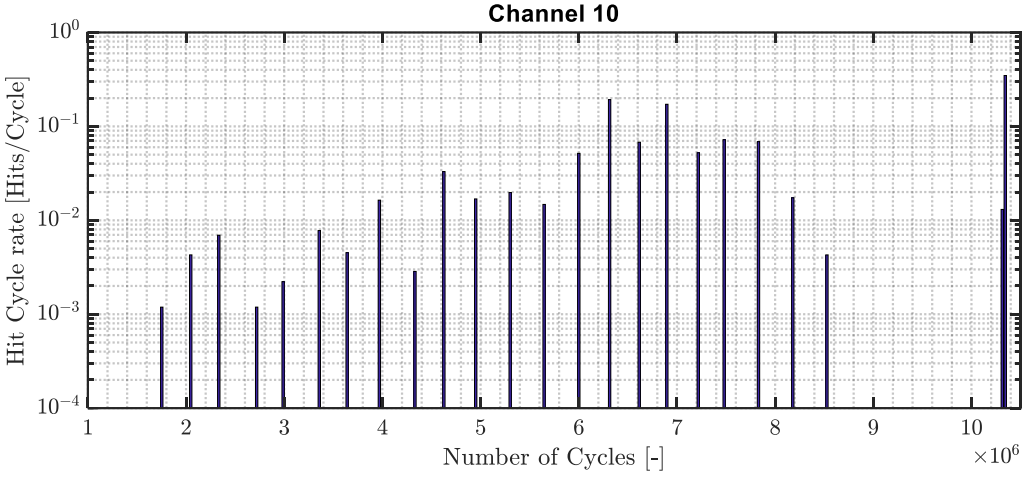
Channel 10
Hit Cycle rate [Hits/Cycle]
10^{0}
10^{-1}
10^{-2}
10^{-3}
10^{-4}
1 2 3 4 5 6 7 8 9 10
Number of Cycles [-]
$\times 10^{6}$

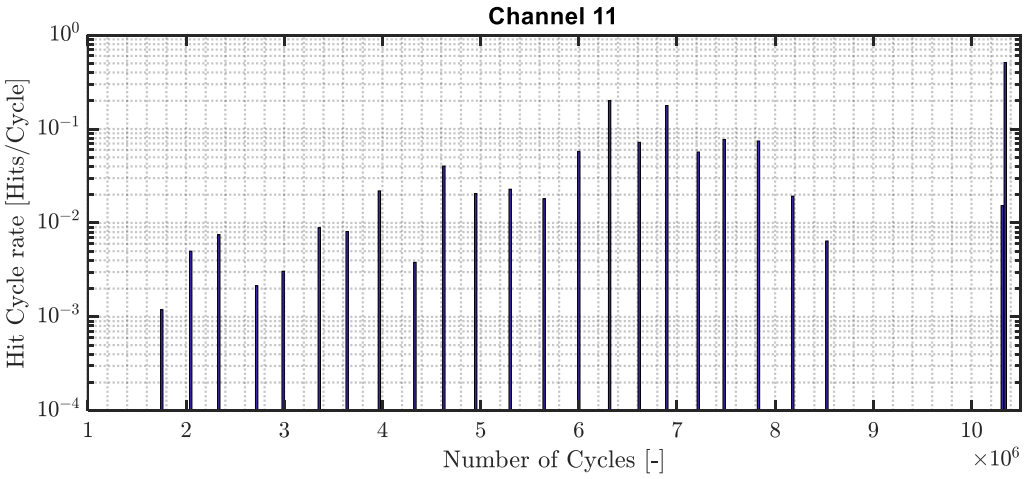
Channel 11
Hit Cycle rate [Hits/Cycle]
Number of Cycles [-]
×10^6

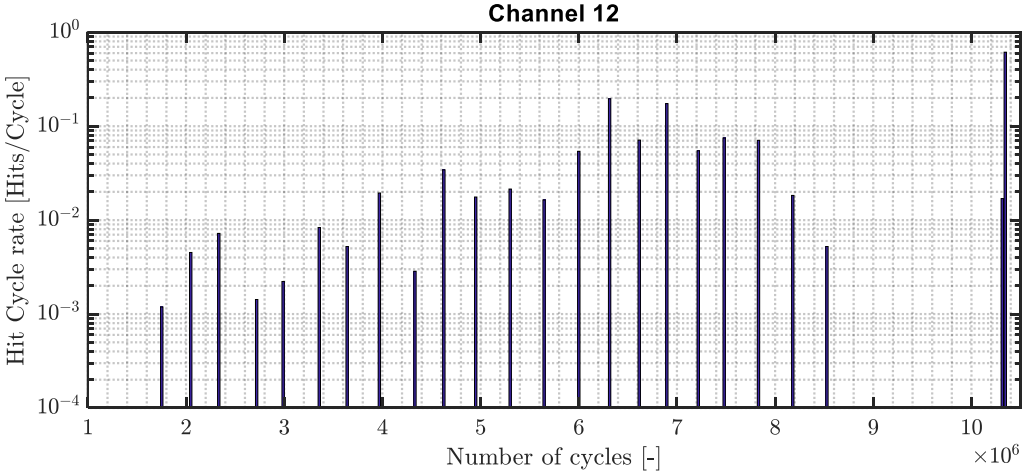
Channel 12
Hit Cycle rate [Hits/Cycle]
Number of cycles [-]
×10^6

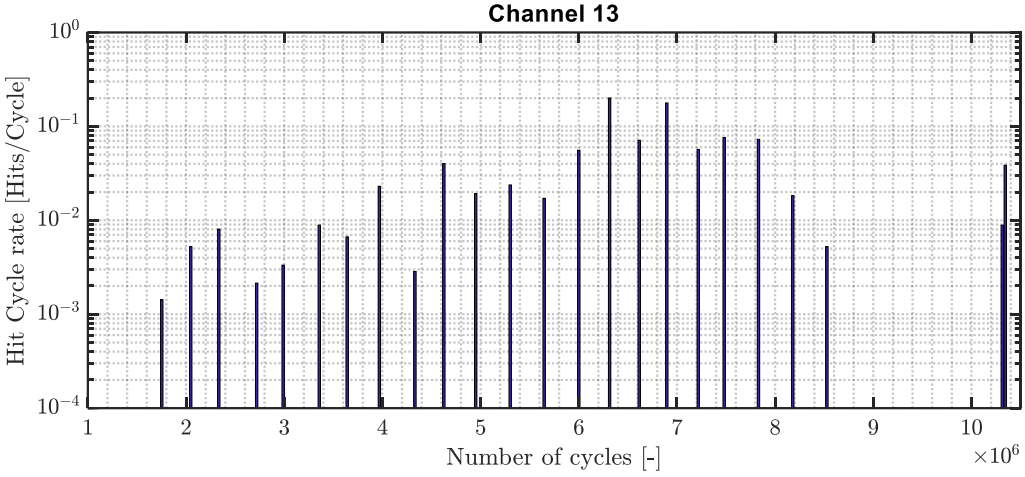
Channel 13
Hit Cycle rate [Hits/Cycle]
Number of cycles [-]
×10^6

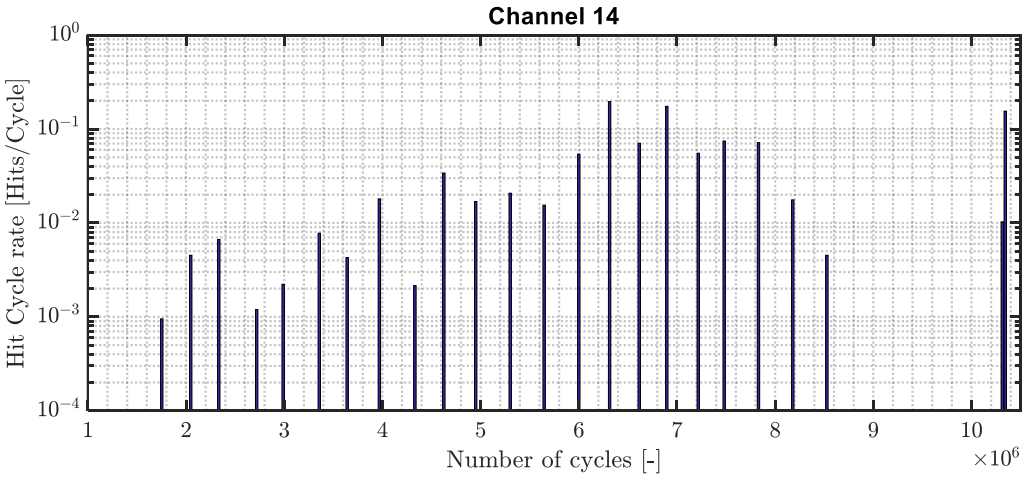
Channel 14
Hit Cycle rate [Hits/Cycle]
10^{0}
10^{-1}
10^{-2}
10^{-3}
10^{-4}
1 2 3 4 5 6 7 8 9 10
Number of cycles [-]
$\times 10^{6}$

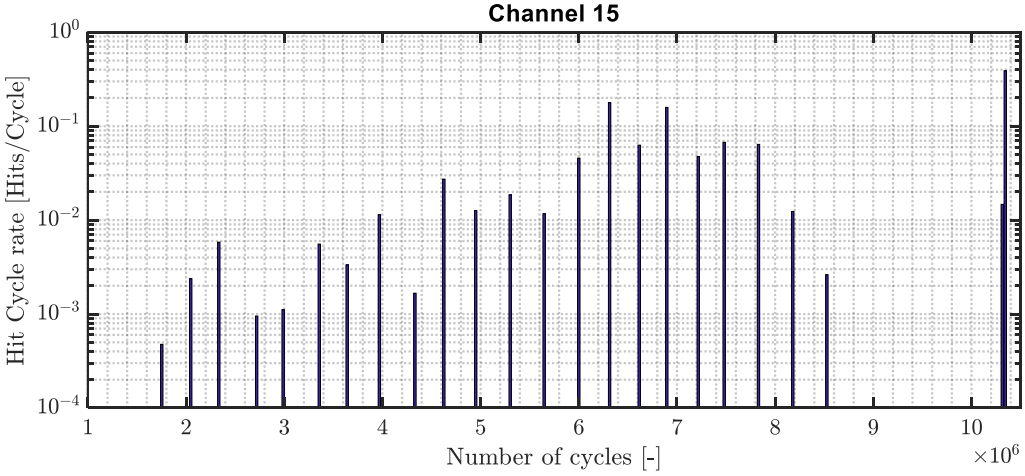
Channel 15
Hit Cycle rate [Hits/Cycle]
10^{0}
10^{-1}
10^{-2}
10^{-3}
10^{-4}
1 2 3 4 5 6 7 8 9 10
Number of cycles [-]
$\times 10^{6}$

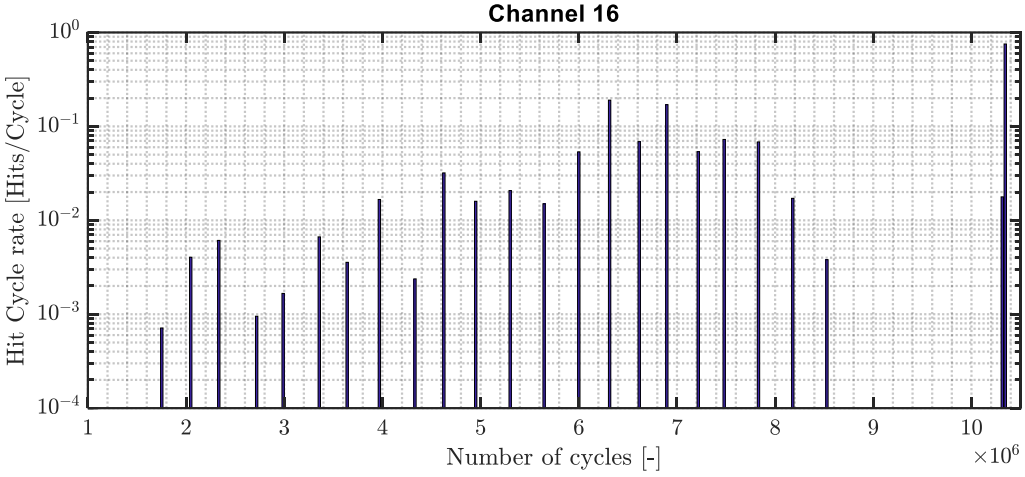
Channel 16
Hit Cycle rate [Hits/Cycle]
10^{0}
10^{-1}
10^{-2}
10^{-3}
10^{-4}
1 2 3 4 5 6 7 8 9 10
Number of cycles [-]
$\times 10^{6}$

Appendix E

Specifics of the VS600-Z2 sensor and the Pre-amplifier AEP5H that is used in the experiments.

5.1.21 VS600-Z2

VS600-Z2

The VS600-Z2 is a passive piezoelectric AE-sensor with integrated cable and full metal housing. Its frequency response is characterized by a peak at 600 kHz where it exhibits a resonance. Its small size makes it especially suited for being mounted on small samples where mounting space is restricted. Additionally it is ideally suited for gluing to the sample because of the full metal housing.

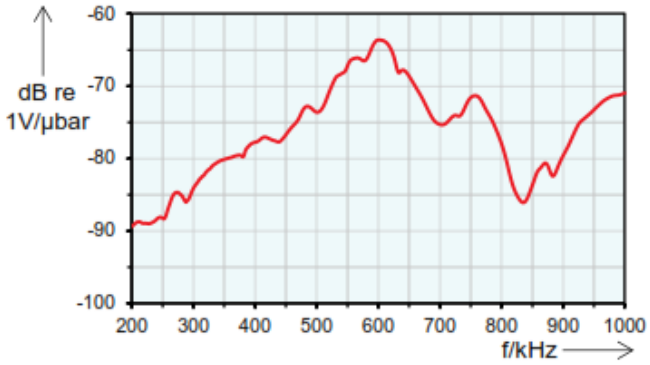

Technical Specification			
Frequency Range (f_{Peak}) [kHz]	400 to 800 (600)	**Size (D x H) [mm]**	4.75 x 5.3
Capacity [pF]	200 (incl. Cable)	**Weight [g]**	20
Integrated Preamplifier	No	**Case Material**	Stainless Steel (1.4571/ 1.4404)
Operating Temperature [°C]	-40 to +110	**Wear Plate**	Stainless Steel (1.4571/ 1.4404)
Vibration – Sinus Sweep	2 Oct/Min, 5 to 180 Hz, 40 g	**Connector**	SMA/BNC
Ingress Protection Rating	IP40	**Shield Cross-Talk [dB]**	< -80

Accessories			
Preamplifier	AEP5, AEP3N	**Sensor Cable**	(integral)
Mounting Holder			

4 AEP5 / AEP5H

The AEP5(H) is a general purpose preamplifier supporting single ended sensors. This preamplifier is a wide-band preamplifier available in two different bandwidth settings (AEP5 and AEP5H). Gain can be set to 34dB or 40dB. The gain selection switch is located inside the preamplifier to prevent any accidental changes of gain settings. As every preamplifier of Vallen Systeme GmbH the AEP5(H) can put a voltage pulse (up to 450 V_{pp}) through to the AE-sensor (sensor coupling test).

Figure 4: AEP5 preamplifier

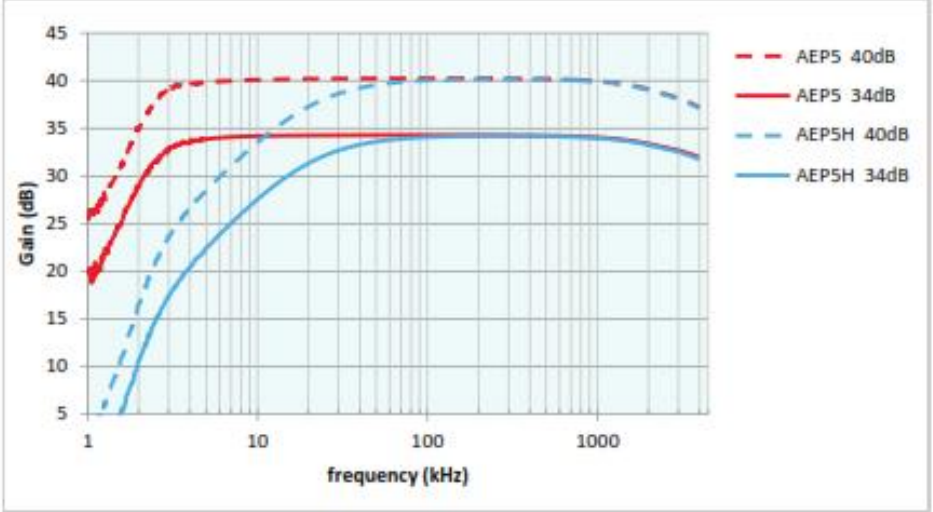

Figure 5: Frequency response of AEP5 and AEP5H preamplifier